

Level set methods for higher order evolution laws

D I S S E R T A T I O N

zur Erlangung des akademischen Grades

Doctor rerum naturalium
(Dr. rer. nat.)

vorgelegt

der Fakultät Mathematik und Naturwissenschaften
der Technischen Universität Dresden

von

Dipl.-Math. Christina Stöcker
geboren am 20.05.1975 in Münster

Gutachter: Prof. Dr. Axel Voigt (Betreuer)
Prof. Dr. Martin Burger
Prof. Dr. Peter Smereka

Eingereicht am: 27.11.2007

Tag der Disputation: 20.2.2008

Contents

1	Introduction	1
1.1	Level set methods	3
1.2	Applications in thin film epitaxy	4
2	Mathematical preliminaries	9
2.1	Analysis on surfaces	9
2.2	Level set methods	11
2.3	Finite element solutions	11
2.3.1	Boundary conditions	12
2.3.2	Adaptivity	13
2.3.3	Norm regularization	13
2.3.4	Energy dissipation and volume conservation	14
2.4	Redistancing	14
3	Isotropic evolution laws	19
3.1	Isotropic mean curvature flow	19
3.2	Isotropic surface diffusion	21
3.3	Isotropic kinetic model	24
3.4	Numerical results	26
3.4.1	Mean curvature flow	26
3.4.2	Surface diffusion	31
3.4.3	Kinetic model	33
4	Anisotropic evolution laws	43
4.1	Anisotropy	43
4.2	Anisotropic mean curvature flow	45
4.3	Anisotropic surface diffusion	46
4.4	Anisotropic kinetic model	47
4.5	Energy dissipation and volume conservation	49
4.6	Numerical results	49
4.6.1	Mean curvature flow	49
4.6.2	Surface diffusion	51
4.6.3	Kinetic model	54
5	Evolution laws with strong anisotropies	59
5.1	Non-convex anisotropies	60
5.2	Curvature regularized mean curvature flow	62
5.3	Curvature regularized surface diffusion	64
5.4	Kinetic model with curvature regularized anisotropy	66
5.5	Energy dissipation and volume conservation	68

5.6	Numerical results	68
5.6.1	Mean curvature flow	69
5.6.2	Surface diffusion	70
5.6.3	Kinetic model	73
6	Adatom model	79
6.1	Level set formulation	81
6.2	Weak formulation and discretization	82
6.3	Extension of adatom density	85
6.4	Energy dissipation and volume conservation	86
6.5	Numerical results	87
6.5.1	Isotropic situation	87
6.5.2	Strong anisotropic situation	90
7	Geodesic evolution laws	97
7.1	Level set method for geodesic evolution laws	98
7.1.1	Level set method for geodesic evolution laws on implicit surfaces	99
7.2	Discretization	99
7.2.1	Discretization for the surface mesh approach	99
7.2.2	Discretization for the implicit surface approach	100
7.3	Numerical results	101
7.3.1	Geodesic mean curvature flow	101
7.3.2	Geodesic surface diffusion	102
7.4	Geodesic mean curvature flow in image denoising	102
8	Conclusion	113
	Acknowledgment	115
	Bibliography	117

Chapter 1

Introduction

Geometric evolution equations arise in various different applications as image processing (image denoising, image restoration and image segmentation), bio-physics (biological membranes) and materials science (thin film growth, solidification processes, dendrite growth). Geometric evolution equations are in general highly non-linear partial differential equations which describe the evolution of surfaces in time. The evolution velocity and direction can be given in many different ways. It may for example be given as a prescribed velocity field independent from the surface, it may arise as a solution of another equation, or it may depend on the geometry of the surface itself. In difference to classical partial differential equations, geometric evolution laws are first of all not defined on a fixed computational domain, since the computational domain itself (the evolving surface) is part of the solution. Because of this property, the evolving surface is also called free boundary.

In order to solve the evolution equations, a mathematical description of the moving surface is needed. In numerical solution methods, there exist several representation approaches. One possibility is to describe the surface as the graph of a function. Another consists in using a parameterization of the surface. The surface can also be represented implicitly as a specific level line of a function, which is done in phase field and level set methods. The phase field approach goes back to the description of phase transition processes, where each phase is assigned to a constant value of the phase field function, typically one and zero, and where the phase field function provides a smooth connection between the constant values. The transition between one and zero occurs on a small transition area. In this approach the moving surface is represented as the level line one half of the phase field function. In difference to phase field functions, which reveal steep gradients in the transition area and constant values in the two phases, level set methods use functions with a norm of the gradient near one. The moving surface is typically the zero level set of the so called level set function. The graph formulation and the parametric approach are called direct methods, whereas the phase field and level set approaches are entitled as implicit methods. In each of the described methods, the representation function is defined on a reference domain which is fix. Thus, the surface representation method delivers a partial differential equation defined on a fixed computational domain.

In this work, the numerical solution of non-linear higher-order geometric evolution equations with level set methods is presented. We consider evolution laws, which describe evolution in normal direction, and where the normal velocity depends on the geometry of the surface. In case the normal velocity depends on the direction of the evolution, i.e. the surface normal, the evolution is called anisotropic. If the motion is independent from the surface normal, the evolution is called isotropic.

Most of the evolution equations we consider in this work model processes in thin film growth. As an introduction to the topic and a preparation for the more complex models, we start with the evolution equations of mean curvature flow (2nd-order equation) and surface diffusion

(4th-order equation), which describe singular phenomena therein. In thin film growth, mean curvature flow models the effect of attachment-detachment, and we therefore also speak of the evolution equations of attachment-detachment in this context. We then present a more complex model which combines the effects of attachment-detachment and surface diffusion, the kinetic model (4th-order equation). In computational results we compare the kinetic model to the models of attachment-detachment and surface diffusion and present results for different choices of parameters.

In all models mentioned so far, the evolution only depends on the geometry of the surface, and the surface itself is the only unknown in the resulting partial differential equations. In the physical process of thin film growth free adatoms, which are somehow mobile atoms on the film surface, are involved. Whether the occurrence of the free adatoms plays an important role for the evolution of the film surface or not is rather unclear. To better understand the influence of the free adatoms, we consider a generalization of the kinetic model, the so called adatom model, which incorporates free adatoms on the film surface. In addition to the surface geometry, the evolution here also depends on the free adatoms, and on the other hand, the change in the adatom density depends on the evolution, that means here we have two unknowns, the surface and the adatom density. Mathematically, the adatom model is a diffusion equation (diffusion of the adatoms) on an evolving surface, and is again a 4th-order equation.

The numerical solution of mean curvature flow and surface diffusion has already been broadly discussed in the literature, and the evolution behavior of these equations is well known. For the kinetic and the adatom model so far numerical simulations are rather rare.

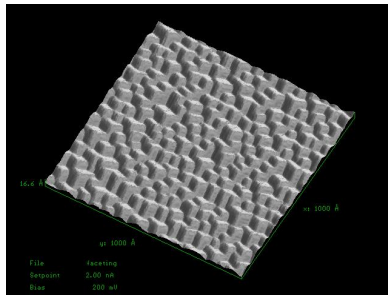


Figure 1.1: Faceted structure of a tungsten film surface¹.

For certain materials, e.g. tungsten, the growing film surface reveals a faceted structure, see figure 1.1. The surface consists of flat areas separated by corners and edges. In physical analysis it has recently been discovered that the corners and edges are not sharp for most temperature ranges but are rounded on a small length scale. The numerical simulation of faceting processes and the subsequent coarsening, where small facets merge to larger ones, is a topic of current research. In order to simulate the effect of faceting, non-convex anisotropies, also called strong anisotropies, are used. Because of the non-convexity the underlying equations are unstable for certain orientations, which provides the formation of facets. Rounded corners and edges as well as a stabilization of the equations are reached by the application of a regularization through higher order curvature terms. For all our models in thin film growth, besides the isotropic and (weak) anisotropic situation, we also present a level set solution for the faceting dynamics (strong anisotropic situation). The curvature regularization leads to an increase in the order of the equations by two, which results in a 4th order equation for attachment-detachment and 6th order equations for surface diffusion, the kinetic and the adatom model.

In the last chapter of this work we leave the physical application of thin film growth and turn to geodesic evolution equations, which are geometric evolution equations for curves on curved

¹Figures produced with Scanning Tunneling Microscope by C.-H. Nien and T. E. Madey, see [43] and [48].

surfaces. In the numerical solution of the geometric evolution of curves, the computational domain in most cases is considered to be planar. But any evolution in planar space could also take place on curved surfaces. The evolution of curves under mean curvature flow on curved surfaces has already been presented in the literature. Here, we also present the evolution under surface diffusion. The evolving curve and the fix surface both are represented by level set functions. We provide a comparison of numerical results with results, where the surface is given parametrically. As an application of geodesic mean curvature flow, we provide examples for image denoising on curved surfaces.

The partial differential equations are numerically solved by standard linear finite elements on unstructured triangular finite element grids. A semi-implicit time discretization scheme is employed. We use adaptively refined grids. The refinement is done via bisectioning, which maintains the regular structure of the initial grid. The discretization leads to systems of 2nd-order equations, which we solve with a Schur complement approach for the equations of mean curvature flow, surface diffusion and the kinetic model, and by an operator splitting approach in the adatom model.

1.1 Level set methods

In level set methods the evolving d -dimensional free boundary or surface is embedded into a larger domain $\Omega \subseteq \mathbb{R}^{d+1}$, which is fix during the whole evolution. The surface at time t is described implicitly as the zero level set of a function $\phi : \Omega \times \mathbb{R}^{\geq 0} \rightarrow \mathbb{R}$ through

$$\Gamma(t) = \{x \in \mathbb{R}^{d+1} \mid \phi(x, t) = 0\}.$$

The evolution of the surface is represented by the evolution of $\phi(., t)$ in time, which provides a family of surfaces $(\Gamma(t))_{t \geq 0}$. The domain Ω is chosen in such a way that it contains all surfaces $\Gamma(t)$ and that it can easily be resolved by the finite element grid used in the numerical solution of the evolution problem. The level set method has been introduced by Osher and Sethian in [50] and is nowadays applied to a broad range of applications as fluid dynamics, materials science and image processing only to mention a few. More information on level set methods and their applications can be found in [49] and [57].

In comparison to direct methods as the graph or parametric representation, the level set method involves an increase in dimension. Tracking a d -dimensional surface requires a function defined on a $d+1$ -dimensional domain. To keep computational costs low, some sort of adaptivity has to be used. We use an heuristic approach which guarantees a fine resolution near the evolving surface and provides a coarse grid away from the surface. More details on the adaptivity approach will be given in the next chapter. The higher computational costs are somehow compensated by other factors as the flexibility in choosing evolving surfaces (any surface which can be represented implicitly by a level set function is allowed) and the ease in handling the computational grid (the surface does not have to be resolved by the grid which would demand sophisticated algorithms to maintain the grid regular during complex evolutions).

For numerical reasons, the level set function should be kept near signed distance. $\phi(., t)$ is a signed distance function on the domain Ω if for any point $x \in \Omega$ the absolute value of $\phi(x, t)$ is the distance of x to the surface $\Gamma(t)$. The sign of the signed distance function indicates on which side of the surface the point x is situated. There are many different approaches how to maintain the signed distance property during evolution. We use the direct approach introduced in [8], which calculates the signed distance function iteratively for a given level set function. A detailed description of the algorithm will be given in the next chapter.

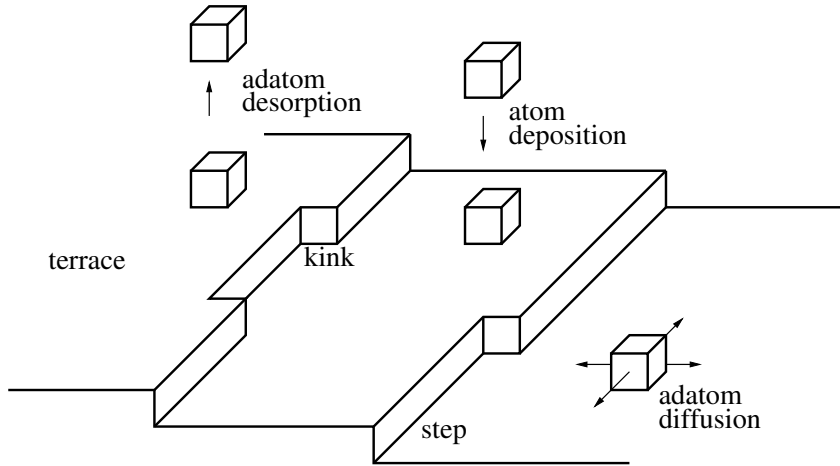


Figure 1.2: Thin film epitaxy.

1.2 Applications in thin film epitaxy

Film growth is a growth process which takes place in small ranges and is applied e.g. in semiconductor industry. Controlling the growth process is a difficult task and physical experiments are expensive. The aim in simulating thin film epitaxy is to gain deeper insight in the growth process without physical experiments.

Many different physical effects have an impact on the thin film morphology. In this section, we first present an outline of thin film epitaxy and explain our modelling assumptions. Afterwards, we concentrate on two basic transport mechanisms, which determine the evolution of the film surface. The singular phenomena of condensation-evaporation (attachment-detachment in solid-vapour phase transitions) and surface diffusion are discussed in more detail, which lead to the geometric evolution equations of mean curvature flow and surface diffusion respectively. We will only describe the simplest case, the isotropic situation, where the motion velocity does not depend on the motion direction. The kinetic model, the adatom model and the anisotropic situation will be discussed later in this work. Details on thin film and crystal growth can be found in [32] and [52].

In the process of thin film epitaxy material is grown on a substrate of not necessary the same material in atomistic layers. Most commonly condensation is used to deposit the material on the substrate, and different temperatures in the substrate and the vapour play an important role. One possible technique to produce thin films is molecular beam epitaxy (MBE). We can imagine the material to arrive atom by atom on the substrate. The atoms build chemical bonds

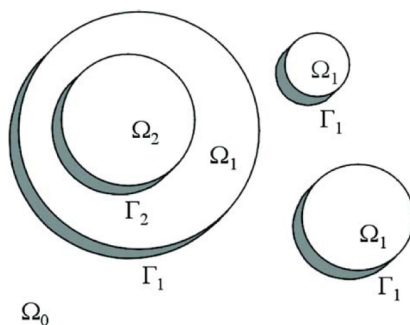


Figure 1.3: Island growth.

with the substrate and attach to its surface, see figure 1.2. By this, they form a thin film on the substrate. To differentiate, atoms which are attached to the substrate or film surface are called adatoms or free adatoms as long as the chemical bonds are not strong enough to incorporate them at a fixed place. Adatoms are somehow mobile on the film surface. They can move around (diffuse), nucleate with other adatoms, and by this form terraces and islands of atomic height. See figure 1.3 for the formation of different islands and islands that grow on top of others. The adatom model in chapter 6 accounts for the portion of free adatoms on the film surface.

The driving force behind the adatom motion is the reduction of the energy of the thin film. If it is energetically more favorable, adatoms also detach from the surface and return into the vapour. We only consider models where the energy in the thin film surface is the dominant energy part, that means a decrease in the surface energy is the driving force in our dynamics. Our aim is to track the evolution of the thin film surface. Furthermore, we concentrate on models where changes in the surface structure are only due to rearrangements of adatoms on the surface. The kinetic model will also include contributions from the bulk, but we will neglect these contributions in the numerical treatment of the model. We will not consider deposition fluxes. Atoms may change from the solid to the vapour and vice versa, but no new atoms are entered in this closed solid-vapour system.

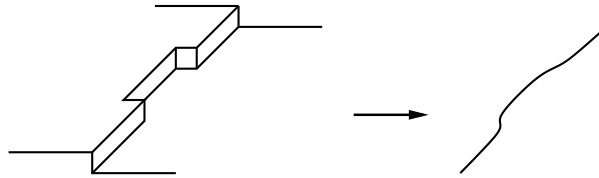


Figure 1.4: Modelling of terrace boundary.

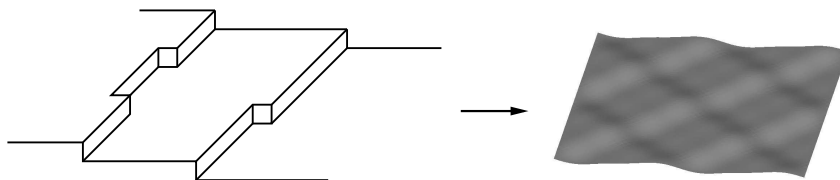


Figure 1.5: Modelling of film surface.

Various models describing the thin film process can be found in the literature. There are models which take account for single adatoms and the atomistic height of terraces and islands. Others, macroscopic models, neglect the discrete structure of the thin film and consider its surface to be smooth. The BCF-model ([14]) is somehow in between: it is discrete with respect to the height of the atomic layers but continuous with respect to the shape of island and terrace boundaries. In this work, we are interested in two different parts of the growth process which belong to different dimensions. The evolution of curves in two-dimensional space models the evolution of island (closed curves) or terrace boundaries (non-closed curves). The figures showing our numerical results later in this work can be understood as a top view on the evolving islands or terraces. See figure 1.4 for the modelling assumptions in 2D. The evolution of surfaces in three-dimensional space models the evolution of film surfaces (non-closed surfaces) or crystals (closed surfaces). Furthermore, the atomic structure is neglected and we assume the curves and surfaces to be smooth. See figure 1.5 for the modelling assumptions in 3D.

The physical term which describes the potential of a system to reduce energy is the chemical potential. It can be divided into the chemical potential in the solid phase, the chemical potential in the vapour phase and the chemical potential on the film surface or solid-vapour interface. In

general, the chemical potential characterizes the property of a material for chemical reactions, phase transitions and diffusion. Since we neglect contributions from the solid and the vapour phase in our computations, the numerical models will only depend on the surface chemical potential μ . The surface chemical potential is related to the surface free energy. In the case of mean curvature flow and surface diffusion, the surface chemical potential is the variational derivative of the surface energy functional. It depends on the geometry of the film surface, especially its mean curvature and orientation (surface normal). In the kinetic model, it is in addition influenced by the motion velocity of the surface (kinetics). And in the adatom model the chemical potential depends on the adatom density of the surface, which on the other hand relies on the geometry of the surface and its changes. We will now present two prominent examples for geometric evolution equations in thin film epitaxy: mean curvature flow, modelling the effect of attachment-detachment, and surface diffusion.

Mean curvature flow in thin film epitaxy

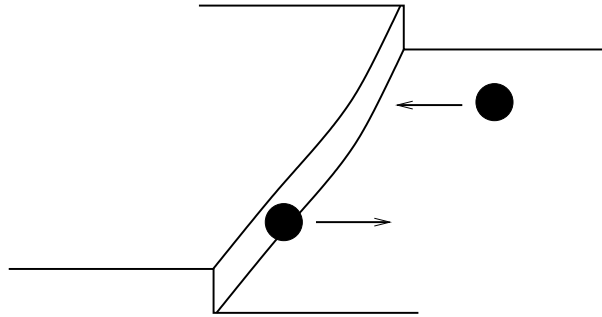


Figure 1.6: Attachment and detachment at a terrace boundary.

As its name implies, attachment describes the effect when atoms from the vapour phase attach to the surface or adatoms attach to a terrace or island boundary. Detachment is the contrary effect when adatoms release their bonds to the surface or boundary. Since the attachment-detachment to/from the film surface is a solid-vapour phase transition, it is also called condensation-evaporation. It can be modelled by mean curvature flow. This model was first introduced by Mullins [45]. With μ_v the chemical potential in the vapour, a material constant c and a surface normal which points into the vapour phase, the normal velocity V of the surface in an attachment-detachment process is given through

$$V = -c(\mu - \mu_v).$$

We neglect the chemical potential in the vapour ($\mu_v = 0$). The chemical potential μ is related to the surface free energy $E[\Gamma]$ through

$$\mu = \frac{\delta E}{\delta \Gamma}.$$

Thus attachment-detachment gives the motion of the film surface in the direction of steepest energy descent. In the case of isotropic evolution, i.e. evolution that does not depend on the orientation of the surface, and where the surface free energy is given through

$$E[\Gamma] = \int_{\Gamma} 1 \, dA,$$

the variational derivative with respect to variations in normal direction is

$$\frac{\delta E}{\delta \Gamma} = H,$$

where H is the mean curvature of the surface. Thus we obtain the mean curvature equation

$$V = -cH.$$

That means in regions where the mean curvature of the surface is positive, adatoms detach or evaporate, and in regions with negative mean curvature material is incorporated in the solid. See figure 1.6 for the attachment and detachment at a terrace boundary.

Surface diffusion in thin film epitaxy

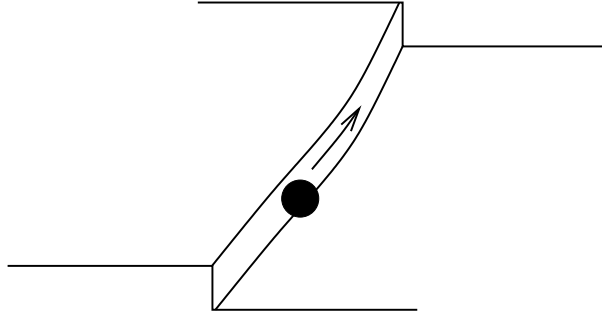


Figure 1.7: Edge diffusion.

Surface diffusion is the phenomenon where adatoms diffuse on the film surface or along a terrace or island edge (edge diffusion). The diffusion is described through a vector field j which is tangent to the surface and given by the surface gradient of the chemical potential

$$j = -m\nabla_{\Gamma}\mu$$

with the positive mobility coefficient m . Since adatoms only change their place on the film surface the mass of the thin film remains unchanged. Considering surface motion which obeys $V = -\nabla_{\Gamma} \cdot j$ for a given material flux j ensures mass conservation, see [15]. With the above choice of the material flux, this provides the equation of surface diffusion

$$V = \nabla_{\Gamma} \cdot (m\nabla_{\Gamma}\mu).$$

The model was also first introduced by Mullins in [46]. See figure 1.7 for an illustration of edge diffusion.

We have only presented the simplest situation and models. In anisotropic situation, the energy functional includes the anisotropy function, which accounts for a different weight for different normal directions. And in the application of curvature regularization as well as for the adatom model, the energy functional is even more complicated. Curvature regularization will lead to non-linear equations of up to 6th order. Parts of this work have already been published in [63], [12], [64], [65], [13] and [66].

Chapter 2

Mathematical preliminaries

Our aim is to track the evolution of surfaces. In this chapter we summarize some geometric analysis required for the mathematical description of the evolution. The level set representation of some basic notions as the mean curvature of a surface and surface gradients will be given. Furthermore, we discuss some general aspects as norm regularization, grid adaptivity and redistancing of level set functions.

2.1 Analysis on surfaces

Let Γ denote the evolving surface, which we model mathematically as a smooth oriented hypersurface in \mathbb{R}^{d+1} . We further assume that Γ is embedded in a domain $\Omega \subseteq \mathbb{R}^{d+1}$. The set Ω will be the domain on which we define our equations.

The surface normal $\nu(x)$ to Γ in $x \in \Gamma$ is given through a differentiable function ν defined in a neighborhood of Γ . In particular the vector $\nu(x)$ is perpendicular to the tangential space $T_x\Gamma$ for each $x \in \Gamma$. The mean curvature function H is defined through

$$H = \nabla \cdot \nu. \quad (2.1)$$

For each $x \in \Gamma$, this definition corresponds to the more common one

$$H(x) = \sum_{i=1}^d \kappa_i(x),$$

where $\kappa_i(x)$ is the i -th principle curvature of Γ in x . See e.g. [23] for the relation between the two definitions of $H(x)$.

For a differentiable function f and a differentiable flow field F defined in a neighborhood of Γ , the surface gradient of f is given through

$$\nabla_\Gamma f = P_\Gamma \nabla f = (I - \nu \otimes \nu) \nabla f, \quad (2.2)$$

where P_Γ denotes the orthogonal projection of a vector in \mathbb{R}^{d+1} on the tangential space of Γ , and

$$\nabla_\Gamma \cdot F$$

denotes the surface divergence. The surface laplacian is then defined through

$$\Delta_\Gamma f = \nabla_\Gamma \cdot \nabla_\Gamma f. \quad (2.3)$$

We describe the motion of a surface through a family of hypersurfaces $(\Gamma(t))_{t \geq 0}$, where $\Gamma(t)$ is the hypersurface at time instance t . We restrict to evolution where each point of the surface

moves in direction normal to the surface, and V denotes the normal velocity. We use the formula for integration by parts on surfaces

$$\int_{\Gamma} \nabla_{\Gamma} \cdot F \eta \, dA = \int_{\partial\Gamma} F \cdot m_{\Gamma} \eta \, ds - \int_{\Gamma} F \cdot \nabla_{\Gamma} \eta \, dA,$$

where m_{Γ} is the normal to $\partial\Gamma$. If Γ is a surface without boundary, $\partial\Gamma = \emptyset$, or $\eta|_{\partial\Gamma} \equiv 0$ this simplifies to

$$\int_{\Gamma} \nabla_{\Gamma} \cdot F \eta \, dA = - \int_{\Gamma} F \cdot \nabla_{\Gamma} \eta \, dA. \quad (2.4)$$

For a differentiable flow field X on Ω , the formula for integration by parts in space reads

$$\int_{\Omega} \nabla \cdot X \eta \, dx = \int_{\partial\Omega} X \cdot m_{\Omega} \eta \, dA - \int_{\Omega} X \cdot \nabla \eta \, dx,$$

with m_{Ω} the normal to $\partial\Omega$. If $\eta \in C_0^{\infty}(\Omega)$ or $X \cdot m_{\Omega} = 0$ this simplifies to

$$\int_{\Omega} \nabla \cdot X \eta \, dx = - \int_{\Omega} X \cdot \nabla \eta \, dx. \quad (2.5)$$

Let $(G(t))_{t \geq 0}$ be bounded subsets of Ω with $\partial G(t) = \Gamma(t)$ evolving in normal direction in time, and Q an open subset of $\Omega \times \mathbb{R}$ containing $(G(t) \cup \partial G(t)) \times \{t\}$ for $t \geq 0$. For a differentiable function f defined on Q , transport theorems (see [23]) read

$$\frac{d}{dt} \int_{G(t)} f \, dx = \int_{G(t)} \frac{\partial f}{\partial t} \, dx + \int_{\Gamma(t)} f V \, dA \quad (2.6)$$

and

$$\frac{d}{dt} \int_{\Gamma(t)} f \, dA = \int_{\Gamma(t)} \frac{\partial f}{\partial t} \, dA + \int_{\Gamma(t)} f V H \, dA + \int_{\Gamma(t)} \frac{\partial f}{\partial \nu} V \, dA. \quad (2.7)$$

For the special case $f \equiv 1$, equation (2.6) gives a formula for the change of volume of $G(t)$

$$\frac{d}{dt} \text{volume}(t) = \frac{d}{dt} \int_{G(t)} 1 \, dx = \int_{\Gamma(t)} V \, dA. \quad (2.8)$$

For a function $g : S^d \rightarrow \mathbb{R}$ and a functional

$$E[\Gamma] = \int_{\Gamma} g(\nu) \, dA$$

we have the time derivative

$$\frac{d}{dt} E[\Gamma(t)] = \int_{\Gamma(t)} V \frac{\delta E}{\delta \Gamma} \, dA, \quad (2.9)$$

where $\frac{\delta E}{\delta \Gamma}$ is the variational derivative of E with respect to variations in normal direction. And for functions $g : S^d \times \mathbb{R}$, $(u(\cdot, t))_{t \geq 0}$ with $u(\cdot, t)$ defined in a neighborhood of $\Gamma(t)$ and a functional

$$E[\Gamma(t), u(\cdot, t)] = \int_{\Gamma(t)} g(\nu, u(\cdot, t)) \, dA$$

in more general situation, we have the time derivative

$$\frac{d}{dt} E[\Gamma(t), u(\cdot, t)] = \int_{\Gamma(t)} u_t \frac{\delta E}{\delta u} \, dA + \int_{\Gamma(t)} V \frac{\delta E}{\delta \Gamma} \, dA \quad (2.10)$$

with $\frac{\delta E}{\delta u}$ the variational derivative of E with respect to variations in u .

2.2 Level set methods

In level set methods, evolution in normal direction with normal velocity V is described through the level set equation

$$\phi_t + V|\nabla\phi| = 0, \quad (2.11)$$

where the level set function ϕ provides implicitly the evolving surface ($\Gamma(t) = \{\phi(\cdot, t) = 0\}$). A transformation of the level set equation gives an expression for the normal velocity in terms of the level set function

$$V = -\frac{\phi_t}{|\nabla\phi|}. \quad (2.12)$$

The outer surface normal is given through

$$\nu = \frac{\nabla\phi}{|\nabla\phi|}, \quad (2.13)$$

and applied to the definition of the mean curvature (2.1), we obtain the level set formulation for the mean curvature

$$H = \nabla \cdot \frac{\nabla\phi}{|\nabla\phi|}. \quad (2.14)$$

Thus, the surface normal points in the direction of increasing level set function values. In our convention, a sphere with outer surface normal has positive mean curvature. Using the level set description of the surface normal (2.13) in the definition of the surface gradient (2.2) results in

$$\nabla_\Gamma f = P_\Gamma \nabla f = \left(I - \frac{\nabla\phi}{|\nabla\phi|} \otimes \frac{\nabla\phi}{|\nabla\phi|} \right) \nabla f$$

for a differentiable function f defined in a neighborhood of the surface Γ , and we obtain the surface divergence of a differentiable flow field F defined in a neighborhood of Γ through

$$\nabla_\Gamma = \frac{1}{|\nabla\phi|} \nabla \cdot \left(|\nabla\phi| F \right). \quad (2.15)$$

The surface Laplacian in level set formulation reads

$$\Delta f = \nabla_\Gamma \cdot \nabla_\Gamma f = \frac{1}{|\nabla\phi|} \nabla \cdot \left(|\nabla\phi| P_\Gamma \nabla f \right). \quad (2.16)$$

Let us finally introduce some notations for distinct subsets of Ω . We denote $B(t)$ the subset with negative or zero level set function values of ϕ ,

$$B(t) = \{x \in \Omega \mid \phi(x, t) \leq 0\}.$$

In the examples of thin film epitaxy, $B(t)$ represents the solid phase. Furthermore, $|B(t)|$ denotes the volume of the subset $B(t)$ and $|\Gamma(t)|$ the area of the surface $\Gamma(t)$. In our numerical examples for closed curves and surfaces, the initial level set function will always be defined in such a way that the domain enclosed by the curves or surfaces is the domain with negative level set function values.

2.3 Finite element solutions

The parabolic partial differential equations, which arise in our evolution problems, are numerically solved with the finite element method. We use standard linear finite elements on simplicial grids. For simplicity in the notations, we assume that the domain of interest Ω has a boundary

of polygonal shape which is resolved by the finite element grid. By this, we do not distinguish between the domain of interest in the partial differential equation and its approximation, the computational domain, in the finite element discretization. If \mathcal{T}_h denotes the partition of Ω into finite elements, the finite element space \mathcal{V}^h is the space of piecewise linear functions

$$\mathcal{V}^h = \{\varphi \in C^0(\bar{\Omega}) \mid \varphi|_{\sigma} \text{ is linear for all elements } \sigma \in \mathcal{T}_h\}.$$

We use shape regular finite element grids. Regularity in the grid is reached through a grid refinement and coarsening method which is based on bisectioning and preserves the shape of the initial grid elements. To illustrate this method, we have a closer look at the refinement on two-dimensional grids. In all our numerical 2D examples, we start with an initial grid which looks like the grid in figure 2.1 on the left or consists of several components of this structure. Two refinement steps lead to a finer grid which contains four times the initial structure, see figure 2.1 on the right. In 3D grids a similar basic grid component is used. Here, three refinement steps are needed to regain the structure of the initial component in a finer grid. All numerical examples have been computed with the finite element toolbox AMDiS [2].

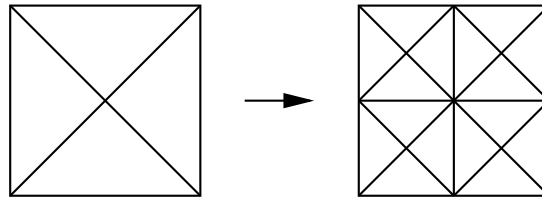


Figure 2.1: Refinement on two-dimensional grid. Basic grid component in 2D on the left, and grid after two refinement steps on the right.

We will now briefly comment on the boundary conditions we use in the finite element solutions, the applied grid adaptivity and a norm regularization which ensures stability for small gradients of the level set function.

2.3.1 Boundary conditions

We are only interested in the evolution of our curve or surface. The embedding of these moving interfaces into a higher-dimensional domain Ω in the level set method is, among other advantages, a device to gain partial differential equations on a fixed grid. But the solution of the equation at the boundary $\partial\Omega$ first of all has no influence on the motion of the interface. Our choice of boundary conditions is somehow arbitrary. For the evolution of closed curves and surfaces,

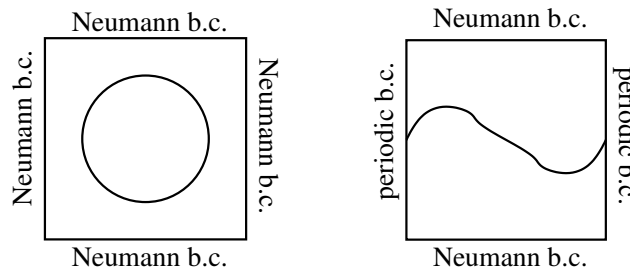


Figure 2.2: On the left: boundary conditions for evolution of closed curves. On the right: boundary conditions for evolution of non-closed curves.

we apply homogeneous Neumann boundary conditions on $\partial\Omega$, see figure 2.2 on the left for an illustration in 2D. And for the evolution of non-closed curves and surfaces, i.e. where the

interface cuts the boundary of the computational domain, we use periodic boundary conditions on the side walls of Ω and homogeneous Neumann boundary conditions on the top and bottom part of $\partial\Omega$, see figure 2.2 on the right for an illustration in 2D.

2.3.2 Adaptivity

We are interested in the evolution of the interface Γ in time. So the resolution of the finite element grid, which is a partition of the computational domain Ω , has to be fine at the interface to ensure an appropriate approximation of the evolution process. In comparison to front tracking methods, where the finite element grid is an approximation of the moving interface, a uniform grid refinement, which results in a small grid resolution on the complete computational domain, would lead to a high computational overhead. But exact information about the evolution of the level set function far away from the interface is not needed. So some sort of adaptivity should be used. One possibility is to use a narrow band approach which in each timestep solves the equations only on a small band around the moving interface. The grid resolution is small on this band and the band changes in each timestep. This approach is quite difficult to apply on unstructured grids.

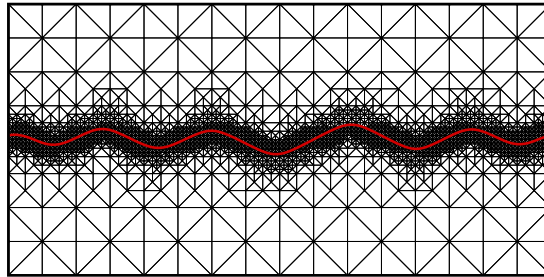


Figure 2.3: Computational grid adaptively refined at the evolving curve.

We therefore use another approach, which consists in an heuristic adaptive grid refinement. Elements near the interface are resolved with a fine resolution, and far away from the interface a coarse grid resolution is used. For an example of an adaptively refined grid in 2D see figure 2.3. To decide where to use fine and where to use coarse grid resolution, the distance property of the level set function is applied. With the redistancing method presented in the next section we can assume, that the level set function ϕ in each point $x \in \Omega$ gives an approximate value for the distance of x to the interface through $|\phi(x)|$.

In the numerical examples, h will denote the grid size at the interface. To avoid problems in the solver convergence of the linear system to be solved in each timestep, the element size far away from the interface is chosen to be at most ten times larger than at the interface.

2.3.3 Norm regularization

In our discretized equations, operator terms including the inverse of the norm of the level set function, $\frac{1}{|\nabla\phi|}$, occur. To avoid instabilities due to small gradients, it is common to use the norm regularization $|\cdot|_\delta$, which is defined through

$$|x|_\delta = \left(|x|^2 + \delta^2\right)^{1/2}$$

for $x \in \Omega$. $|\cdot|$ denotes the Euklidean norm. Choosing the regularization parameter δ in a size about the grid size h has turned out to be the best choice of parameter. In our adaptively refined grids, we choose $\delta \sim h$ with h the grid size at the interface.

2.3.4 Energy dissipation and volume conservation

For the models of mean curvature flow, surface diffusion, the kinetic model and the adatom model, the energy dissipating property of the evolution laws is depicted in chapters 3-6. Energy dissipation is controlled for each numerical example therein. Evolution under surface diffusion is volume conserving, as well as evolution in the kinetic model and the adatom model when neglecting the mean curvature flow part. Short justifications for this property will be given. In all numerical examples dealing with a volume conserving evolution in this work, the change in volume is controlled. The development of energy and volume in time will be illustrated in selected examples.

2.4 Redistancing

It is a common problem in level set methods, that the level set function which is the unknown of our geometric evolution equations, becomes somehow degenerate during evolution. Level lines move close to each other (steep gradients), increase their distance to each other in other areas (flat gradients) or may even intersect. A fast change from flat to steep gradients can also often be observed. Areas with high curvatures in the level lines are in particular sensitive to this behavior. In evolution equations with higher than second order, a reason for the degenerate evolution is certainly the missing of a comparison principle. Whereas in second order equations, the comparison principle guarantees that different level lines do not intersect or do not even decrease their distance to each other, this is not the case for higher order equations. For numerical reasons it is thus desirable to deal with level set functions which are signed distance functions ($|\nabla\phi| = 1$). In general, one is only interested in the evolution of the interface given by the zero level set. So reestablishing the signed distance property of the level set function while maintaining the zero level set ("redistancing") does not change the solution.

Since any redistancing slightly changes the interface, it should be employed with care. In our implementation we check the norm of the gradient of the level set function ϕ in a band around the zero level set which is about the grid size. If the norm differs too much from one, which in our implementation is the case if $|\nabla\phi| \leq 0.5$ or $|\nabla\phi| \geq 2.0$, redistancing is done.

Our redistancing algorithm is an approach for unstructured grids based on a local Hopf-Lax formula which was introduced in [8] and given in detail for two dimensions therein. In [63] it was extended to three dimensions. In the following we give a brief outline of the idea behind and describe the algorithm in detail.

Let ϕ be the level set function for which we want to calculate the signed distance function. ϕ defines implicitly the interface Γ through

$$\Gamma = \{x \in \Omega \mid \phi(x) = 0\}.$$

The redistancing problem now consists in finding a function $\tilde{\phi} : \Omega \rightarrow \mathbb{R}$ which satisfies

$$|\nabla\tilde{\phi}| = 1 \quad \text{on } \Omega \tag{2.17}$$

$$\tilde{\phi}|_{\Gamma} = 0. \tag{2.18}$$

This defines a distance function to Γ . Calculating a distance function, where our algorithm actually will restrict to, is sufficient. The correct sign can be added afterwards in a postprocessing step with the sign of the function ϕ through

$$\begin{aligned} \tilde{\phi}(x) &> 0 && \text{if and only if} && \phi(x) > 0 \\ \tilde{\phi}(x) &< 0 && \text{if and only if} && \phi(x) < 0. \end{aligned}$$

For closed interfaces the redistancing problem (2.17) and (2.18) restricted to the bounded domain B enclosed by the interface is the eikonal equation, which in a more general form is given through

$$\begin{aligned} |\nabla \tilde{\phi}| &= 1 & \text{on } B \\ \tilde{\phi}|_{\Gamma} &= g \end{aligned}$$

with an adequate function g . This is a Hamilton-Jacobi equation. In [41] it is shown that under certain conditions on g a solution of the eikonal equation is given through the Hopf-Lax formula

$$\tilde{\phi}(x) = \min_{y \in \partial B} (g(y) + |x - y|)$$

under the assumption that the segment line through x and y is contained in $\bar{\Omega}$. The principle idea of the redistancing algorithm is to apply the Hopf-Lax formula on a local discretized problem.

To emphasize that we are in the discrete situation, we denote Ω_h the polygonal approximation of Ω . The polygonal approximation Γ_h of the interface Γ is implicitly given through the finite element approximation $\phi_h \in \mathcal{V}^h$ of the level set function ϕ . We denote \mathcal{T}_h^I the set of elements $\sigma \in \mathcal{T}_h$ which are cut by the interface ("interface elements"), i.e.

$$\mathcal{T}_h^I = \{\sigma \in \mathcal{T}_h \mid \sigma \cap \Gamma_h \neq \emptyset\},$$

and define

$$\Omega_h^I = \bigcup_{\sigma \in \mathcal{T}_h^I} \sigma.$$

The redistancing algorithm mainly consists of two steps: first, the calculation of the distances of the vertices in interface elements to the interface, and second subsequent iterations over all non-interface elements, where local Hopf-Lax updates are processed on each element, until the correct distance information is spread to the complete grid. The distance on vertices of interface elements is calculated directly with geometric considerations on the element. We define a function g_h on Ω_h , which after this first redistancing step ("initialization") holds the correct distance information for the vertices $x_h \in \bar{\Omega}_h^I$.

We now come to the local Hopf-Lax update. For each vertex $x_h \notin \bar{\Omega}_h^I$, we define the local element patch $\omega_h(x_h)$ as the interior of the union of all elements $\sigma \in \mathcal{T}_h \setminus \mathcal{T}_h^I$ containing x_h . For a prescribed function g_h , a solution of the local discretized problem

$$\begin{aligned} |\nabla \phi_h^*| &= 1 & \text{on } \omega_h(x_h) \\ \phi_h^*|_{\partial\omega_h(x_h)} &= g_h \end{aligned}$$

is given by the local Hopf-Lax formula

$$\phi_h^*(x_h) = \min_{y \in \partial\omega_h(x_h)} (g_h(y) + |x_h - y|).$$

The second step in the redistancing algorithm consists now in an iterative application of the local Hopf-Lax formula for the grid vertices $x_h \notin \bar{\Omega}_h^I$. We define the local Hopf-Lax update through

$$(\Lambda_h \phi_h)(x_h) = \begin{cases} \min_{y \in \partial\omega_h(x_h)} (\phi_h(y) + |x_h - y|) & \text{for } x_h \notin \bar{\Omega}_h^I \\ \phi_h(x_h) & \text{for } x_h \in \bar{\Omega}_h^I. \end{cases}$$

A possible redistancing algorithm consists in traversing all vertices x_h until the Hopf-Lax updates do not give new values or to be more precise until for any small tolerance tol we have $|(\Lambda_h \phi_h)(x_h) - \phi_h(x_h)| \leq tol$ for all vertices x_h . Since our approach is a slight variation of this

idea, we give a short explanation for the convergence of the Hopf-Lax updates which is based on a monotonicity argument: The sequence $(\phi_h^n)_{n \geq 0}$ defined through

$$\phi_h^0(x_h) = \begin{cases} \infty & \text{for } x_h \notin \bar{\Omega}_h^I \\ g_h(x_h) & \text{for } x_h \in \bar{\Omega}_h^I \end{cases}$$

and

$$\phi_h^{n+1} = \Lambda_h \phi_h^n$$

is decreasing monotonously,

$$\phi_h^{n+1} \leq \phi_h^n \leq \dots \leq \phi_h^1 \leq \phi_h^0.$$

Since there is the lower bound

$$\phi_h^n(x_h) \geq \min_{y_h \in \bar{\Omega}_h^I} g_h(y_h) \quad \text{for all } n \geq 0,$$

for each vertex x_h , the sequence converges uniformly to a function $\tilde{\phi}_h$.

Our approach uses an element-based Hopf-Lax vertex update

$$(\Lambda_h \phi_h)(x_h, \sigma) = \begin{cases} \min_{y \in \partial\omega_h(x_h) \cap \bar{\sigma}} (\phi_h(y) + |x_h - y|) & \text{for } x_h \notin \bar{\Omega}_h^I \\ \phi_h(x_h) & \text{for } x_h \in \bar{\Omega}_h^I. \end{cases} \quad (2.19)$$

With these definitions, our redistancing algorithm can now be described:

1. For all vertices x_h in $\bar{\Omega}_h^I$:
Calculate the distance $g_h(x_h)$ to the discretized interface Γ_h .

2.

$$\tilde{\phi}_h(x_h) = \begin{cases} \infty & \text{for } x_h \notin \bar{\Omega}_h^I \\ g_h(x_h) & \text{for } x_h \in \bar{\Omega}_h^I \end{cases}$$

3. Do

For all grid elements σ :

For all vertices x_h in σ :

If $(|(\Lambda_h \tilde{\phi}_h)(x_h, \sigma) - \tilde{\phi}_h(x_h)| > \text{tol})$

$\tilde{\phi}_h(x_h) = (\Lambda_h \tilde{\phi}_h)(x_h, \sigma)$.

While (Hopf-Lax vertex update has been performed during grid traverse).

The algorithm finishes after a finite number of iterations because the monotonicity property is preserved in the restriction of the Hopf-Lax updates to elements. In the rest of the section we describe the algorithm for the calculation of the Hopf-Lax vertex update (2.19) in detail. It only makes use of geometric considerations. For dimensions two, it is quite short, the implementation only takes a few lines. The algorithm is given in [8]. We now describe an algorithm for dimensions three.

We denote $HL_2d(x_h, \sigma)$ and $HL_3d(x_h, \sigma)$ the Hopf-Lax vertex update for the vertex x_h in element σ for dimensions two and dimensions three respectively. To explain the algorithm we employ a geometric interpretation of the Hopf-Lax vertex update $HL_3d(x_h, \sigma)$. Denote u_h, v_h, w_h the vertices in the element σ in the face opposite to x_h . Now we rotate and translate σ in three-dimensional space in such a way that u_h has the height $\phi_h(u_h)$ over the x-y-plane, v_h the height $\phi_h(v_h)$ and w_h the height $\phi_h(w_h)$. That means the x-y-plane serves as an approximation of the interface, see the left picture in figure 2.4. If the perpendicular line from the rotated x_h

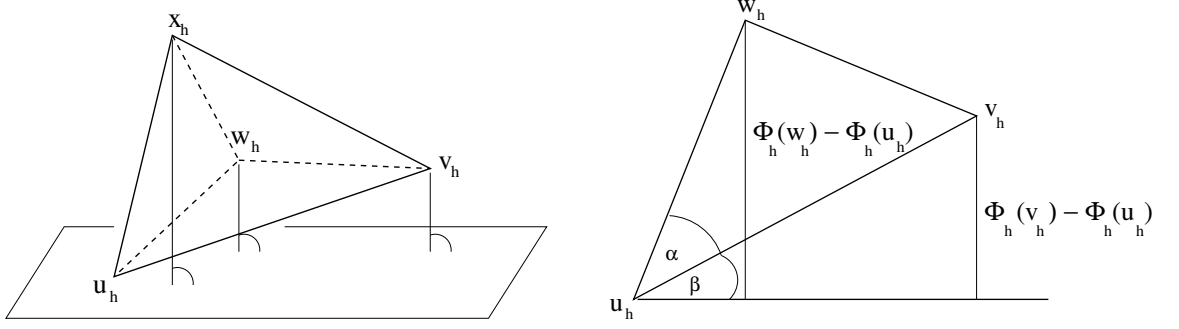


Figure 2.4: 3D-Hopf-Lax vertex update algorithm: Shows the rotation of an element with respect to ϕ_h (on the left) and restrictions to the existence of this rotation (on the right).

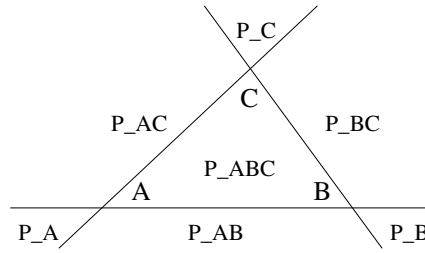


Figure 2.5: 3D-Hopf-Lax vertex update algorithm: Possible positions of the projection point D with respect to \triangle_{ABC} .

to the x-y-plane passes through $\triangle_{u_h v_h w_h}$ the Hopf-Lax vertex update is the distance of x_h to the x-y-plane. Else, we need further geometric arguments. Denote A the projection of u_h on the x-y-plane, B the projection of v_h , C the projection of w_h and D the projection of x_h . Then the position of D can be described by the areas defined in figure 2.5. Let $y(x_h)$ be defined through

$$y(x_h) = \operatorname{argmin}_{y \in \partial \omega_h(x_h) \cap \bar{\sigma}} (g_h(y) + |x_h - y|).$$

The position of D indicates the position of $y(x_h)$. For example, if D is situated in the area P_{AB} , the point $y(x_h)$ lies on the edge of σ containing u_h and v_h . That means the Hopf-Lax vertex update is obtained as the two-dimensional Hopf-Lax vertex update on a face of σ , namely

$$HL_3d(x_h, \sigma) = HL_2d(x_h, \triangle_{x_h u_h v_h}).$$

$$\begin{aligned} D \in P_{ABC} &: HL_3d(x_h, \sigma) = \text{distance of } x_h \text{ to x-y-plane} \\ D \in P_A &: HL_3d(x_h, \sigma) = \phi_h(u_h) + |x_h - u_h| \\ D \in P_B &: HL_3d(x_h, \sigma) = \phi_h(v_h) + |x_h - v_h| \\ D \in P_C &: HL_3d(x_h, \sigma) = \phi_h(w_h) + |x_h - w_h| \\ D \in P_{AB} &: HL_3d(x_h, \sigma) = HL_2d(x_h, \triangle_{x_h u_h v_h}) \\ D \in P_{AC} &: HL_3d(x_h, \sigma) = HL_2d(x_h, \triangle_{x_h u_h w_h}) \\ D \in P_{BC} &: HL_3d(x_h, \sigma) = HL_2d(x_h, \triangle_{x_h v_h w_h}) \end{aligned}$$

Table 2.1: 3D-Hopf-Lax vertex update algorithm: Calculation formula for the Hopf-Lax update depending on the position of D (see Figure 2.5).

Or, if D lies in the area P_C , we have $y(x_h) = w_h$. Thus, depending on the position of D , the three-dimensional Hopf-Lax vertex update can be calculated as in table 2.1. Our algorithm now consists in the following steps: first performing the above rotation with respect to the distances $\phi_h(u_h)$, $\phi_h(v_h)$ and $\phi_h(w_h)$, and then calculating the update as in table 2.1.

In some cases the rotation is not possible. Let us consider the rotation to be done in three steps: First we arrange the vertices u_h , v_h and w_h such that

$$\phi_h(u_h) \leq \phi_h(v_h) \leq \phi_h(w_h). \quad (2.20)$$

Then the edge $[u_h, v_h]$ is rotated appropriately. This is only possible if

$$\phi_h(v_h) - \phi_h(u_h) \leq |v_h - u_h|. \quad (2.21)$$

And finally we position the edge $[u_h, w_h]$. The right picture in figure 2.4 shows a rotation of $\Delta_{u_h v_h w_h}$ into the x-z-plane and illustrates that the second rotation is only possible if

$$0 \leq \alpha + \beta \leq \pi/2 \quad (2.22)$$

$$\frac{\phi_h(w_h) - \phi_h(u_h)}{|w_h - u_h|} \leq \sin(\alpha + \beta), \quad (2.23)$$

with the angles α and β defined in the figure. The algorithm for the three-dimensional Hopf-Lax vertex update $HL_3d(x_h, \sigma)$ is now given as follows:

1. Arrange u_h , v_h and w_h as in (2.20).
2. If (rotation of σ is possible, i.e. (2.21)-(2.23) are fulfilled)
 - Rotate σ and calculate $HL_3d(x_h, \sigma)$ as in table 2.1.
 - Else
 - $HL_3d(x_h, \sigma)$ is the minimum of the two-dimensional Hopf-Lax vertex updates for x_h on the faces of σ containing x_h .

The described algorithm is well suited for unstructured grids. Further speed up can be achieved by an ordered element traverse, in which elements near the interface are visited first.

Chapter 3

Isotropic evolution laws

To get started, we consider isotropic evolution, i.e. evolution where the normal velocity V does not depend on the orientation (given by the surface normal) of the moving surface. First of all we recall the well known evolution equations of mean curvature flow and surface diffusion and describe their numerical treatment with the level set method. Then, a model which combines mean curvature flow and surface diffusion is presented in the context of thin film epitaxy.

3.1 Isotropic mean curvature flow

Motion by mean curvature flow is described through the evolution law

$$V = -H,$$

i.e. the normal velocity is proportional to the mean curvature of the surface, and the motion direction depends on the sign of the mean curvature. Often the evolution equation is also considered in the more general version

$$V = -cH \tag{3.1}$$

with a positive coefficient c , where c may e.g. depend on the orientation of the surface, $c = c(\nu)$. In chapter 1 we have seen that motion by mean curvature flow models the singular phenomenon of attachment-detachment in the evolution of thin film surfaces.

The numerical solution of isotropic mean curvature flow, for the evolution of curves also called isotropic curve shortening flow, has already been broadly discussed in the literature. Deckelnick, Dziuk and Elliott have extensively investigated the subject and have provided numerous results, including error and stability analysis for a graph, level set and parametric treatment with finite elements, as well as computational results. See [23] for a review paper and the references therein for more details. A level set solution with finite differences has been delivered in [59].

We will now transform the evolution equation (3.1) into its level set description and show how it is numerically treated with finite elements. We consider the evolution of a d -dimensional surface in a domain $\Omega \subseteq \mathbb{R}^{d+1}$. With the level set representation of the geometric expressions presented in chapter 2, we can rewrite the evolution law in terms of the level set function $\phi : \Omega \times \mathbb{R}^{\geq 0} \rightarrow \mathbb{R}$. The level set description of the normal velocity V is given in (2.12) and the expression for the mean curvature in (2.14). Thus the level set formulation for the evolution law (3.1) reads

$$\frac{1}{c} \frac{\phi_t}{|\nabla\phi|} = \nabla \cdot \frac{\nabla\phi}{|\nabla\phi|}.$$

Multiplication with test functions, integration and integration by parts gives us the weak formulation

$$\int_{\Omega} \frac{1}{c} \frac{\phi_t}{|\nabla\phi|} \eta \, dx = - \int_{\Omega} \frac{\nabla\phi}{|\nabla\phi|} \cdot \nabla\eta \, dx$$

for all test functions $\eta \in C_0^\infty(\Omega)$. We discretize in space with linear finite elements and assume that the boundary of our domain of interest Ω is of polygonal shape. In all the equations considered in this work, we use the following semi-implicit time discretization scheme. First, the time derivative ϕ_t is approximated by $\frac{1}{\tau}(\phi^{k+1} - \phi^k)$, where τ is the timestep size, and second, all linear terms are treated implicitly and all non-linear terms explicitly. Here, this results in

$$\int_{\Omega} \frac{1}{c} \frac{\phi^{k+1}}{|\nabla\phi^k|_\delta} \eta \, dx - \int_{\Omega} \frac{1}{c} \frac{\phi^k}{|\nabla\phi^k|_\delta} \eta \, dx + \tau \int_{\Omega} \frac{\nabla\phi^{k+1}}{|\nabla\phi^k|_\delta} \cdot \nabla\eta \, dx = 0 \quad (3.2)$$

for all $\eta \in \mathcal{V}^h$ with the norm regularization $|\cdot|_\delta$ described in 2.3.3 accounting for small gradients in ϕ which may arise during evolution. As usual, ϕ^k is the finite element approximation of the level set function ϕ in timestep k . We do not use timestep adaption, so the timestep τ is fixed throughout a computational evolution run and does not depend on k . The boundary in timestep k is approximated by the zero level line of ϕ^k of polygonal shape.

To describe the linear system which has to be solved in each timestep, we introduce the following notations for mass and stiffness matrices. For a function $f : \Omega \rightarrow \mathbb{R}$, a linear operator $A : \mathbb{R}^{d+1} \rightarrow \mathbb{R}^{d+1}$ and basis functions $(\varphi_i)_{i=1\dots N}$ of the finite element space \mathcal{V}^h we define

$$\begin{aligned} M[f] &:= \left(\int_{\Omega} f \varphi_i \varphi_j \, dx \right)_{ij}, \\ L[f] &:= \left(\int_{\Omega} f \nabla\varphi_i \cdot \nabla\varphi_j \, dx \right)_{ij}, \\ L[A] &:= \left(\int_{\Omega} A \nabla\varphi_i \cdot \nabla\varphi_j \, dx \right)_{ij}. \end{aligned}$$

With the system matrices

$$\begin{aligned} M_1 &:= M\left[\frac{1}{c} |\nabla\phi^k|_\delta^{-1}\right], \\ L_1 &:= L\left[|\nabla\phi^k|_\delta^{-1}\right] \end{aligned}$$

and the linear expansion

$$\phi^k = \sum_{i=1}^N \bar{\phi}_i^k \varphi_i$$

the linear system to be solved in timestep $k+1$ reads

$$\left(M_1 + \tau L_1 \right) \bar{\phi}^{k+1} = M_1 \bar{\phi}^k.$$

It is symmetric and positive definite. The system is solved with the conjugate gradient method.

Variational formulation

The evolution equation for mean curvature flow can be derived within a variational formulation with the energy or area functional

$$E[\Gamma] = \int_{\Gamma} dA. \quad (3.3)$$

The variational derivative with respect to variations in normal direction of this functional is

$$\frac{\delta E}{\delta \Gamma} = H. \quad (3.4)$$

Equation (3.1) thus gives the evolution of the surface Γ in the direction of the negative variational derivative. It is the L^2 -gradient flow of the energy functional (3.3) and describes evolution in the direction of steepest energy decrease with respect to the L^2 -metric.

Energy dissipation

Energy dissipation is required for a thermodynamically consistent model. From the variational formulation it is clear, that evolution under mean curvature flow decreases the energy (3.3). Another approach to proof energy dissipation is to show

$$\frac{d}{dt} E[\Gamma(t)] \leq 0,$$

which we will also use later on to show energy dissipation for surface diffusion. Equations (2.9), (3.1) and (3.4) give

$$\frac{d}{dt} E[\Gamma(t)] = \int_{\Gamma(t)} V \frac{\delta E}{\delta \Gamma} dA = - \int_{\Gamma(t)} c \left(\frac{\delta E}{\delta \Gamma} \right)^2 dA \leq 0.$$

In the physical context of thin film growth, the functional (3.3) provides the surface free energy. The surface chemical potential in the model of attachment-detachment is given through the variational derivative $\frac{\delta E}{\delta \Gamma}$.

3.2 Isotropic surface diffusion

Motion by surface diffusion is described through the evolution law

$$V = \Delta_{\Gamma} H$$

or in a more general version

$$V = \nabla_{\Gamma} \cdot (m \nabla_{\Gamma} H) \quad (3.5)$$

with the diffusion flux $\nabla_{\Gamma} H$ along the surface and the non-negative diffusion or mobility coefficient m . The surface moves fast in regions where the Laplacian of the mean curvature is large. In regions with constant mean curvature, e.g. on a circle or a sphere, the evolution is stationary.

There are several works on the numerical solution of isotropic surface diffusion in the literature. In [59] and [19] a level set solution with finite differences is presented. The author in [59] develops a semi-implicit time discretization scheme which allows for timestep sizes $\tau \approx Ch^2$. To compare, an explicit scheme of the 4th-order equation demands $\tau \approx Ch^4$. A solution with finite elements within the graph and parametric setting is given in [3] and [4] respectively.

With (2.12) and (2.16), we obtain the level set formulation for (3.5) through

$$-\phi_t = \nabla \cdot \left(m |\nabla \phi| P_{\Gamma} \nabla \left(\nabla \cdot \frac{\nabla \phi}{|\nabla \phi|} \right) \right).$$

This is a 4th order equation. With linear finite elements only equations with the highest order two can be discretized. We split up the equation into a system of two second order equations, which reads

$$\begin{aligned} -\phi_t &= \nabla \cdot \left(m |\nabla \phi| P_{\Gamma} \nabla \omega \right) \\ \omega &= \nabla \cdot \frac{\nabla \phi}{|\nabla \phi|}. \end{aligned}$$

Again, we apply integration by parts, and obtain the weak formulation

$$\begin{aligned}\int_{\Omega} \phi_t \eta \, dx &= \int_{\Omega} m |\nabla \phi| P_{\Gamma} \nabla \omega \cdot \nabla \eta \, dx \\ \int_{\Omega} \omega \xi \, dx &= - \int_{\Omega} \frac{\nabla \phi}{|\nabla \phi|} \cdot \nabla \xi \, dx\end{aligned}$$

for all test functions $\eta, \xi \in C_0^\infty(\Omega)$. Time discretization is done in the same semi-implicit way as in the mean curvature case and results in the following system of equations

$$\begin{aligned}\int_{\Omega} \phi^{k+1} \eta \, dx - \int_{\Omega} \phi^k \eta \, dx - \tau \int_{\Omega} m |\nabla \phi^k|_{\delta} P_{\Gamma}^k \nabla \omega^{k+1} \cdot \nabla \eta \, dx &= 0 \\ \int_{\Omega} \omega^{k+1} \xi \, dx + \int_{\Omega} \frac{\nabla \phi^{k+1}}{|\nabla \phi^k|_{\delta}} \cdot \nabla \xi \, dx &= 0\end{aligned}$$

for all $\eta, \xi \in \mathcal{V}^h$, where P_{Γ}^k is the discrete projection operator

$$P_{\Gamma}^k = I - \nu^k \otimes \nu^k = I - \frac{\nabla \phi^{k+1}}{|\nabla \phi^k|} \otimes \frac{\nabla \phi^{k+1}}{|\nabla \phi^k|}.$$

We define the system matrices

$$\begin{aligned}M_1 &:= M[1], \\ L_1 &:= L[m |\nabla \phi^k|_{\delta} P_{\Gamma}^k], \\ L_2 &:= L[|\nabla \phi^k|_{\delta}^{-1}].\end{aligned}$$

With the linear expansions

$$\phi^k = \sum_{i=1}^N \bar{\phi}_i^k \varphi_i, \quad \omega^k = \sum_{i=1}^N \bar{\omega}_i^k \varphi_i$$

the linear system to be solved in timestep $k+1$ reads

$$\begin{pmatrix} M_1 & -\tau L_1 \\ L_2 & M_1 \end{pmatrix} \begin{pmatrix} \bar{\phi}^{k+1} \\ \bar{\omega}^{k+1} \end{pmatrix} = \begin{pmatrix} M_1 \bar{\phi}^k \\ 0 \end{pmatrix}. \quad (3.6)$$

This is a non-symmetric linear system of dimension $2N$. We are only interested in the unknown $\bar{\phi}^{k+1}$, and do not need the second variable. We use a similar approach as the authors in [3] and solve the system with a Schur complement approach which results in the non-symmetric linear system of dimension N

$$\left(M_1 + \tau L_1 M_1^{-1} L_2 \right) \bar{\phi}^{k+1} = M_1 \bar{\phi}^k.$$

The inverse M_1^{-1} is approximated with mass lumping. We solve the linear system with the Krylov subspace method BiCGStab2 allowing for arbitrary regular matrices.

Other solution approaches

Another approach consists in solving the linear system (3.6) as a system of dimension $2N$. There exist various possibilities to do so. Comparing the matrices L_1 and L_2 , the size of the components may differ significantly, leading to a bad conditioned system. Preconditioning is probably essential, on the one hand to cope with a bad conditioned system and on the other

hand to reduce computational time. We did computational experiments solving (3.6) as a system in its symmetric and positive definite version, which is reached by exchanging the sequence of the equations. We used a conjugate gradient solver and applied diagonal preconditioning. However, the solver needed a high number of iterations. More sophisticated preconditioning, e.g. multigrid preconditioning, should help to improve this point. With respect to volume conservation the Schur complement approach produced better results.

In [3] and [5] a Schur complement approach is used for symmetric systems resulting from the solution of surface diffusion in a graph and parametric setting respectively. In [5] a diagonal preconditioning scheme is proposed. The effect of the preconditioning is measured by the computational time used for the unpreconditioned and preconditioned system. The authors state, that in most considered examples, there is only a minor speed up in time.

Second order time discretization with Crank-Nicolson

As further time discretization scheme we have considered second order Crank-Nicolson time discretization for parabolic equations. It also results in a non-symmetric linear system. But in numerical experiments the semi-implicit time discretization showed to be more accurate and allowed for bigger timesteps.

Energy dissipation and volume conservation

With the evolution law (3.5), equations (2.9) and (3.4) and integration by parts on surfaces (2.4) we obtain

$$\frac{d}{dt}E[\Gamma(t)] = \int_{\Gamma(t)} V \frac{\delta E}{\delta \Gamma} dA = \int_{\Gamma(t)} \nabla_{\Gamma} \cdot \left(m \nabla_{\Gamma} \frac{\delta E}{\delta \Gamma} \right) \frac{\delta E}{\delta \Gamma} dA = - \int_{\Gamma(t)} m \left(\nabla_{\Gamma} \frac{\delta E}{\delta \Gamma} \right)^2 dA \leq 0,$$

which shows the thermodynamic consistency of the evolution law (3.5). Isotropic surface diffusion is the H^{-1} -gradient flow of the energy functional (3.3).

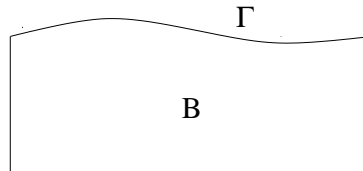


Figure 3.1: Solid phase B and evolving surface Γ , which is part of the boundary ∂B .

We first verify volume conservation for closed surfaces. $B(t)$ is the domain enclosed by the surface $\Gamma(t)$ and $\partial B(t) = \Gamma(t)$. Equations (2.8), (3.5) and (3.4) and integration by parts on surfaces provide

$$\frac{d}{dt} \text{volume}(t) = \int_{\Gamma(t)} V dA = \int_{\Gamma(t)} \nabla_{\Gamma} \cdot \left(m \nabla_{\Gamma} \frac{\delta E}{\delta \Gamma} \right) \cdot 1 dA = - \int_{\Gamma(t)} m \left(\nabla_{\Gamma} \frac{\delta E}{\delta \Gamma} \right) \cdot \nabla_{\Gamma} 1 dA = 0.$$

In physical context, this volume conserving property is often called mass conservation. In the situation of non-closed surfaces, the evolving surface Γ is not equal to the boundary of $B(t)$. Figure 3.1 illustrates the situation. But only the portion $\Gamma(t)$ of the boundary ∂B changes in time, that means the normal velocity V is zero on $\partial B(t) \setminus \Gamma(t)$. Thus

$$\int_{\partial B(t)} V dA = \int_{\Gamma(t)} V dA,$$

and we obtain volume conservation as above. For this reason, we do not have to distinguish between closed and non-closed surfaces in further volume conserving analysis.

3.3 Isotropic kinetic model

The evolution equations of mean curvature flow and surface diffusion discussed so far each model singular phenomena in thin film epitaxy. We now come to a model which includes both phenomena. In [33] a model for thin film growth is presented which combines the effects of attachment-detachment and surface diffusion, and incorporates influences from the solid and vapour phases. It has been derived within the framework of configurational forces. In [64] a different derivation based on more standard variational concepts is given. We first of all present the model, where we follow the approach in [64] for our explanations, and then come to the level set treatment and numerical solution. In the description of the model we use "+" for the solid and "-" for the vapour phase. In addition to the models of attachment-detachment and surface diffusion described in chapter 1, the model in [64] considers mass supply from the vapour, which is given by the difference between the surface chemical potential μ and the chemical potential in the vapour μ^- through $-c(\mu - \mu^-)$, where c is the attachment rate, which may depend on the orientation of the surface ($c = c(\nu)$). The model accounts for a material flux j from the solid, and the normal velocity V therein also depends on the grand canonical potential $\psi^+ - \rho\mu$ in the solid with ρ the density in the solid. The model in [64] is a system of two equations and reads

$$\rho V = \nabla_{\Gamma} \cdot (m \nabla_{\Gamma} \mu) + j \cdot \nu - c(\mu - \mu^-) \quad (3.7)$$

$$bV = -\frac{\delta E}{\delta \Gamma} - \psi^+ + \rho\mu. \quad (3.8)$$

$b = b(\nu)$ is a non-negative kinetic and $m = m(\nu)$ a non-negative mobility coefficient. The first equation results from the local mass balance property, whereas the second equation incorporates a new kinetic effect or mass transport mechanism in the system. We will show its relation to the classical equations of mean curvature flow and surface diffusion later on. In this work, we concentrate on models with only contributions from the film surface (solid-vapour interface) and restrict to the density $\rho = 1$. If with $j = \mu^- = \psi^+ = 0$ we neglect the influence from the solid and the vapour in (3.7) and (3.8) and set $\rho = 1$, we obtain

$$V = \nabla_{\Gamma} \cdot (m \nabla_{\Gamma} \mu) - c\mu \quad (3.9)$$

$$bV = -\frac{\delta E}{\delta \Gamma} + \mu. \quad (3.10)$$

We note that, considering only equation (3.10), the chemical potential μ now does not only depend on the variational derivative of the surface free energy, but includes in addition a kinetic component by the relation to the normal velocity. Again, we consider the surface free energy (3.3) with its variational derivative $\frac{\delta E}{\delta \Gamma} = H$, thus in our considerations of isotropic surface energies equations (3.9) and (3.10) read

$$V = \nabla_{\Gamma} \cdot (m \nabla_{\Gamma} \mu) - c\mu \quad (3.11)$$

$$bV = -H + \mu. \quad (3.12)$$

Written as one equation this gives

$$V = \nabla_{\Gamma} \cdot (m \nabla_{\Gamma} (bV + H)) - c\mu.$$

For $c = 0$ the authors in [15] have transformed this equation into an expression for the normal velocity V which reads

$$V = -(\nabla_{\Gamma} \cdot (m \nabla_{\Gamma})) (\nabla_{\Gamma} \cdot (m \nabla_{\Gamma}) - \frac{1}{b})^{-1} \left(\frac{1}{b} H \right). \quad (3.13)$$

In [15] it is shown that choosing a large mobility coefficient ($m = \infty$) provides the volume preserving motion by the difference between mean curvature and the average mean curvature $C(\Gamma) = \int_{\Gamma} \frac{1}{b} H dA / \int_{\Gamma} \frac{1}{b} dA$, which is given through the evolution law

$$V = -\frac{1}{b}(H - C(\Gamma)).$$

The volume conserving property is easily verified with (2.8) through

$$\begin{aligned} \frac{d}{dt} \text{volume}(t) &= - \int_{\Gamma(t)} \frac{1}{b} H dA + \int_{\Gamma(t)} \frac{1}{b} \left(\int_{\Gamma(t)} \frac{1}{b} H dA / \int_{\Gamma(t)} \frac{1}{b} dA \right) dA \\ &= - \int_{\Gamma(t)} \frac{1}{b} H dA + \int_{\Gamma(t)} \frac{1}{b} H dA = 0. \end{aligned}$$

Motion by the difference between mean curvature and the average mean curvature models a kinetic effect which is due to the rearrangement of adatoms. Adatoms diffuse infinitely fast. This effect is called surface kinetics.

For specific choices of the coefficients, we regain the evolution laws in sections 3.1 and 3.2. With $b = m = 0$, equations (3.11) and (3.12) are the evolution law for mean curvature flow (3.1). And with $b = c = 0$, we get the evolution law for surface diffusion (3.5). For $c = 0$ equations (3.11) and (3.12) combine surface diffusion and surface kinetics. We will briefly call this evolution surface diffusion with kinetics.

With (2.12), (2.14) and (2.16) we obtain the level set formulation of equations (3.11) and (3.12) through

$$\begin{aligned} \phi_t &= -\nabla \cdot (m|\nabla\phi|P_{\Gamma}\nabla\mu) + c|\nabla\phi|\mu \\ b \frac{\phi_t}{|\nabla\phi|} &= \nabla \cdot \frac{\nabla\phi}{|\nabla\phi|} - \mu. \end{aligned}$$

Again with integration by parts, we get the weak formulation

$$\begin{aligned} \int_{\Omega} \phi_t \eta dx &= \int_{\Omega} m|\nabla\phi|P_{\Gamma}\nabla\mu \cdot \nabla\eta dx + \int_{\Omega} c|\nabla\phi|\mu\eta dx \\ \int_{\Omega} b \frac{\phi_t}{|\nabla\phi|} \xi dx &= - \int_{\Omega} \frac{\nabla\phi}{|\nabla\phi|} \cdot \nabla\xi dx - \int_{\Omega} \mu\xi dx \end{aligned}$$

for all test functions $\eta, \xi \in C_0^{\infty}(\Omega)$, and discretization and norm regularization results in

$$\begin{aligned} \int_{\Omega} \phi^{k+1} \eta dx - \int_{\Omega} \phi^k \eta dx - \tau \int_{\Omega} m|\nabla\phi^k|_{\delta} P_{\Gamma}^k \nabla\mu^{k+1} \cdot \nabla\eta dx - \tau \int_{\Omega} c|\nabla\phi^k|_{\delta} \mu^{k+1} \eta dx &= 0 \\ \int_{\Omega} b \frac{\phi^{k+1}}{|\nabla\phi^k|_{\delta}} \xi dx - \int_{\Omega} b \frac{\phi^k}{|\nabla\phi^k|_{\delta}} \xi dx + \tau \int_{\Omega} \frac{\nabla\phi^{k+1}}{|\nabla\phi^k|_{\delta}} \cdot \nabla\xi dx + \tau \int_{\Omega} \mu^{k+1} \xi dx &= 0 \end{aligned}$$

for all $\eta, \xi \in \mathcal{V}^h$. We define the system matrices

$$\begin{aligned} M_1 &:= M[1], & L_1 &:= L[m|\nabla\phi^k|_{\delta} P_{\Gamma}^k], \\ M_2 &:= M[c|\nabla\phi^k|_{\delta}], & L_2 &:= L[|\nabla\phi^k|_{\delta}^{-1}], \\ M_3 &:= M[b|\nabla\phi^k|_{\delta}^{-1}], \end{aligned}$$

and with the linear expansions

$$\phi^k = \sum_{i=1}^N \bar{\phi}_i^k \varphi_i, \quad \mu^k = \sum_{i=1}^N \bar{\mu}_i^k \varphi_i$$

the linear system to be solved in timestep $k+1$ reads

$$\begin{pmatrix} M_1 & -\tau M_2 - \tau L_1 \\ M_3 + \tau L_2 & \tau M_1 \end{pmatrix} \begin{pmatrix} \bar{\phi}^{k+1} \\ \bar{\mu}^{k+1} \end{pmatrix} = \begin{pmatrix} M_1 \bar{\phi}^k \\ M_3 \bar{\phi}^k \end{pmatrix}.$$

Again, the system is solved with a Schur complement approach which gives

$$\left(M_1 + (M_2 + L_1)M_1^{-1}(M_3 + \tau L_2) \right) \bar{\phi}^{k+1} = M_1 \bar{\phi}^k + (M_2 + L_1)M_1^{-1}M_3 \bar{\phi}^k.$$

The inverse M_1^{-1} is approximated with mass lumping. The non-symmetric linear system is solved with the Krylov subspace method BiCGStab2.

Energy dissipation and volume conservation

We show energy dissipation and volume conservation for the form (3.9) and (3.10) of the kinetic model with a general energy. With (2.9) and (3.9), integration by parts on surfaces and the transformation

$$\frac{\delta E}{\delta \Gamma} = \mu - bV$$

of (3.10), energy dissipation follows from

$$\begin{aligned} \frac{d}{dt} E[\Gamma(t)] &= \int_{\Gamma(t)} V \frac{\delta E}{\delta \Gamma} dA \\ &= \int_{\Gamma(t)} V \mu dA - \int_{\Gamma(t)} bV^2 dA \\ &= \int_{\Gamma(t)} \nabla_{\Gamma} \cdot (m \nabla_{\Gamma} \mu) \mu dA - \int_{\Gamma(t)} c\mu^2 dA - \int_{\Gamma(t)} bV^2 dA \\ &= - \int_{\Gamma(t)} m (\nabla_{\Gamma} \mu)^2 dA - \int_{\Gamma(t)} c\mu^2 dA - \int_{\Gamma(t)} bV^2 dA \\ &\leq 0. \end{aligned}$$

And with (2.8) and (3.9) the change of mass in the solid phase, which is equal to the geometrically measured volume of $B(t)$, amounts to

$$\frac{d}{dt} mass(t) = \int_{\Gamma(t)} V dA = \int_{\Gamma(t)} \nabla_{\Gamma} \cdot (m \nabla_{\Gamma} \mu) - c\mu dA = - \int_{\Gamma(t)} c\mu dA.$$

Thus for the attachment rate $c = 0$, evolution of a surface under the kinetic model is volume conserving.

3.4 Numerical results

We now discuss computational results for the three presented models. For attachment-detachment, we use the parameter $c = 1.0$ in all examples, and for surface diffusion we apply the mobility constant $m = 1.0$. The kinetic model is analyzed for different choices of parameters.

3.4.1 Mean curvature flow

Validation of computational results. First of all, we show that for the evolution of a circle and a sphere under mean curvature flow our numerical computations converge to the correct

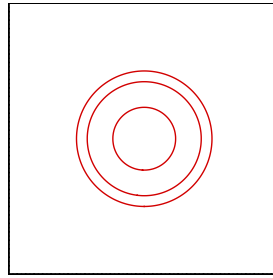


Figure 3.2: Evolution of curve under mean curvature flow. $[0, 4] \times [0, 4]$ grid, grid size $h = 0.03125$, timestep $\Delta t = 0.00097$. From outer to inner circle: $t = 0.0, 0.1455, 0.388$.

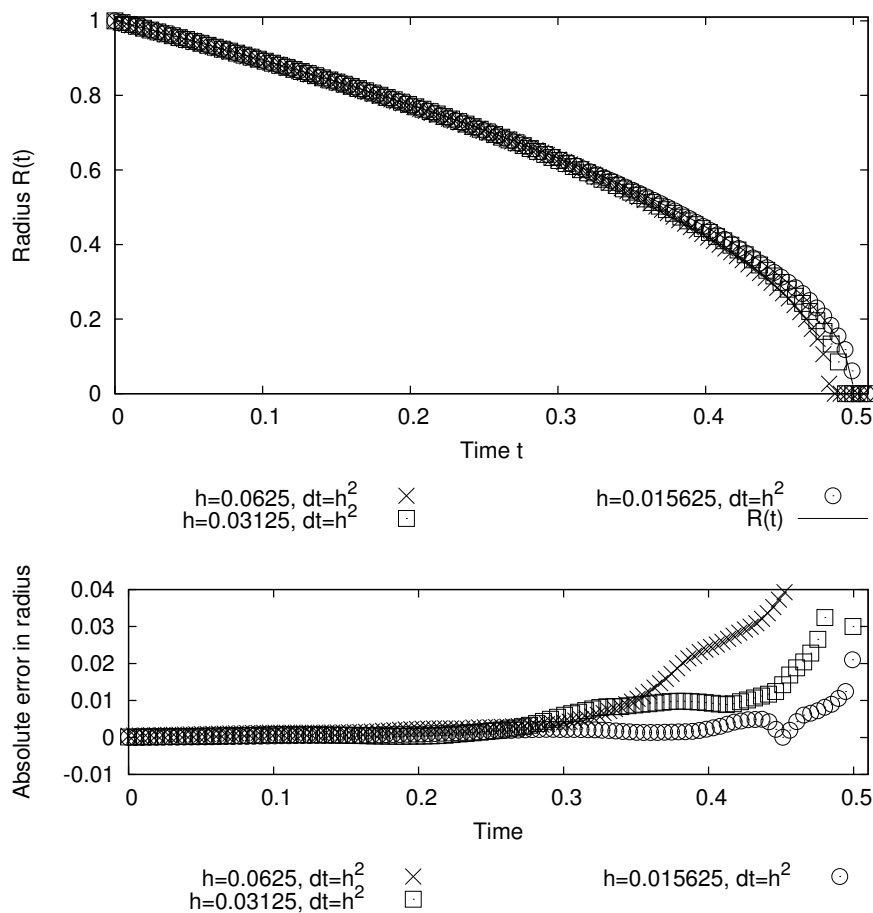


Figure 3.3: Convergence of mean curvature flow: evolution of a circle with initial radius $R_0 = 1.0$ with different grid sizes and timesteps, see figure 3.2. Above: comparison of the exact evolution of the circle with computational results with grid sizes $h = 0.0625$, $h = 0.03125$ and $h = 0.015625$ and timestep $\Delta t = h^2$. Below: absolute error in the radius.

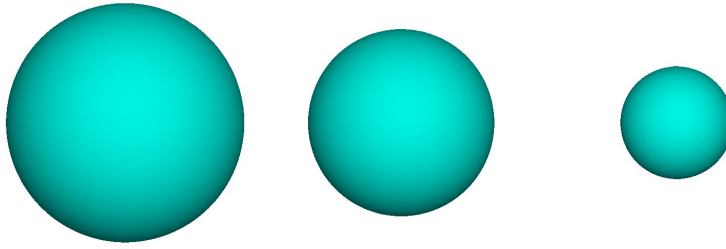


Figure 3.4: Evolution of surface under mean curvature flow. $[0, 4] \times [0, 4] \times [0, 4]$ grid, grid size $h = 0.03125$, timestep $\Delta t = 0.00097$. From left to right: $t = 0.0, 0.097, 0.194$.

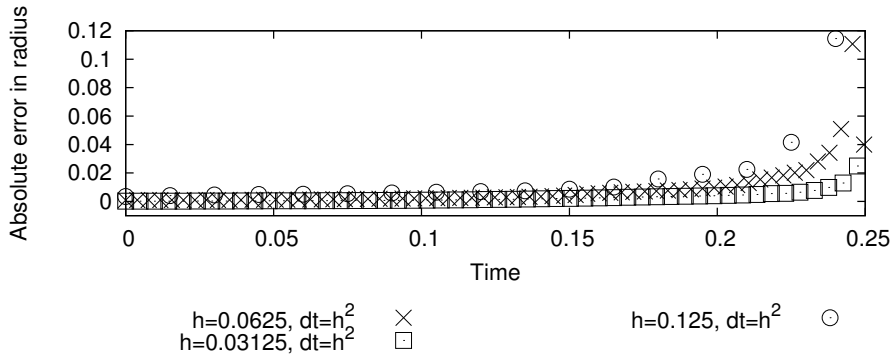


Figure 3.5: Convergence of mean curvature flow: evolution of a sphere with initial radius $R_0 = 1.0$ with different grid sizes and timesteps, see figure 3.4. Absolute error in the radius for grid sizes $h = 0.125$, $h = 0.0625$ and $h = 0.03125$ and timestep $\Delta t = h^2$.

solution as the grid size h tends to zero. Here, the analytical solution is known. A circle with radius R_0 at time $t = 0$, which evolves under mean curvature flow, has the radius

$$R(t) = \sqrt{R_0^2 - 2t}$$

at time t . And the radius of a sphere evolving under mean curvature flow with initial radius R_0 is at time t

$$R(t) = \sqrt{R_0^2 - 4t}.$$

Figure 3.2 shows the evolution of a circle with initial radius $R_0 = 1.0$. Figure 3.3 illustrates for different grid sizes h , the development of the radius in time and the absolute error in the radius. The timestep size is always chosen in dependence on the grid size by $\Delta t = h^2$. The figure demonstrates the desired convergence behavior. As expected, the largest errors occur near $t = 0.5$, where the circle shrinks to a point and the grid size is too large with respect to the small radius.

Figure 3.5 shows similar convergence results for the evolution of a sphere with initial radius $R_0 = 1.0$. The evolution is presented in figure 3.4.

Closed curves and surfaces. In figure 3.6, we consider the evolution of a square-shaped closed curve under mean curvature flow. First the corners are rounded, since the mean curvature is largest in these areas. The figure shows the characteristic behavior of mean curvature flow for closed curves: the shape becomes circular and shrinks to a point. Figure 3.7 gives the same evolutionary behavior for a cube. Both figures reveal a further characteristic of mean curvature flow: the enclosed domain, which is initially convex, stays convex under evolution.

Non-closed curves and surfaces. Figure 3.8 shows the evolution under mean curvature flow of a sine function which is overlaid by a sine function with higher frequency. As expected,

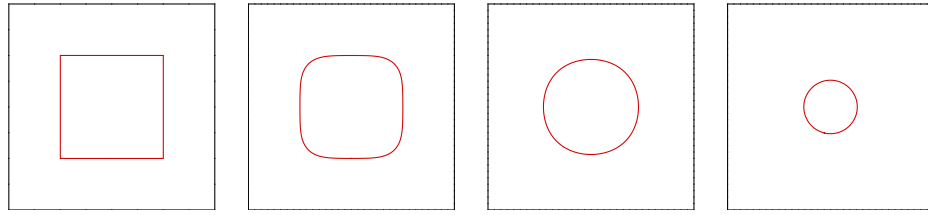


Figure 3.6: Evolution of curve under mean curvature flow. $[0, 4] \times [0, 4]$ grid, grid size $h = 0.03125$, timestep $\Delta t = 0.001$. From left to right: $t = 0.0, 0.02, 0.2, 0.5$.

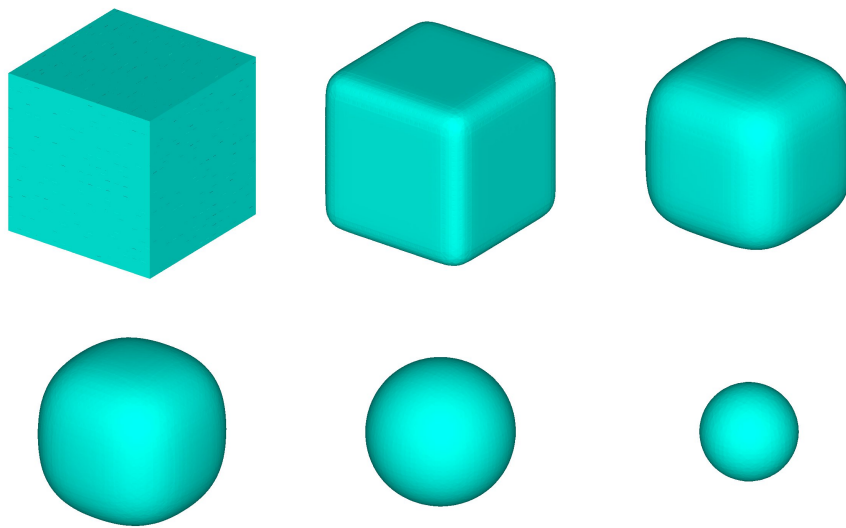


Figure 3.7: Evolution of surface under mean curvature flow. $[0, 4] \times [0, 4] \times [0, 4]$ grid, grid size $h = 0.05$, timestep $\Delta t = 0.001$. From top left to bottom right: $t = 0.0, 0.01, 0.05, 0.1, 0.2, 0.3$.

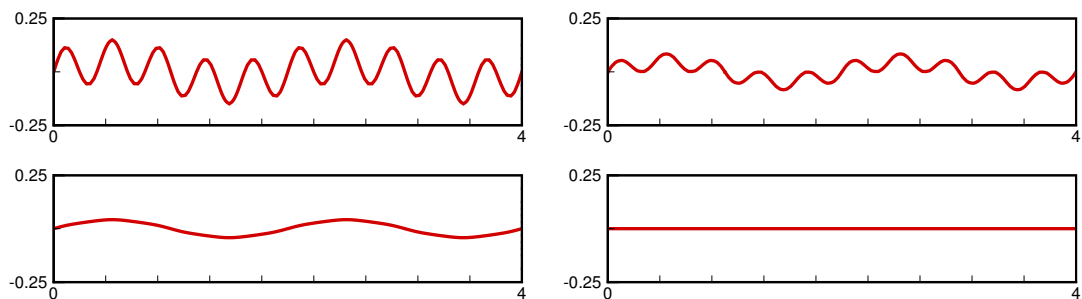


Figure 3.8: Evolution of curve under mean curvature flow. $[0, 4] \times [-1, 1]$ grid, grid size $h = 0.03125$, timestep $\Delta t = 0.001$. From top left to bottom right: $t = 0.0, 0.005, 0.02, 1.0$.

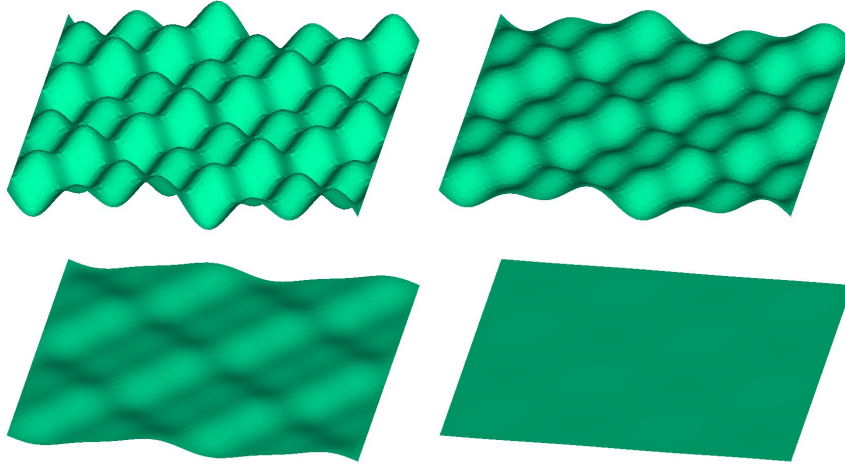


Figure 3.9: Evolution of surface under mean curvature flow. $[-2, 2] \times [-2, 2] \times [-0.5, -0.5]$ grid, grid size $h = 0.05$, timestep $\Delta t = 0.001$. From top left to bottom right: $t = 0.0, 0.01, 0.03, 0.2$.

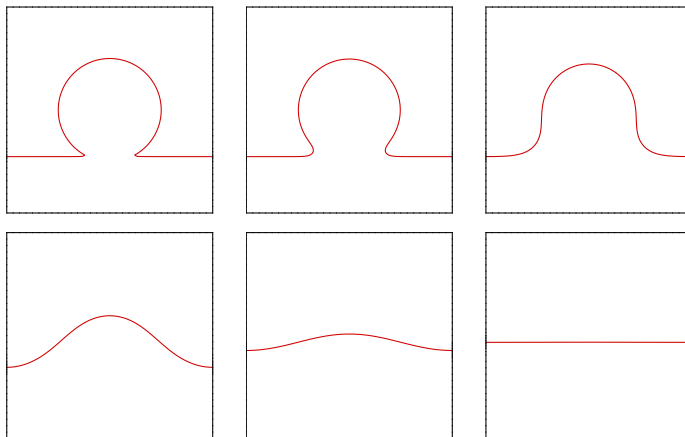


Figure 3.10: Evolution of curve under mean curvature flow. $[0, 4] \times [0, 4]$ grid, grid size $h = 0.03125$, timestep $\Delta t = 0.001$. From top left to bottom right: $t = 0.0, 0.01, 0.1, 0.5, 1.0, 3.0$.

first the higher frequencies are damped out, since the curvature is higher than for the lower frequencies. Then the lower frequencies are damped on a larger time scale and the curve reaches its energy minimizing shape, which in case of non-closed curves is a straight line. Figure 3.9 gives the corresponding example in 3D. It shows the evolution of a wave-like surface towards a flat surface, where high mean curvature areas are smoothed out first.

Another example for the evolution of a non-closed curve under mean curvature flow is given in figure 3.10. It starts with an omega-like shape, which is an example for a non-closed curve that cannot be represented as the graph of a function. The final evolution of the curve to the straight line occurs on a large time scale, since the curvature is small.

3.4.2 Surface diffusion

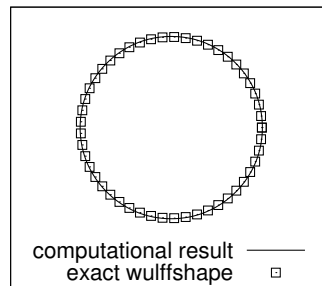


Figure 3.11: Comparison of computational result and exact wulffshape for the evolution of a curve with the initial shape of a square under surface diffusion, see figure 3.12 for the evolution.

Validation of computational results. As a validation of our computational results we graphically compare the equilibrium shape reached for the evolution of a square-like shape under surface diffusion with the predicted shape (wulffshape), which is a circle, since the evolution is isotropic. Figure 3.11 shows that the computational result matches the predicted one. The evolution leads to a minor increase in volume of about 1.5%. The evolution is shown in figure 3.12.

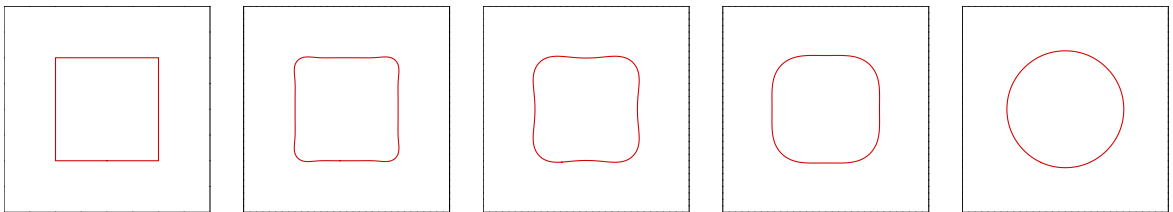


Figure 3.12: Evolution of curve under surface diffusion. $[0, 4] \times [0, 4]$ grid, grid size $h = 0.03125$, timestep $\Delta t = 10^{-6}$. From left to right: $t = 0.0, 0.0001, 0.001, 0.005, 0.1$.

Closed curves and surfaces. The evolution of a square-like shape under surface diffusion towards the circular equilibrium shape is given in figure 3.12. As in the mean curvature flow situation, the evolution starts in the corners of the square, since here, the curvature changes fast. The evolution is about ten times faster than for mean curvature flow. The corresponding 3D example is given in figure 3.13. A cube evolves under surface diffusion towards a sphere which is the equilibrium shape for closed surfaces.

In difference to mean curvature flow, an initially convex shape may become non-convex under evolution in the surface diffusion case. This is the case for both examples as the figures show, and can especially be observed quite well in the 3D example.

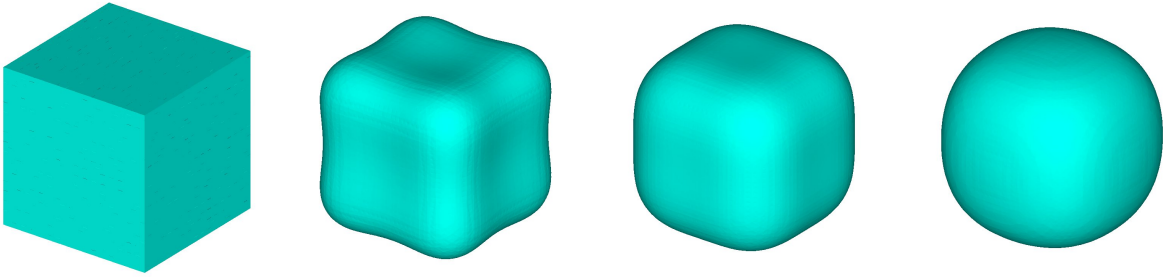


Figure 3.13: Evolution of surface under surface diffusion. $[0, 4] \times [0, 4] \times [0, 4]$ grid, grid size $h = 0.05$, timestep $\Delta t = 10^{-6}$. From left to right: $t = 0.0, 0.001, 0.005, 0.01$.

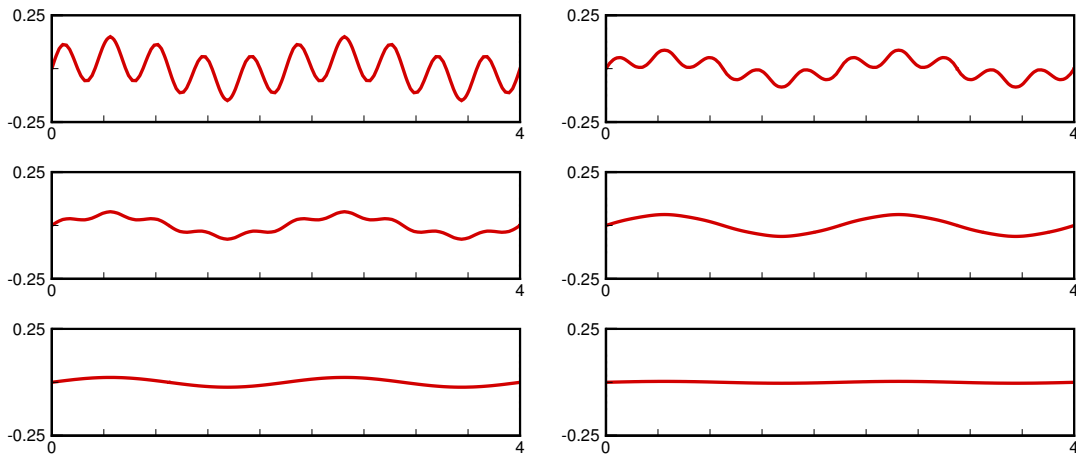


Figure 3.14: Evolution of curve under surface diffusion. $[0.4] \times [-1, 1]$ grid, grid size $h = 0.032$, timestep $\Delta t = 10^{-6}$. From top left to bottom right: $t = 0.0, 0.00003, 0.00005, 0.0001, 0.01, 0.1$.

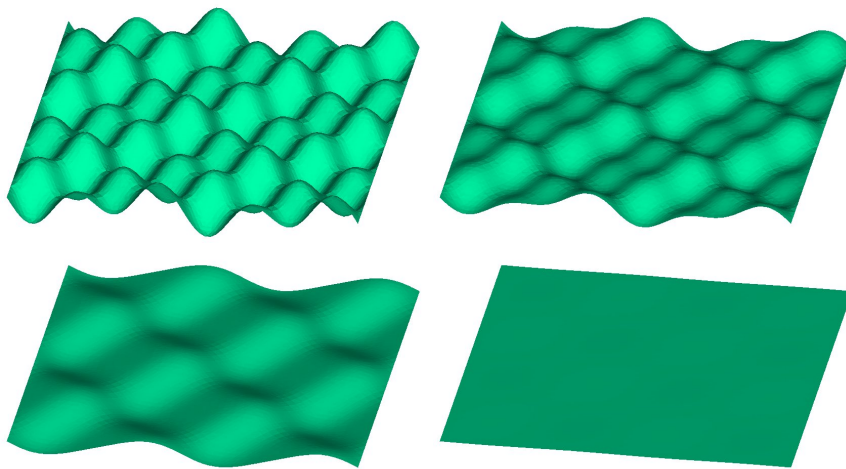


Figure 3.15: Evolution of surface under surface diffusion. $[-2, 2] \times [-2, 2] \times [-0.5, 0.5]$ grid, grid size $h = 0.05$, timestep $\Delta t = 10^{-5}$. From top left to bottom right: $t = 0.0, 0.0002, 0.0005, 0.01$.

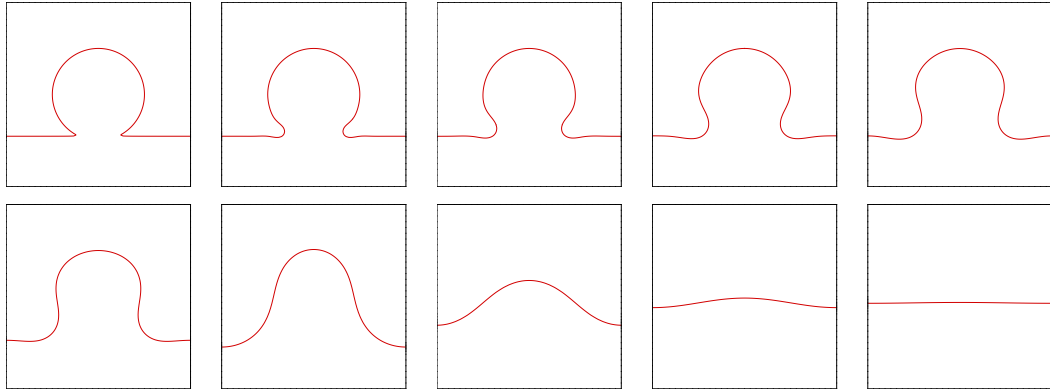


Figure 3.16: Evolution of curve under surface diffusion. $[0, 4] \times [0, 4]$ grid, grid size $h = 0.03125$, timestep $\Delta t = 10^{-6}$. From left to right: $t = 0.0, 0.0001, 0.0005, 0.002, 0.005, 0.01, 0.05, 0.5, 1.0, 5.0$.

Non-closed curves and surfaces. In figure 3.14, we consider the evolution of an overlaid sine function towards a flat line under surface diffusion. The higher frequencies are damped much faster than under mean curvature flow. In the example, the volume change is at most 0.002%. The 3D counterpart is given in the evolution of a wave-like surface towards a flat surface in figure 3.15.

The evolution of the omega-like shape under surface diffusion again reveals a change from a convex to a non-convex area in the corners at the beginning of the evolution. With respect to the reached shape, first surface diffusion is again about ten times faster than mean curvature flow, but the evolution of a nearly flat to a flat line takes more time than for mean curvature flow, which is due to the low curvature changes in this situation.

Pinch-off. We finally present two similar examples for topology changes under surface diffusion. In figure 3.17 initially two circles are connected by two narrow straight lines. Under evolution the two lines touch in two different places and pinch off in three parts, which finally each develop to a circle. In figure 3.18 the connecting part is shorter. The closed curve pinches off into two parts, and the evolution finally results in two circles. In the example in figure 3.17 the volume loss is about 0.8%, and in the example in figure 3.18 a volume loss of about 0.3% occurs.

Volume conservation and energy dissipation. As another check of the correctness of our computations, we control the volume conservation under evolution and the energy dissipation. In all examples presented for surface diffusion the mass change is at most about 1.5%. See figures 3.19 for the change of volume and the energy dissipation under evolution for the example in figure 3.16.

3.4.3 Kinetic model

After checking computational results against results from mean curvature flow and surface diffusion, the focus of the numerical examples will be on the influence of the parameter b on the evolution. The authors in [33] suppose, that the kinetic term bV in the second equation is negligible for small values of b . Our numerical results confirm this supposition for values of b chosen in the magnitude of 0.001 or smaller. But for larger values, a difference in the evolution velocity is clearly visible. For the parameter choice $b = 1.0$ surface diffusion with kinetics behaves like volume-conserving mean curvature flow. For this choice of parameter the evolution under surface diffusion with kinetics is close to that under mean curvature flow when only considering the shape.

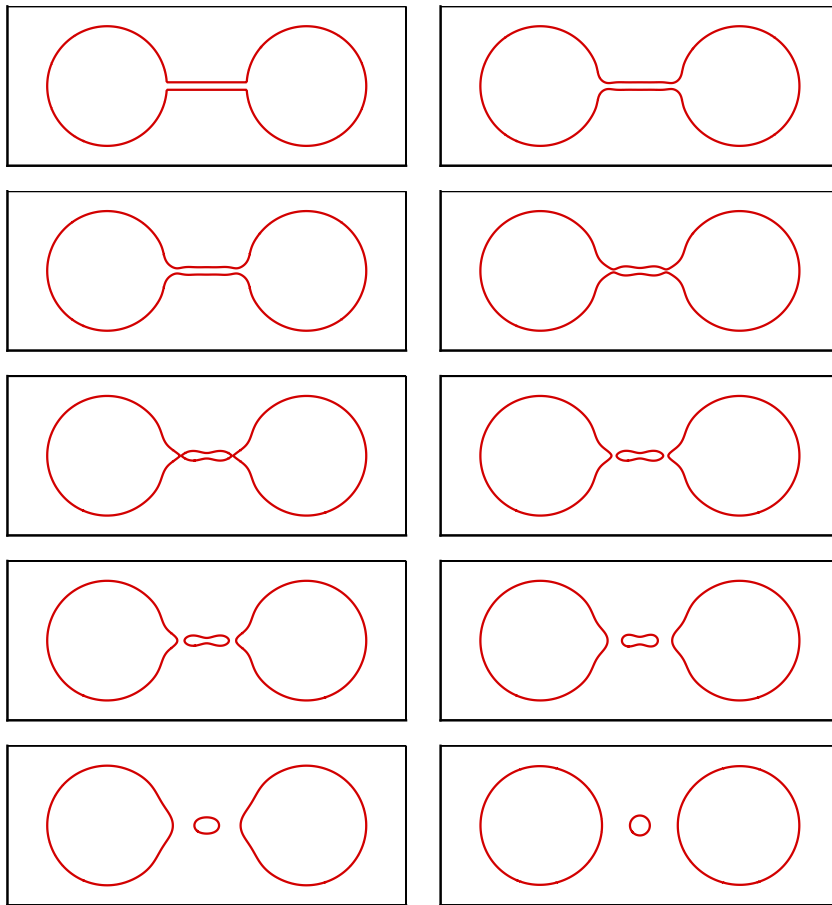


Figure 3.17: Evolution of curve under surface diffusion. $[0, 6] \times [-1.5, 1.5]$ grid, grid size $h = 0.015625$, timestep $\Delta t = 10^{-6}$. From top left to bottom right: $t = 0.0, 5 \times 10^{-6}, 10^{-5}, 3 \times 10^{-5}, 3.6 \times 10^{-5}, 3.8 \times 10^{-5}, 4 \times 10^{-5}, 6 \times 10^{-5}, 0.0001, 0.005$.

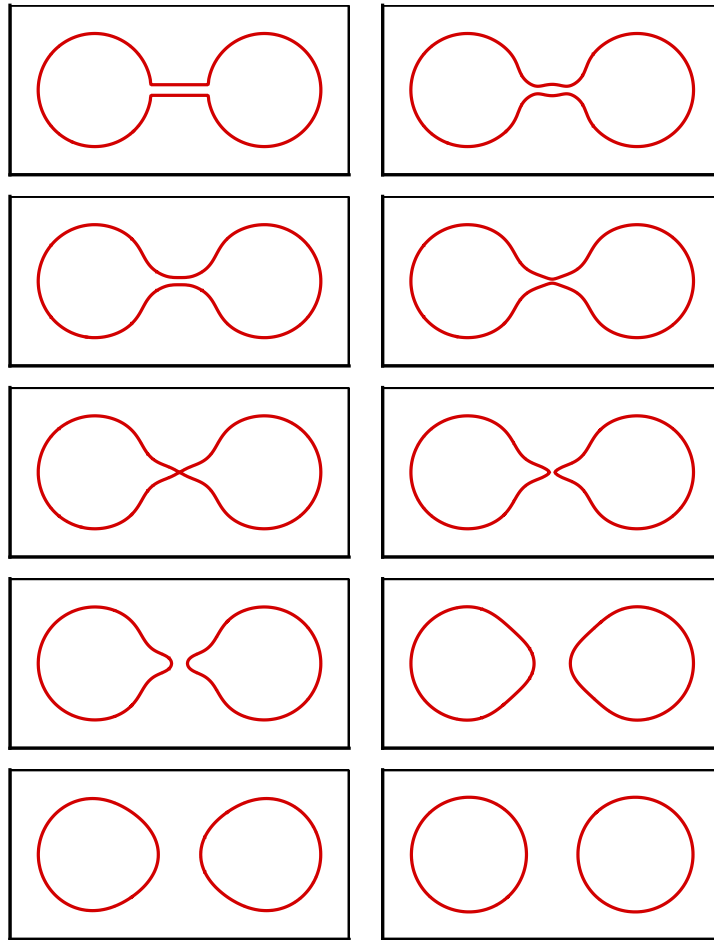


Figure 3.18: Evolution of curve under surface diffusion. $[0, 6] \times [-1.5, 1.5]$ grid, grid size $h = 0.015625$, timestep $\Delta t = 10^{-6}$. From top left to bottom right: $t = 0.0, 10^{-5}, 4 \times 10^{-5}, 5 \times 10^{-5}, 5.3 \times 10^{-5}, 5.4 \times 10^{-5}, 6 \times 10^{-5}, 0.0002, 0.0005, 0.01$.

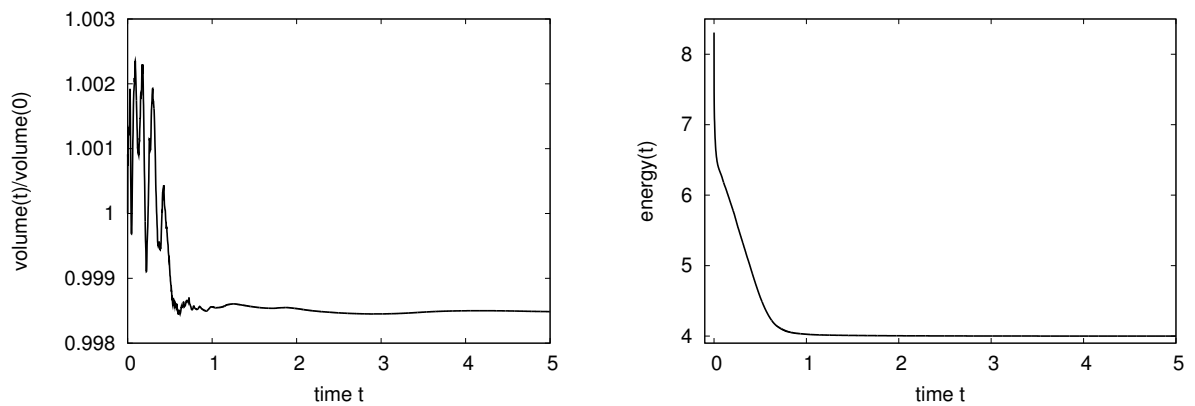


Figure 3.19: Change of volume (left) and energy dissipation (right) in evolution under isotropic surface diffusion for the example in figure 3.16.

Validation of computational results. We check our computational results by a comparison with the limiting cases mean curvature flow and surface diffusion. As already mentioned, the kinetic model is the model of mean curvature flow for the parameter choice $m = 0$, $b = 0$. We now choose the parameters m and b in the kinetic model small and show that the results are close to those achieved by computations with mean curvature flow. We start with a star-like closed curve. The comparison of the results is given in figure 3.20. With the exception of the last timestep, where minor differences can be observed, the results are undistinguishable, which confirms the correctness of our computations in the limiting case.

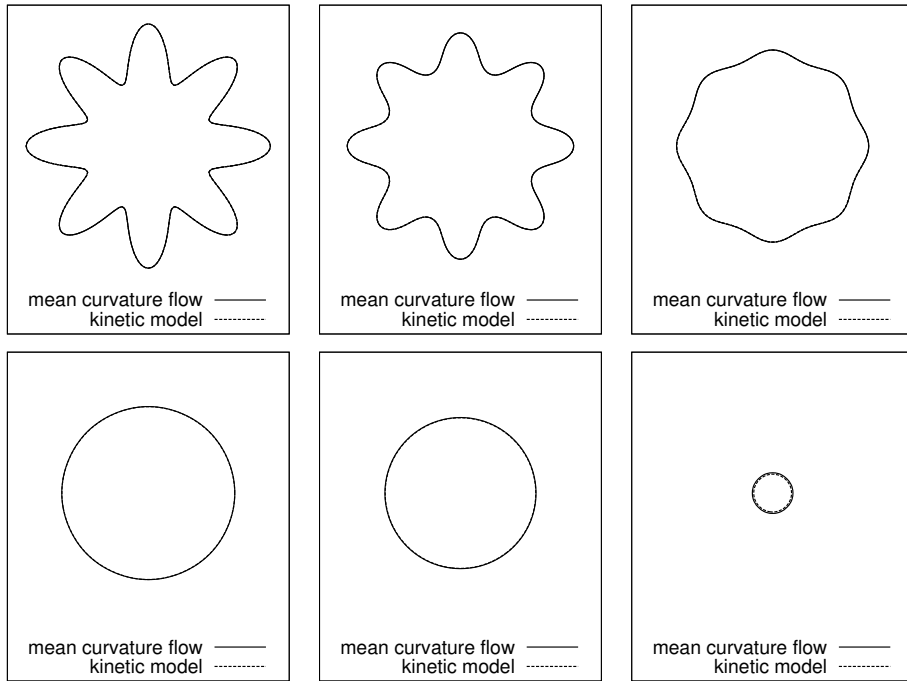


Figure 3.20: Comparison of mean curvature flow and kinetic model with $b = 0.0001$, $c = 1.0$ and $m = 0.0001$. $[0, 4] \times [0, 4]$ grid, grid size $h = 0.03125$, timestep $\Delta t = 0.001$. From top left to bottom right: $t = 0.0, 0.01, 0.04, 0.1, 0.2, 0.5$.

The model of surface diffusion is a special case of the kinetic model for parameters $b = 0$ and $c = 0$. Again, we use a star-like shape to test the evolution. Figure 3.21 shows that the evolution of the closed curve under the kinetic model with small parameters b and c converges to the evolution under surface diffusion.

Comparison of surface diffusion with surface diffusion with kinetics. We compare the evolution of an overlaid sine function under surface diffusion and surface diffusion with kinetics in figure 3.22. With respect to the shape, the evolution in both models seems to coincide. But the evolution under surface diffusion with kinetics is much slower. In this example, surface diffusion is about twenty times faster than surface diffusion with kinetics.

Different choices of parameters. Following the supposition in [33], we study the influence of the parameter b for small values. The different parameter values are $b = 1$, $b = 0.1$, $b = 0.01$ and $b = 0.001$. Figure 3.23 shows a comparison of surface diffusion with kinetics and surface diffusion. For $b = 1$ and $b = 0.1$ a significant slow-down in the evolution can be observed due to the kinetic term bV . Even for $b = 0.01$ a difference in the evolution velocity is clearly visible. But for very small values as $b \leq 0.001$ the kinetic term seems to be negligible.

We have already stated that evolution under the kinetic model is volume conserving for $c = 0$. A change of volume can be expected for non-zero values of c . Figure 3.24 shows that the shape

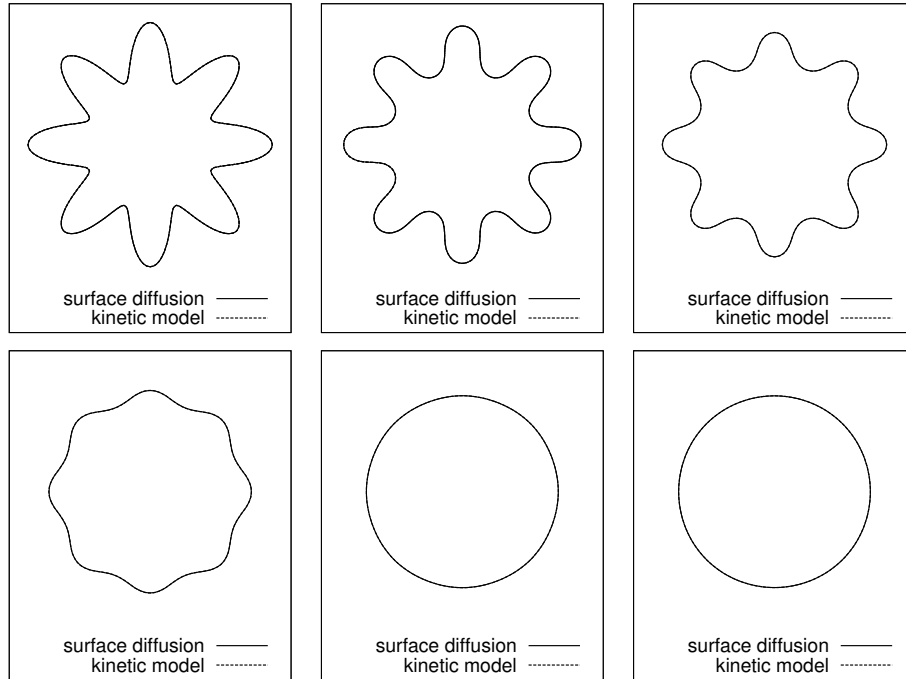


Figure 3.21: Comparison of surface diffusion and kinetic model with $b = 0.0001$, $c = 0.0001$ and $m = 1.0$. $[0, 4] \times [0, 4]$ grid, grid size $h = 0.03125$, timestep $\Delta t = 10^{-6}$. From top left to bottom right: $t = 0.0, 0.0001, 0.0005, 0.001, 0.002, 0.003$.

of the evolving curve is the same for the kinetic model with $c = 1$ and surface diffusion with kinetics at each time instance for our choice of parameters. The only difference is a difference in volume. As expected the volume of the domain enclosed by the curve shrinks for $c = 1$.

As stated before, the limiting case for $m \rightarrow \infty$ in the kinetic model with $c = 0$ is the volume-conserving mean curvature flow. It is the question whether m has to be chosen very large to reveal this effect. Figure 3.25 shows that already for the value $m = 1$ the evolution seems to be that of volume-conserving mean curvature flow. The results for $m = 1$ and $m = 100$ are undistinguishable.

Comparison to surface diffusion and mean curvature flow. We finally present comparisons of the three models of surface diffusion, surface diffusion with kinetics and mean curvature flow. In figure 3.26 a 2D example is given. The comparison confirms our observations. The evolution under surface diffusion is much faster than that under surface diffusion with kinetics and mean curvature flow. And with respect to the evolution velocity of the shape the evolution under surface diffusion with kinetics with parameter $m = 1$ is close to that of mean curvature flow. Here, the only difference is the enclosed volume.

Figure 3.27 presents a comparison of the three models in a 3D example. The figure shows that our observations also seem to be valid for the evolution of surfaces. Especially, the change from a convex to a non-convex shape does only occur for surface diffusion.

Volume conservation. In all numerical examples for the volume-conserving evolution of surface diffusion with kinetics the change in volume measures at most 0.6%.

We note, that the parameter study is far from complete and our choice of parameter somehow arbitrary. An analysis with realistic parameters in the physical context would be interesting.

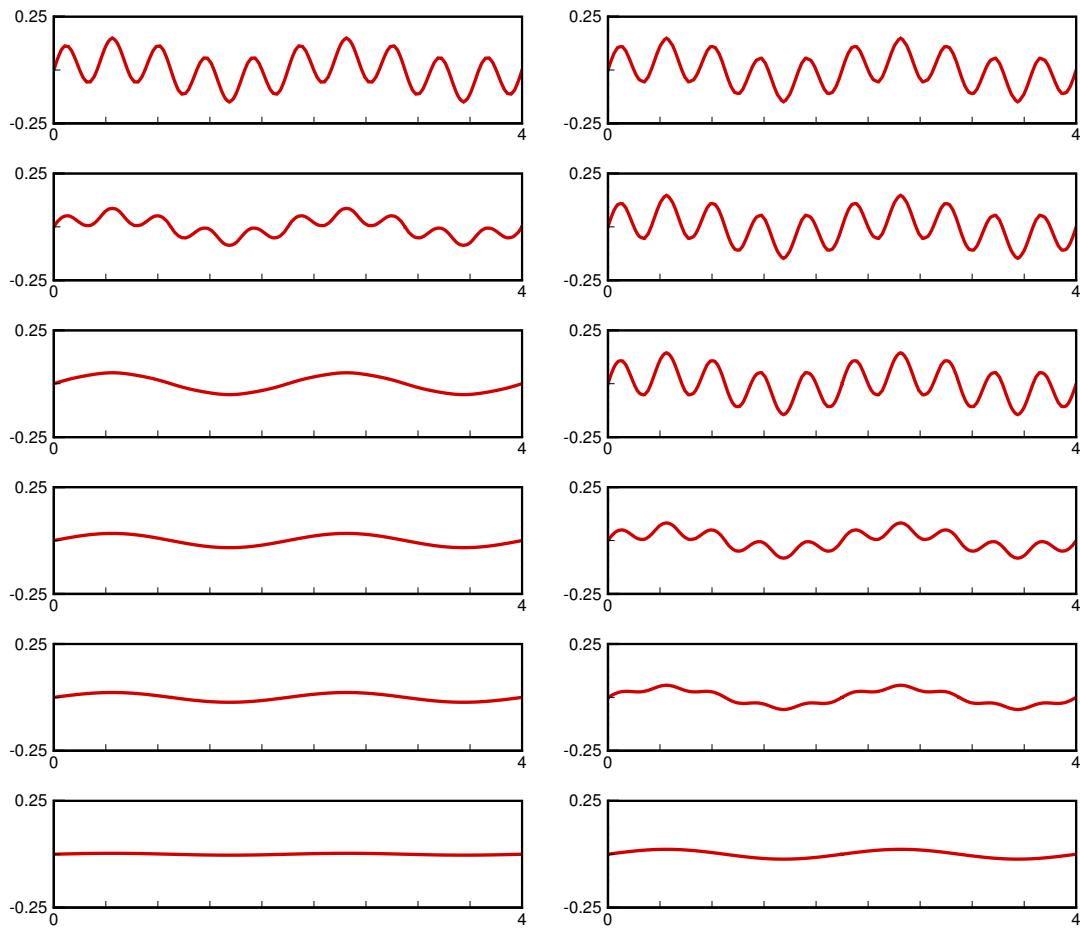


Figure 3.22: Comparison of evolution under surface diffusion (left) and surface diffusion with kinetics with $b = 1.0$, $m = 1.0$ (right). $[0.4] \times [-1, 1]$ grid, grid size $h = 0.03125$, timestep $\Delta t = 10^{-6}$. From top to bottom: $t = 0.0, 0.00003, 0.0001, 0.005, 0.01, 0.1$.

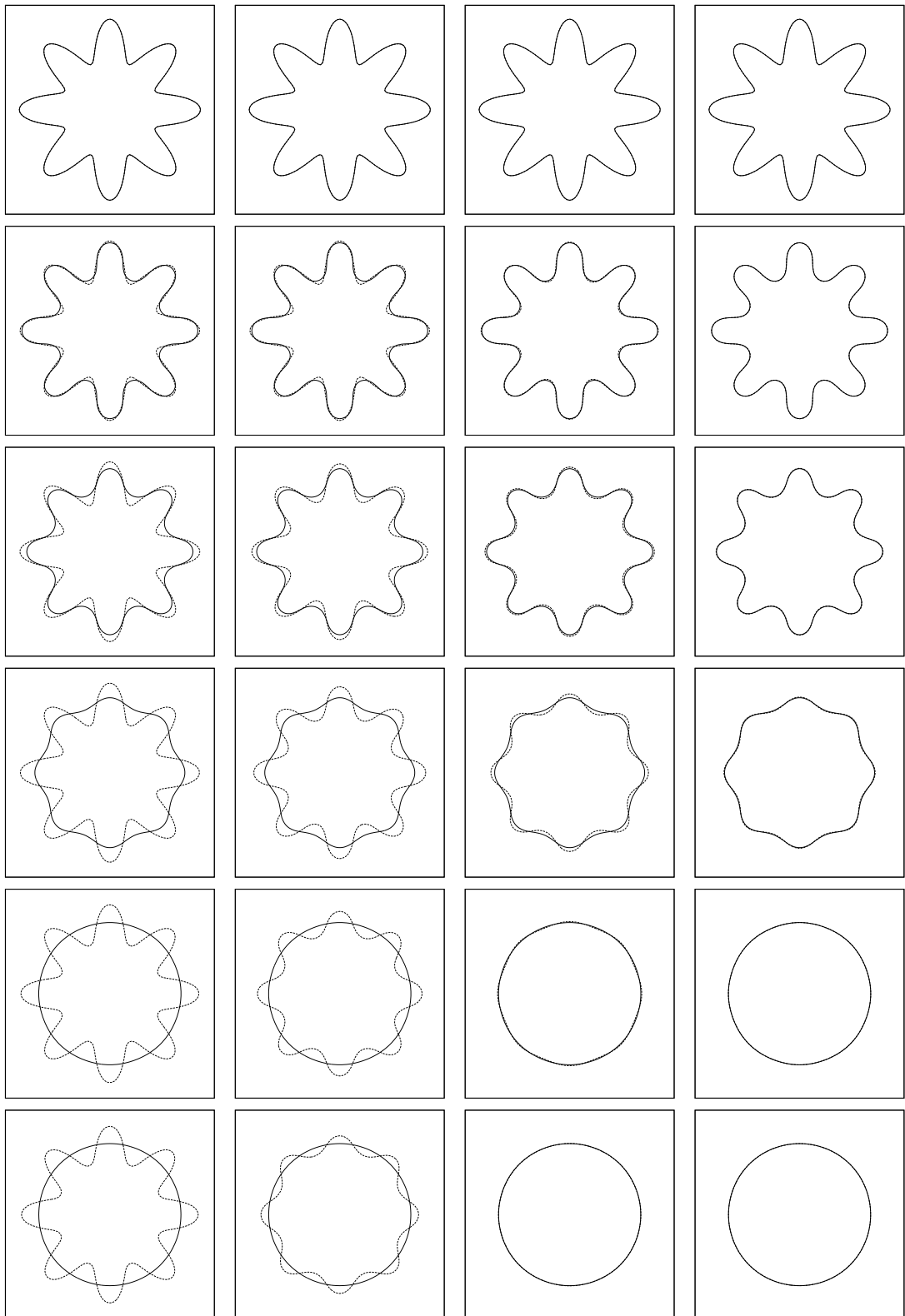


Figure 3.23: Comparison of surface diffusion (solid line) and surface diffusion with kinetics with $c = 0.0$, $m = 1.0$ and different values for b (dashed line). First column: $b = 1.0$, second column: 0.1 , third column: $b = 0.01$, fourth column: $b = 0.001$. $[0, 4] \times [0, 4]$ grid, grid size $h = 0.03125$, timestep $\Delta t = 10^{-6}$. From top to bottom: $t = 0.0, 0.0001, 0.0005, 0.001, 0.002, 0.003$.

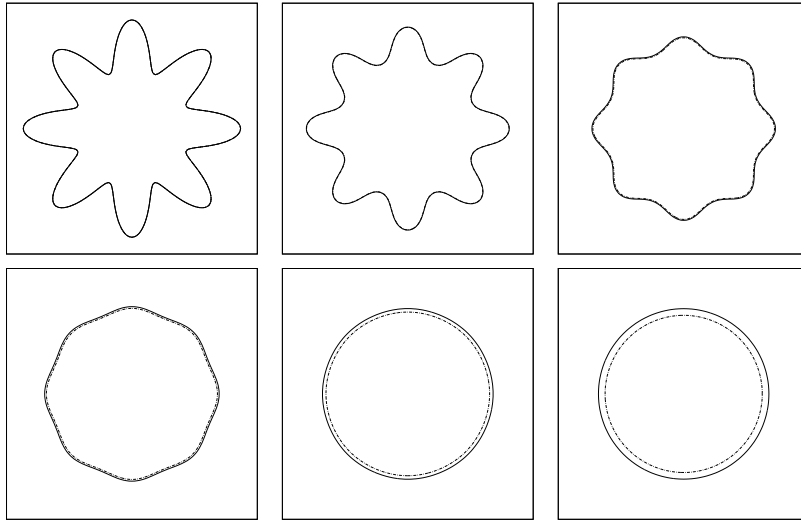


Figure 3.24: Comparison of surface diffusion with kinetics with $b = 1.0$, $m = 1.0$ (solid line) and kinetic model with $b = 1.0$, $c = 1.0$, $m = 1.0$ (dash-dotted line). $[0, 4] \times [0, 4]$ grid, grid size $h = 0.03125$, timestep $\Delta t = 10^{-6}$. From top left to bottom right: $t = 0.0, 0.01, 0.03, 0.05, 0.1, 0.18$.

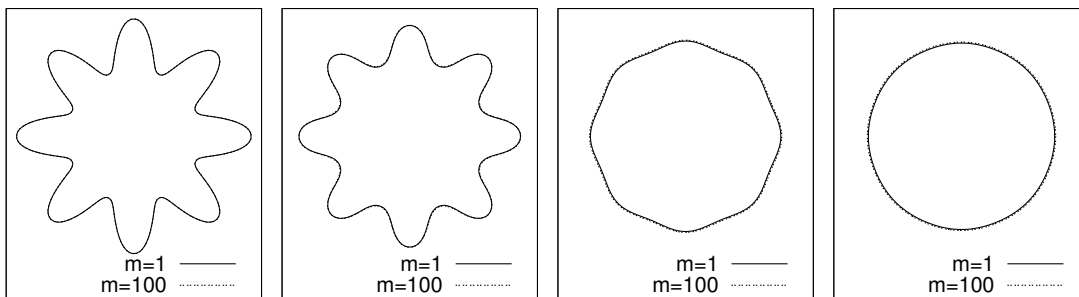


Figure 3.25: Comparison of surface diffusion with kinetics with $b = 1.0$ and different values for m : $m = 1$ (solid line) and $m = 100$ (dashed line). $[0, 4] \times [0, 4]$ grid, grid size $h = 0.03125$, timestep $\Delta t = 10^{-6}$ ($m = 1$) and $\Delta t = 10^{-5}$ ($m = 100$). From left to right: $t = 0.001, 0.01, 0.05, 0.09$.

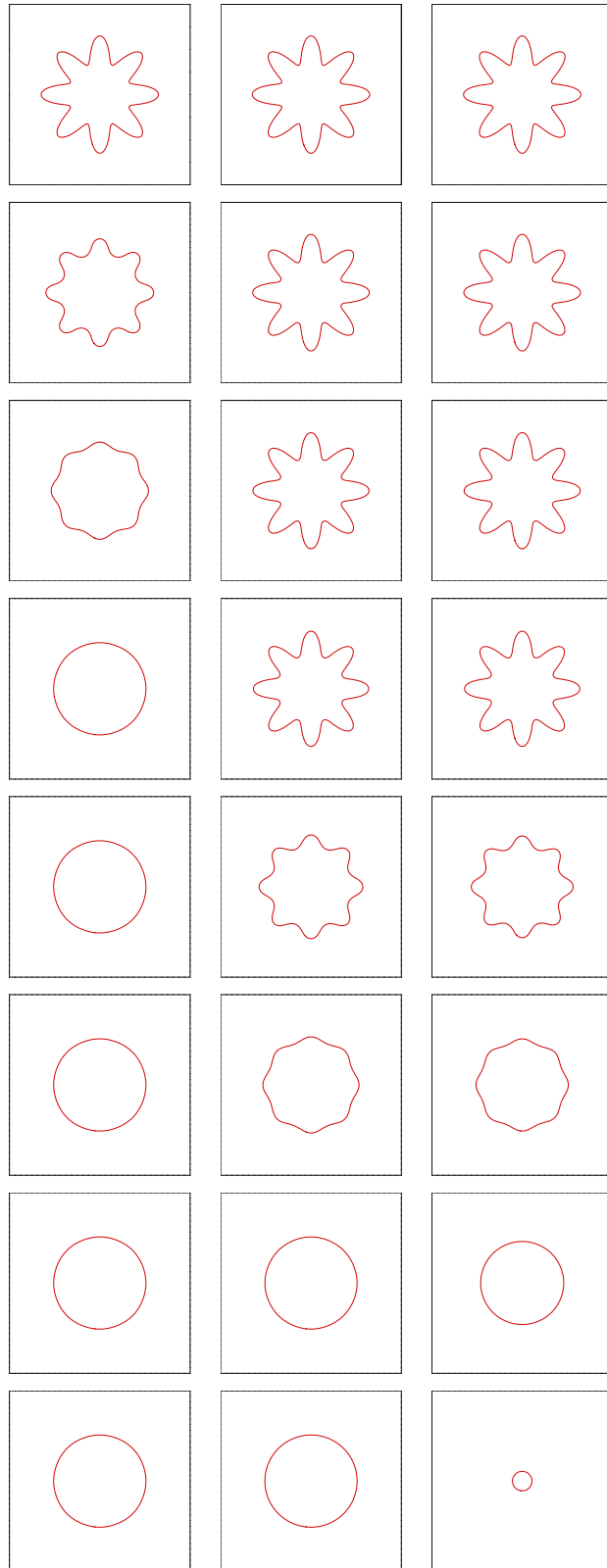


Figure 3.26: Comparison of surface diffusion (left), surface diffusion with kinetics with $c = 0.0$, $m = 1.0$ and $b = 1.0$ (center) and mean curvature flow (right). $[0, 4] \times [0, 4]$ grid, grid size $h = 0.03125$, timestep $\Delta t = 10^{-6}$ (surface diffusion and surface diffusion with kinetics) and $\Delta t = 10^{-5}$ (mean curvature flow). From top to bottom: $t = 0.0, 0.0005, 0.001, 0.002, 0.02, 0.04, 0.1, 0.5$.

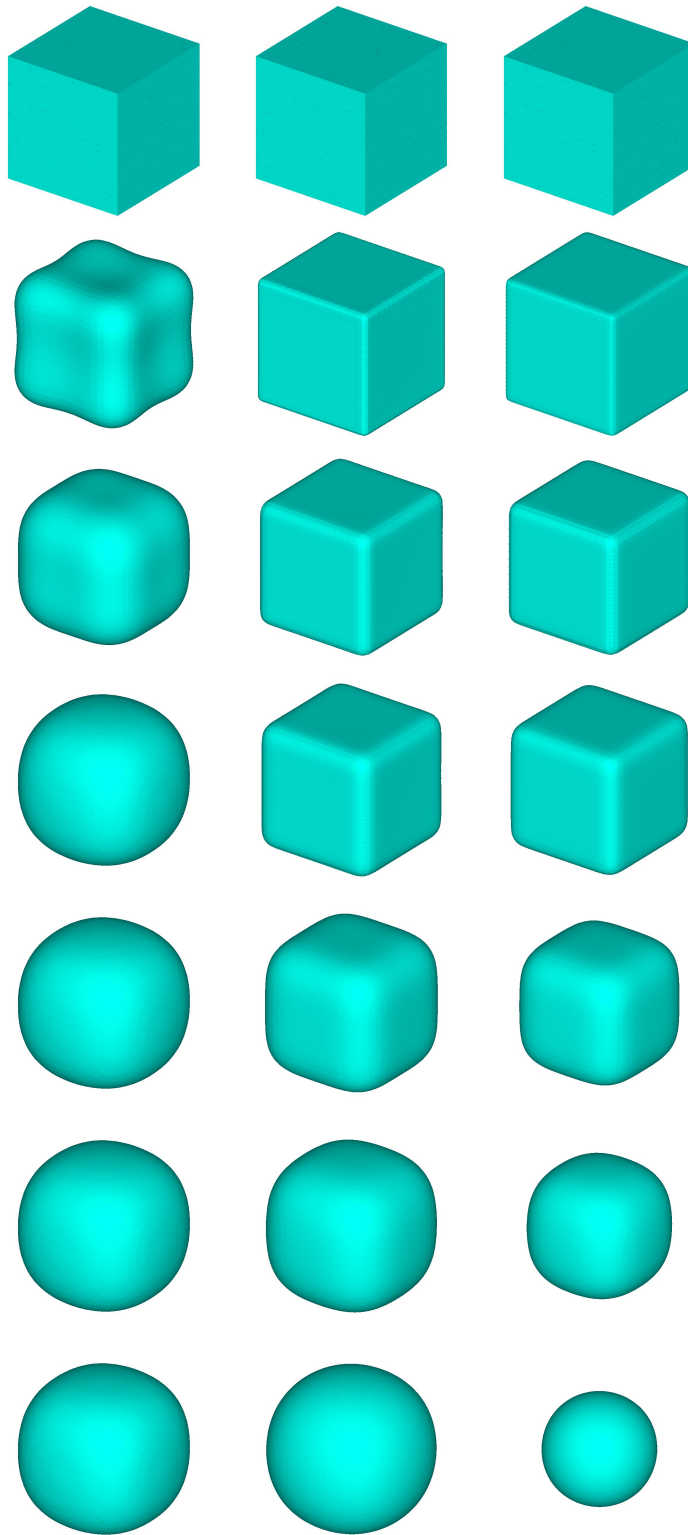


Figure 3.27: Comparison of evolution under surface diffusion (left), surface diffusion with kinetics with $c = 0.0$, $m = 1.0$ and $b = 1.0$ (center) and mean curvature flow (right). $[0, 4] \times [0, 4] \times [0, 4]$ grid, grid size $h = 0.05$, timestep $\Delta t = 10^{-6}$ (surface diffusion), $\Delta t = 0.0001$ (surface diffusion with kinetics) and $\Delta t = 0.001$ (mean curvature flow). From top to bottom: $t = 0.0, 0.001, 0.005, 0.01, 0.05, 0.1, 0.2$.

Chapter 4

Anisotropic evolution laws

In thin film growth, materials are often anisotropic, i.e. the motion velocity depends on the motion direction. So the isotropic models discussed so far are too simple. We now consider evolution laws where the normal velocity depends on the motion direction. In physical context, this means that certain directions are energetically more favorable than others. The anisotropic behavior is expressed by an anisotropy function γ depending on the surface normal. Again, our evolution laws are energy decreasing. The energy functional now accounts for the anisotropic behavior. It is given through

$$E[\Gamma] = \int_{\Gamma} \gamma \, dA. \quad (4.1)$$

In this chapter, the evolution laws treated in chapter 3 are presented in their anisotropic counterpart. First, we give a precise definition of anisotropy functions and explain their relation to energy minimizing shapes of evolving surfaces. Then, we come to the anisotropic formulation of the evolution equations and their numerical treatment.

4.1 Anisotropy

An anisotropy function is a positive one-homogeneous differentiable function $\gamma : \mathbb{R}^{d+1} \setminus \{0\} \rightarrow \mathbb{R}$, that means we have

$$\gamma(\lambda x) = \lambda \gamma(x) \quad \text{for all } \lambda > 0.$$

The first derivative $D\gamma$ is zero-homogeneous

$$D\gamma(\lambda x) = D\gamma(x) \quad \text{for all } \lambda > 0,$$

which is a consequence of the one-homogeneity of γ . Anisotropy functions are also often defined as one-homogeneous extensions of functions given on the unit sphere S^d .

In this chapter, we concentrate on anisotropy functions which are convex. This guarantees the well-posedness of the parabolic equations we consider. In chapter 5 we explain the relation between the convexity of the anisotropy function and the well-posedness of the problem in more detail.

In \mathbb{R}^2 the surface normal is uniquely determined through the angle θ between the normal and a fixed coordinate axis, e.g. the x-axis of the Cartesian coordinate system. Thus, the anisotropy function can also be defined in terms of the angle θ . Doing so, the convexity of an anisotropy function can be decided by looking at the polar plot of the inverse function. γ is convex if and only if $1/\gamma$ is convex. A computational argument for convexity in 2D uses the stiffness $\tilde{\gamma}(\theta) = \gamma(\theta) + \gamma''(\theta)$. The anisotropy γ is convex if and only if the stiffness is non-negative. See [51] for more details on anisotropy functions and their representation.

In isotropic situation the energy minimizing shape for closed surfaces is the sphere, or circle in 2D. This is the shape with the smallest area with respect to the enclosed volume. Starting with an arbitrary closed surface, evolution tends towards a sphere. In anisotropic situation the energy functional can be interpreted as weighted area functional. The energy minimizing shape \mathcal{W}_γ , the so called wulffshape, is defined through

$$\mathcal{W}_\gamma = \{x \in \mathbb{R}^{d+1} \mid x \cdot \nu \leq \gamma(\nu) \text{ for all } \nu \in S^d\}.$$

This is the shape with the minimal (anisotropic) energy with respect to the enclosed volume. The boundary of the wulffshape can be calculated as the image of the sphere under the first derivative of the anisotropy function, $\mathcal{W}_\gamma = D\gamma(S^d)$, see [51] and [20]. The notion wulffshape goes back to Wulff who solved in [72] the problem of determining the equilibrium shape of a perfect crystal.

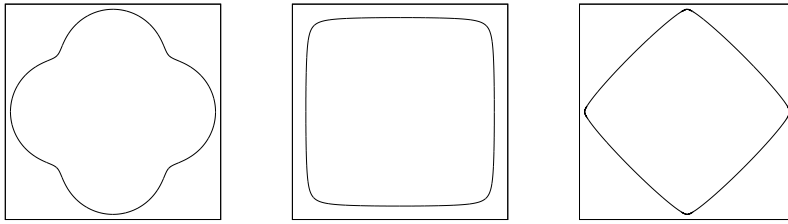


Figure 4.1: Polar plot of anisotropy function, its inverse and the corresponding wulffshape for the anisotropy defined in 4.2.

In our numerical examples we use the anisotropy function

$$\gamma(p) = \gamma_0(R_{\pi/4}(p)) \quad \text{with} \quad \gamma_0(p) = \sum_{i=1}^d (a|p|^2 + p_i^2)^{1/2}, \quad a = 0.01 \quad (4.2)$$

and $R_{\pi/4}$ the clockwise rotation about the angle $\pi/4$ in \mathbb{R}^{d+1} . In figure 4.1 the polar plot of γ and $1/\gamma$ and the wulffshape of γ are given. The convexity of the polar plot of $1/\gamma$ illustrates the convexity of the anisotropy function.

In anisotropic evolution, the motion behavior of surfaces now also depends on the motion direction. Whereas the evolution in isotropic situation is basically determined through the mean curvature of the surface in the models discussed so far, it is now determined through the weighted or anisotropic mean curvature, which depends on the anisotropy function. It is defined through

$$H_\gamma = \nabla \cdot D\gamma(\nu),$$

which in terms of a level set function ϕ and due to the zero-homogeneity of $D\gamma$ gives with (2.13)

$$H_\gamma = \nabla \cdot D\gamma(\nabla\phi). \quad (4.3)$$

For curves the weighted mean curvature is defined through

$$H_\gamma = (\gamma + \gamma'')H.$$

The weighted mean curvature is the variational derivative of the weighted energy functional (4.1) with respect to variations in normal direction

$$\frac{\delta E}{\delta \Gamma} = H_\gamma, \quad (4.4)$$

see e.g. [23].

4.2 Anisotropic mean curvature flow

Corresponding to the evolution law of isotropic mean curvature flow in its variational formulation, $V = -\frac{\delta E}{\delta \Gamma}$, the evolution law of anisotropic mean curvature flow with the energy (4.1) reads

$$V = -cH_\gamma \quad (4.5)$$

with the positive coefficient c . The evolution under anisotropic mean curvature flow has been numerically analyzed in several works by Deckelnick, Dziuk and Elliott. In [22] the authors provide stability and error analysis in the graph case, as well as a semi-implicit discretization scheme, which is unconditionally stable.

We obtain the level set formulation with 2.12 and 4.3 by

$$\frac{1}{c} \frac{\phi_t}{|\nabla \phi|} = \nabla \cdot D\gamma(\nabla \phi).$$

To derive the finite element discretization, we start with the weak formulation of this equation, which is

$$\int_{\Omega} \frac{1}{c} \frac{\phi_t}{|\nabla \phi|} \eta \, dx = - \int_{\Omega} D\gamma(\nabla \phi) \cdot \nabla \eta \, dx \quad (4.6)$$

for all test functions $\eta \in C_0^\infty(\Omega)$. In the evolution of curves in 2D the evolution law reads $V = -c(\gamma + \gamma'')H$. Thus in the strong formulation of the evolution law, the second derivative of the anisotropy function γ is needed. Solving the evolution equation with finite differences thus also requires the second derivative of γ . Whereas in the weak formulation only the first derivative of γ occurs, and for this reason, the finite element solution only needs $\gamma \in C^1(\mathbb{R}^{d+1} \setminus \{0\})$. Our semi-implicit discretization scheme described in section 3.1 and norm regularization provide

$$\int_{\Omega} \frac{1}{c} \frac{\phi^{k+1}}{|\nabla \phi^k|_\delta} \eta \, dx - \int_{\Omega} \frac{1}{c} \frac{\phi^k}{|\nabla \phi^k|_\delta} \eta \, dx + \tau \int_{\Omega} D\gamma(\nabla \phi^k) \cdot \nabla \eta \, dx = 0$$

for all $\eta \in \mathcal{V}^h$. In the above discretization, the anisotropic mean curvature term is treated fully explicit. To treat this term more implicitly and for stabilization reasons, the authors in [22] introduced a semi-implicit discretization scheme for this term, which we will apply throughout this work. It extends the integral term $\int_{\Omega} D\gamma(\nabla \phi^k) \cdot \nabla \eta \, dx$ to

$$\int_{\Omega} D\gamma(\nabla \phi^k) \cdot \nabla \eta \, dx + \lambda \int_{\Omega} \frac{\gamma\left(\frac{\nabla \phi^k}{|\nabla \phi^k|_\delta}\right)}{|\nabla \phi^k|_\delta} \nabla(\phi^{k+1} - \phi^k) \cdot \nabla \eta \, dx. \quad (4.7)$$

In isotropic situation, where $D\gamma(p) = p/|p|$ and $\gamma(p) = |p|$, it simplifies for $\lambda = 1$ to the full implicit discretization of the mean curvature term

$$\int_{\Omega} \frac{\nabla \phi^{k+1}}{|\nabla \phi^k|_\delta} \cdot \nabla \eta \, dx$$

which we used for isotropic mean curvature flow, compare with our discretized equations in (3.2). The authors in [22] proofed for the numerical solution of anisotropic mean curvature flow with the graph formulation, that choosing the positive parameter λ with respect to the first and second derivative of the anisotropy γ sufficiently large, provides an unconditionally stable numerical scheme. Using the semi-implicit discretization scheme (4.7) in our discretization results in

$$\begin{aligned} \int_{\Omega} \frac{\phi^{k+1}}{|\nabla \phi^k|_\delta} \eta \, dx - \int_{\Omega} \frac{\phi^k}{|\nabla \phi^k|_\delta} \eta \, dx + \tau \int_{\Omega} D\gamma(\nabla \phi^k) \cdot \nabla \eta \, dx + \\ \tau \lambda \int_{\Omega} \frac{\gamma\left(\frac{\nabla \phi^k}{|\nabla \phi^k|_\delta}\right)}{|\nabla \phi^k|_\delta} \nabla(\phi^{k+1} - \phi^k) \cdot \nabla \eta \, dx = 0 \end{aligned}$$

for all $\eta \in \mathcal{V}^h$. With the system matrices

$$\begin{aligned} M_1 &:= M\left[\frac{1}{c}|\nabla\phi^k|_\delta^{-1}\right], \\ L_1 &:= L\left[|\nabla\phi^k|_\delta^{-1}\gamma\left(\frac{\nabla\phi^k}{|\nabla\phi^k|_\delta}\right)\right], \\ R_1 &:= \left(\int_\Omega D\gamma(\nabla\phi^k) \cdot \nabla\varphi_i\right)_i \end{aligned}$$

and the linear expansion

$$\phi^k = \sum_{i=1}^N \bar{\phi}_i^k \varphi_i$$

the linear system to be solved in timestep $k+1$ reads

$$\left(M_1 + \tau\lambda L_1\right)\bar{\phi}^{k+1} = M_1\bar{\phi}^k + \tau\lambda L_1\bar{\phi}^k - \tau R_1.$$

We solve the symmetric and positive definite system with the conjugate gradient method.

4.3 Anisotropic surface diffusion

With (3.4), the evolution law of isotropic surface diffusion can be written as $V = \nabla_\Gamma \cdot (m\nabla_\Gamma \frac{\delta E}{\delta \Gamma})$, where here E is the isotropic energy functional (3.3). Again, we obtain the anisotropic evolution law by using the anisotropic energy functional (4.1) and its variational derivative (4.4) instead, which gives

$$V = \nabla_\Gamma \cdot (m\nabla_\Gamma H_\gamma)$$

with the non-negative diffusion coefficient m . In [24] a numerical solution of the equation with the graph formulation is presented, and stability and error analysis is given for the numerical scheme. In [21] a numerical solution with the level set method is given. The level set treatment, which we derive in the following, is taken from this work.

With 2.12 and 4.3 we get the fourth order evolution equation

$$-\phi_t = \nabla \cdot \left(m|\nabla\phi|P_\Gamma \nabla(\nabla \cdot D\gamma(\nabla\phi))\right)$$

which we split again in two second order equations through

$$\begin{aligned} -\phi_t &= \nabla \cdot \left(m|\nabla\phi|P_\Gamma \nabla\omega\right) \\ \omega &= \nabla \cdot D\gamma(\nabla\phi). \end{aligned}$$

The weak formulation reads

$$\int_\Omega \phi_t \eta \, dx = \int_\Omega m|\nabla\phi|P_\Gamma \nabla\omega \cdot \nabla\eta \, dx \quad (4.8)$$

$$\int_\Omega \omega \xi \, dx = - \int_\Omega D\gamma(\nabla\phi) \cdot \nabla\xi \, dx \quad (4.9)$$

for all test functions $\eta, \xi \in C_0^\infty(\Omega)$ and contains now only derivatives of highest order one, which can be discretized by linear finite elements. Space and time discretization and norm regularization provide

$$\begin{aligned} \int_\Omega \phi^{k+1} \eta \, dx - \int_\Omega \phi^k \eta \, dx - \tau \int_\Omega m|\nabla\phi^k|_\delta P_\Gamma^k \nabla\omega^{k+1} \cdot \nabla\eta \, dx &= 0 \\ \int_\Omega \omega^{k+1} \xi \, dx + \int_\Omega D\gamma(\nabla\phi^k) \cdot \nabla\xi \, dx &= 0 \end{aligned}$$

for all $\eta, \xi \in \mathcal{V}^h$. Again, we make use of the semi-implicit discretization scheme (4.7) for the anisotropic mean curvature term and finally obtain the discretization

$$\int_{\Omega} \phi^{k+1} \eta \, dx - \int_{\Omega} \phi^k \eta \, dx - \tau \int_{\Omega} m |\nabla \phi^k|_{\delta} P_{\Gamma}^k \nabla \omega^{k+1} \cdot \nabla \eta \, dx = 0 \quad (4.10)$$

$$\int_{\Omega} \omega^{k+1} \xi \, dx + \int_{\Omega} D\gamma(\nabla \phi^k) \cdot \nabla \xi \, dx + \lambda \int_{\Omega} \frac{\gamma(\frac{\nabla \phi^k}{|\nabla \phi^k|_{\delta}})}{|\nabla \phi^k|_{\delta}} \nabla(\phi^{k+1} - \phi^k) \cdot \nabla \xi \, dx = 0 \quad (4.11)$$

for all $\eta, \xi \in \mathcal{V}^h$. With the system matrices

$$\begin{aligned} M_1 &:= M[1], \\ L_1 &:= L[m|\nabla \phi^k|_{\delta} P_{\Gamma}^k], \\ L_2 &:= L[|\nabla \phi^k|_{\delta}^{-1} \gamma(\frac{\nabla \phi^k}{|\nabla \phi^k|_{\delta}})], \\ R_1 &:= \left(\int_{\Omega} D\gamma(\nabla \phi^k) \cdot \nabla \varphi_i \right)_i \end{aligned}$$

and the linear expansions

$$\phi^k = \sum_{i=1}^N \bar{\phi}_i^k \varphi_i, \quad \omega^k = \sum_{i=1}^N \bar{\omega}_i^k \varphi_i$$

the linear system to be solved in timestep $k+1$ reads

$$\begin{pmatrix} M_1 & -\tau L_1 \\ \lambda L_2 & M_1 \end{pmatrix} \begin{pmatrix} \bar{\phi}^{k+1} \\ \bar{\omega}^{k+1} \end{pmatrix} = \begin{pmatrix} M_1 \bar{\phi}^k \\ \lambda L_2 \bar{\phi}^k - R_1 \end{pmatrix}.$$

As in isotropic situation, we solve the linear system with a Schur complement approach, which provides the equation

$$\left(M_1 + \tau \lambda L_1 M_1^{-1} L_2 \right) \bar{\phi}^{k+1} = M_1 \bar{\phi}^k + \tau L_1 M_1^{-1} (\lambda L_2 \bar{\phi}^k - R_1)$$

for the unknown level set function ϕ^{k+1} . We approximate the inverse M_1^{-1} with mass lumping. The non-symmetric system is solved with the Krylov subspace method BiCGStab2.

4.4 Anisotropic kinetic model

In equations (3.9) and (3.10) the evolution law of the kinetic model is presented in a general form for an arbitrary energy functional $E[\Gamma]$. We use this representation with the anisotropic energy functional (4.1) and its variational derivative (4.4) and obtain the evolution law of the kinetic model in its anisotropic version

$$\begin{aligned} V &= \nabla_{\Gamma} \cdot (m \nabla_{\Gamma} \mu) - c \mu \\ bV &= -H_{\gamma} + \mu. \end{aligned}$$

The transformation to the level set formulation gives

$$\begin{aligned} \phi_t &= -\nabla \cdot (m |\nabla \phi| P_{\Gamma} \nabla \mu) + c |\nabla \phi| \mu \\ b \frac{\phi_t}{|\nabla \phi|} &= \nabla \cdot D\gamma(\nabla \phi) - \mu, \end{aligned}$$

and the weak formulation reads

$$\begin{aligned} \int_{\Omega} \phi_t \eta \, dx &= \int_{\Omega} m |\nabla \phi| P_{\Gamma} \nabla \mu \cdot \nabla \eta \, dx + \int_{\Omega} c |\nabla \phi| \mu \eta \, dx \\ \int_{\Omega} b \frac{\phi_t}{|\nabla \phi|} \xi \, dx &= - \int_{\Omega} D\gamma(\nabla \phi) \cdot \nabla \xi \, dx - \int_{\Omega} \mu \xi \, dx \end{aligned}$$

for all test functions $\eta, \xi \in C_0^\infty(\Omega)$. Our semi-implicit discretization scheme and norm regularization provide

$$\begin{aligned} \int_{\Omega} \phi^{k+1} \eta \, dx - \int_{\Omega} \phi^k \eta \, dx - \tau \int_{\Omega} m |\nabla \phi^k|_{\delta} P_{\Gamma}^k \nabla \mu^{k+1} \cdot \nabla \eta \, dx - \tau \int_{\Omega} c |\nabla \phi^k|_{\delta} \mu^{k+1} \eta \, dx &= 0 \\ \int_{\Omega} b \frac{\phi^{k+1}}{|\nabla \phi^k|_{\delta}} \xi \, dx - \int_{\Omega} b \frac{\phi^k}{|\nabla \phi^k|_{\delta}} \xi \, dx + \tau \int_{\Omega} D\gamma\left(\frac{\nabla \phi^k}{|\nabla \phi^k|_{\delta}}\right) \cdot \nabla \xi \, dx + \tau \int_{\Omega} \mu^{k+1} \xi \, dx &= 0 \end{aligned}$$

for all $\eta, \xi \in \mathcal{V}^h$, and the semi-implicit treatment of the anisotropic mean curvature term (4.7) results in

$$\begin{aligned} \int_{\Omega} \phi^{k+1} \eta \, dx - \int_{\Omega} \phi^k \eta \, dx - \tau \int_{\Omega} m |\nabla \phi^k|_{\delta} P_{\Gamma}^k \nabla \mu^{k+1} \cdot \nabla \eta \, dx - \tau \int_{\Omega} c |\nabla \phi^k|_{\delta} \mu^{k+1} \eta \, dx &= 0 \\ \int_{\Omega} b \frac{\phi^{k+1}}{|\nabla \phi^k|_{\delta}} \xi \, dx - \int_{\Omega} b \frac{\phi^k}{|\nabla \phi^k|_{\delta}} \xi \, dx + \tau \int_{\Omega} D\gamma\left(\frac{\nabla \phi^k}{|\nabla \phi^k|_{\delta}}\right) \cdot \nabla \xi \, dx + \\ \tau \lambda \int_{\Omega} |\nabla \phi^k|_{\delta}^{-1} \gamma\left(\frac{\nabla \phi^k}{|\nabla \phi^k|_{\delta}}\right) \nabla(\phi^{k+1} - \phi^k) \cdot \nabla \xi \, dx + \tau \int_{\Omega} \mu^{k+1} \xi \, dx &= 0 \end{aligned}$$

for all $\eta, \xi \in \mathcal{V}^h$. With the system matrices

$$\begin{aligned} M_1 &:= M[1], & L_1 &:= L[m |\nabla \phi^k|_{\delta} P_{\Gamma}^k], \\ M_2 &:= M[c |\nabla \phi^k|_{\delta}], & L_2 &:= L[|\nabla \phi^k|_{\delta}^{-1} \gamma\left(\frac{\nabla \phi^k}{|\nabla \phi^k|_{\delta}}\right)], \\ M_3 &:= M[b |\nabla \phi^k|_{\delta}^{-1}], & R_1 &:= \left(\int_{\Omega} D\gamma\left(\frac{\nabla \phi^k}{|\nabla \phi^k|_{\delta}}\right) \cdot \nabla \varphi_i \, dx \right)_i \end{aligned}$$

and the linear expansions

$$\phi^k = \sum_{i=1}^N \bar{\phi}_i^k \varphi_i, \quad \mu^k = \sum_{i=1}^N \bar{\mu}_i^k \varphi_i$$

the linear system to be solved in timestep $k+1$ reads

$$\begin{pmatrix} M_1 & -\tau M_2 - \tau L_1 \\ M_3 + \tau \lambda L_2 & \tau M_1 \end{pmatrix} \begin{pmatrix} \bar{\phi}^{k+1} \\ \bar{\mu}^{k+1} \end{pmatrix} = \begin{pmatrix} M_1 \bar{\phi}^k \\ M_3 \bar{\phi}^k + \tau \lambda L_2 \bar{\phi}^k - \tau R_1 \end{pmatrix}.$$

Again, we apply a Schur complement approach, which gives

$$\left(M_1 + (M_2 + L_1) M_1^{-1} (M_3 + \tau \lambda L_2) \right) \bar{\phi}^{k+1} = M_1 \bar{\phi}^k + (M_2 + L_1) M_1^{-1} (M_3 \bar{\phi}^k + \tau \lambda L_2 \bar{\phi}^k - \tau R_1),$$

and solve the non-symmetric system with the Krylov subspace method BiCGStab2. The inverse M_1^{-1} is approximated with mass lumping.

4.5 Energy dissipation and volume conservation

In the verification of energy dissipation and volume conservation for isotropic mean curvature flow, surface diffusion and evolution under the kinetic model in section 3.1, 3.2 and 3.3 respectively, a general energy $E[\Gamma]$ has been used. Energy dissipation and volume conservation for the evolution laws in their anisotropic version thus follow with the same argumentation applied to the energy functional (4.1) and its variational derivative (4.4).

4.6 Numerical results

In all numerical examples, the anisotropy function defined in (4.2) is used. In difference to the isotropic situation, where a spherical shape is the energetically most favorable shape, the wulffshape is now similar to a square. A plot of the wulffshape for the chosen anisotropy function in 2D is presented in figure 4.1.

For the evolution under anisotropic mean curvature flow and anisotropic surface diffusion, we set again $c = 1$ and $m = 1$ for the coefficients of the models. The parameter choice in the anisotropic kinetic model will be given later.

4.6.1 Mean curvature flow

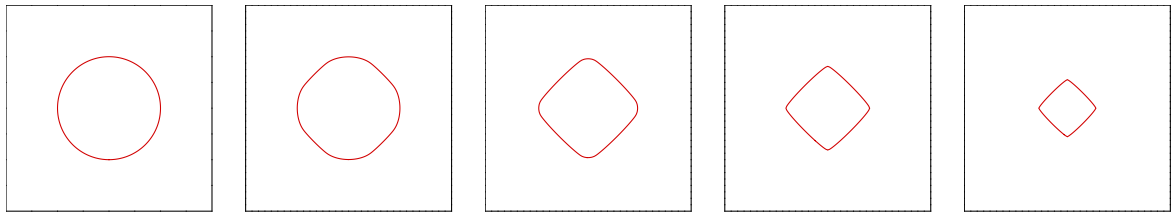


Figure 4.2: Evolution of curve under anisotropic mean curvature flow. $[0, 4] \times [0, 4]$ grid, grid size $h = 0.03125$, timestep $\Delta t = 0.001$, $\lambda = 10.0$. From left to right: $t = 0.0, 0.02, 0.1, 0.2, 0.3$.

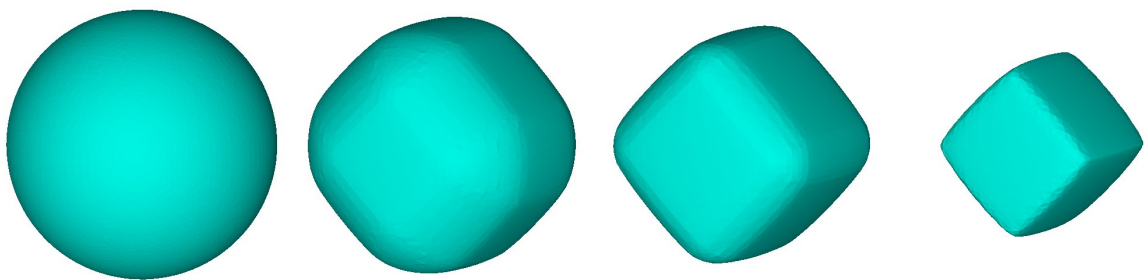


Figure 4.3: Evolution of surface under anisotropic mean curvature flow. $[0, 4] \times [0, 4] \times [0, 4]$ grid, grid size $h = 0.05$, timestep $\Delta t = 0.001$, $\lambda = 5.0$. From left to right: $t = 0.0, 0.02, 0.05, 0.1$.

Closed curves and surfaces. In figure 4.2 the evolution of a circle towards the wulffshape under anisotropic mean curvature flow is given. Let us comment on the way the initial shape changes towards the wulffshape. The weighted mean curvature on the wulffshape is constant. In 2D situation, the weighted mean curvature is given through $\tilde{\gamma}H$. That means for orientations with small mean curvature on the wulffshape, the stiffness $\tilde{\gamma}$ is large, and for orientations with high mean curvature on the wulffshape, the stiffness is comparably small. For this reason, the local formation of the energy minimizing shape is faster for orientations with large stiffness than

for those with small stiffness. This behavior can be observed quite well in the example of the circle. The orientations with high curvature in the wulffshape, develop slower than the others.

Figure 4.3 shows the corresponding example in 3D. A sphere develops under anisotropic mean curvature flow towards the wulffshape. Since mean curvature flow is not volume conserving, the closed surface shrinks after the wulffshape has been reached.

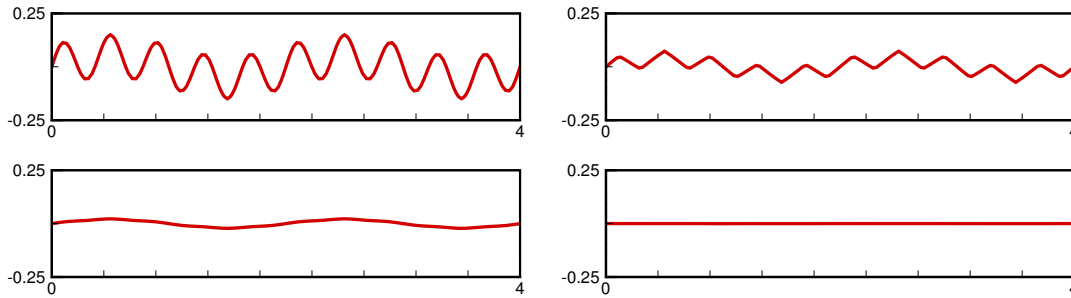


Figure 4.4: Evolution of curve under anisotropic mean curvature flow. $[0, 4] \times [-1, 1]$ grid, grid size $h = 0.03125$, timestep $\Delta t = 0.001$, $\lambda = 10.0$. From top left to bottom right: $t = 0.0, 0.1, 1.0, 10.0$.

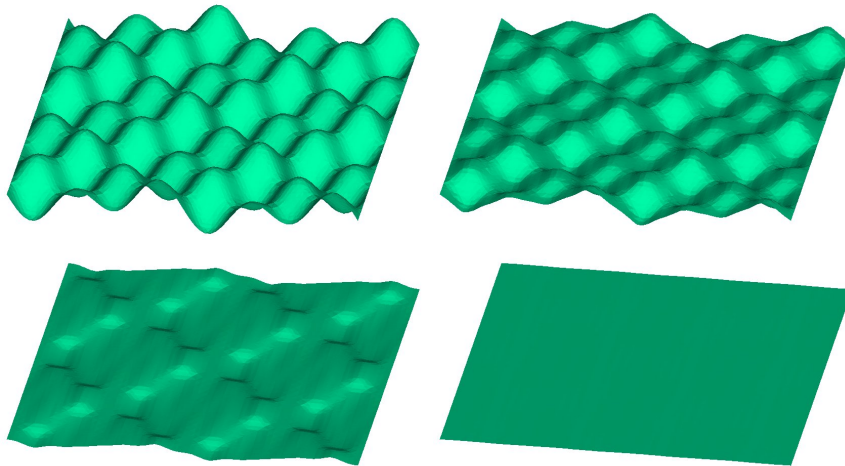


Figure 4.5: Evolution of surface under anisotropic mean curvature flow. $[-2, 2] \times [-2, 2] \times [-0.5, 0.5]$ grid, grid size $h = 0.05$, timestep $\Delta t = 0.001$, $\lambda = 5.0$. From top left to bottom right: $t = 0.0, 0.01, 0.03, 0.08$.

Non-closed curves and surfaces. We start with the evolution of sinusoidal curves and surfaces. In figure 4.4, an example in 2D is given, and figure 4.5 describes a surface evolution in 3D. As in isotropic situation, the high frequencies are damped first, before the lower frequencies are smoothed on a larger time scale. In the beginning of the evolution, the formation of flat areas can be observed. But this surface structure is not in equilibrium, since it is energetically more favorable to reduce the length of the flat areas and the velocity direction in each point is the direction towards the completely flat structure. The equilibrium shape for non-closed curves and surfaces is the flat line.

In figure 4.6, again an example for a non-closed curve that cannot be represented as the graph of a function is given. First, locally the shape of the wulffshape is attained before the curve flattens on a very large timescale.

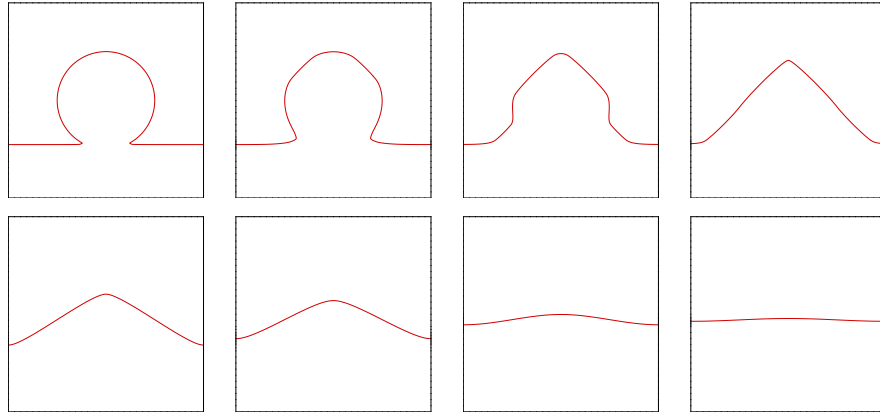


Figure 4.6: Evolution of curve under anisotropic mean curvature flow. $[0, 4] \times [0, 4]$ grid, grid size $h = 0.03125$, timestep $\Delta t = 0.001$, $\lambda = 10.0$. From top left to bottom right: $t = 0.0, 0.02, 0.1, 0.2, 1.0, 2.0, 10.0, 20.0$.

4.6.2 Surface diffusion

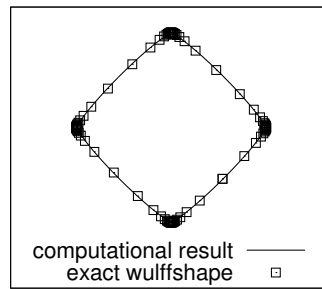


Figure 4.7: Comparison of computational result and exact wulffshape for the evolution of a curve with the initial shape of a circle under anisotropic surface diffusion, see figure 4.8 for the evolution.

Validation of the computational results. As a test for the correctness of the evolution, we compare the equilibrium shape reached in the evolution of a circle under anisotropic surface diffusion with the predicted one, which is the wulffshape of the anisotropy function. The volume is conserved under surface diffusion, so the volume enclosed by the wulffshape is that of the initial circle. Figure 4.7 shows that the computations match quite well the predicted shape. The volume change in this example is only about 0.08%.

Closed curves and surfaces. In figure 4.8 the evolution of a circle towards the equilibrium shape under anisotropic mean flow is presented. As in the isotropic situation, the wulffshape is reached in much shorter time than in the evolution under mean curvature flow. The counterpart in 3D, the evolution of a sphere towards the wulffshape, is given in figure 4.9.

Non-closed curves and surfaces. In figures 4.10 and 4.11 the evolution of a sinusoidal structure under anisotropic surface diffusion in 2D and 3D respectively is given. The anisotropy first causes a hill-valley structure with flat areas separated by small high-curvature parts. As in anisotropic mean curvature situation this structure is not in equilibrium and the evolution ends up with a flat line and surface respectively.

In the evolution of an omega-like shape under anisotropic surface diffusion in figure 4.12, the local formation with respect to the wulffshape is more dominant than under anisotropic surface diffusion. Finally, evolution reaches the flat line as equilibrium shape, as expected.

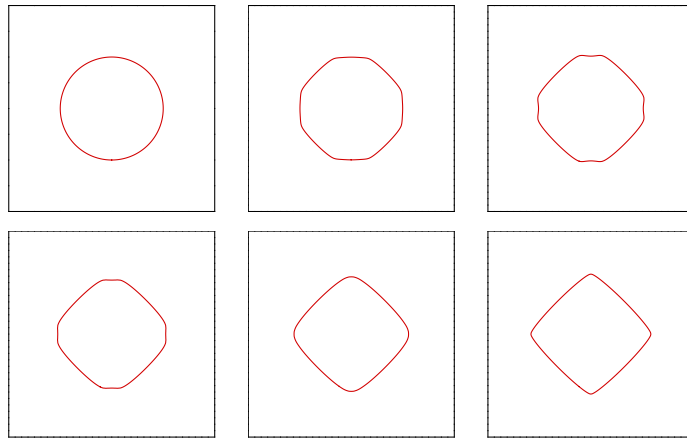


Figure 4.8: Evolution of curve under anisotropic surface diffusion. $[0, 4] \times [0, 4]$ grid, grid size $h = 0.03125$, timestep $\Delta t = 10^{-6}$, $\lambda = 10.0$. From top left to bottom right: $t = 0.0, 0.0005, 0.002, 0.003, 0.005, 0.008$.

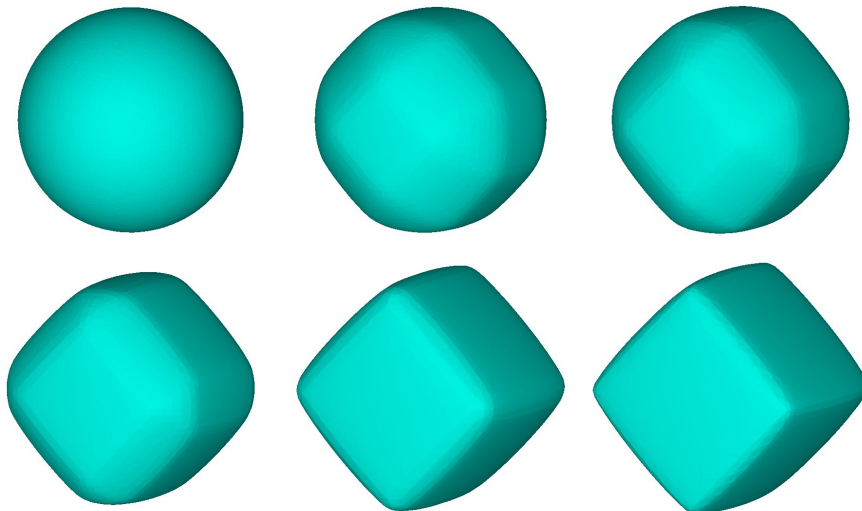


Figure 4.9: Evolution of surface under anisotropic surface diffusion. $[0, 4] \times [0, 4] \times [0, 4]$ grid, grid size $h = 0.05$, timestep $\Delta t = 10^{-5}$, $\lambda = 20.0$. From top left to bottom right: $t = 0.0, 0.0005, 0.001, 0.002, 0.005, 0.008$.

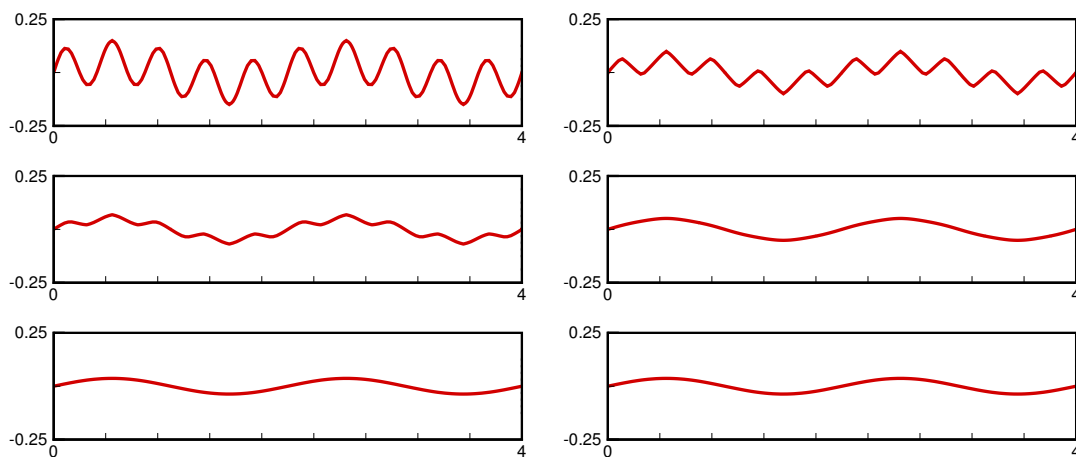


Figure 4.10: Evolution of curve under anisotropic surface diffusion. $[0, 4] \times [-1, 1]$ grid, grid size $h = 0.03125$, timestep $\Delta t = 10^{-6}$, $\lambda = 10.0$. From top left to bottom right: $t = 0.0, 0.0001, 0.0005, 0.002, 0.05, 1.0$.

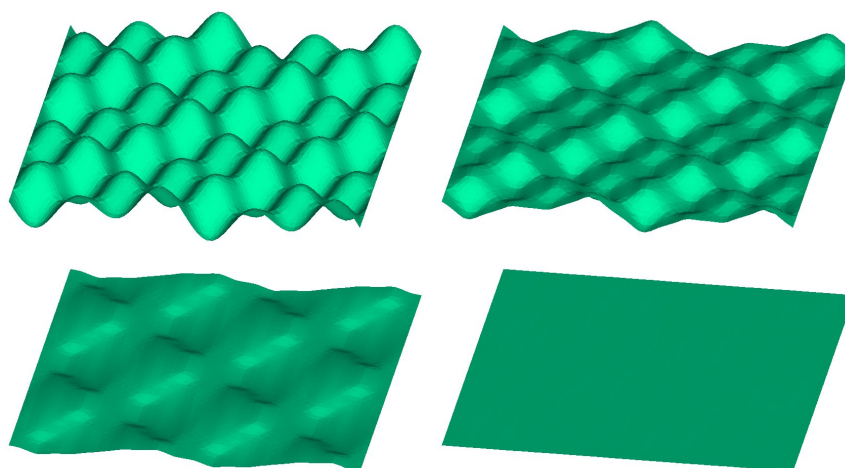


Figure 4.11: Evolution of surface under anisotropic surface diffusion. $[-2, 2] \times [-2, 2] \times [-0.5, 0.5]$ grid, grid size $h = 0.05$, timestep $\Delta t = 10^{-5}$, $\lambda = 20.0$. From top left to bottom right: $t = 0.0, 0.0003, 0.001, 0.004$.

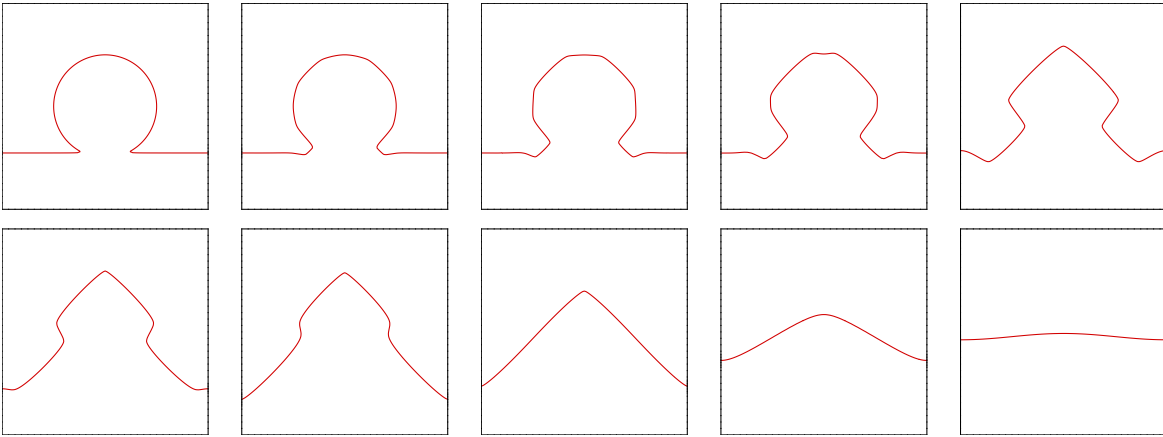


Figure 4.12: Evolution of curve under anisotropic surface diffusion. $[0, 4] \times [0, 4]$ grid, grid size $h = 0.03125$, timestep $\Delta t = 10^{-6}$, $\lambda = 10.0$. From left to right: $t = 0.0$, $t = 0.0001$, 0.0005 , 0.002 , 0.01 , 0.03 , $t = 0.05$, 0.2 , 1.0 , 8.0 .

Volume conservation and energy dissipation. In the numerical examples considered for the volume conserving evolution of anisotropic surface diffusion, the change in volume is at most 2%, which is reached for the example in figure 4.12. In the other examples the change in volume measures only up to 0.25%. For the evolution of a sphere in figure 4.9 the development of the volume and energy is depicted in figure 4.13.

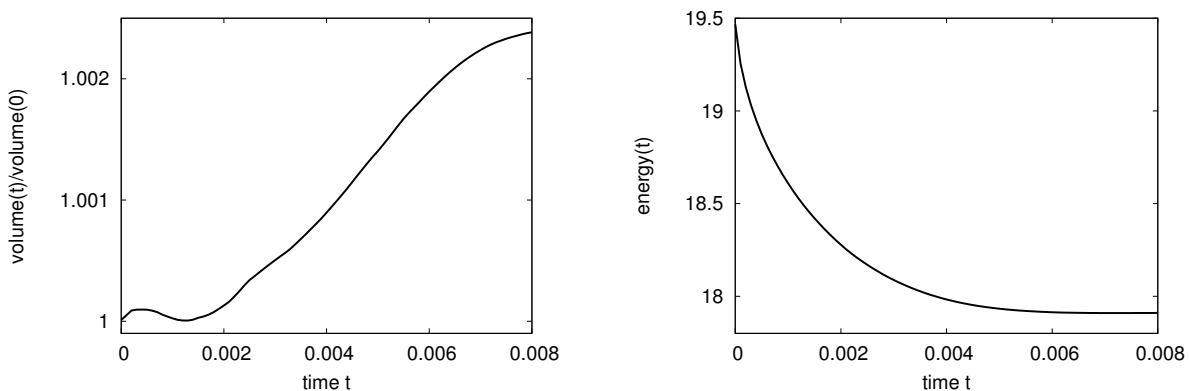


Figure 4.13: Change of volume (left) and energy dissipation (right) in evolution under anisotropic surface diffusion for the example in figure 4.9.

4.6.3 Kinetic model

The major result from the computations in the isotropic kinetic model was, first, that the evolution under surface diffusion is much faster than under surface diffusion with kinetics, and second, that surface diffusion with kinetics with the mobility coefficient m in the magnitude of one or higher shows the evolution behavior of volume-conserving mean curvature flow and by this is close to the evolution under mean curvature flow if one neglects the volume decrease. The numerical examples are chosen in the spirit to check whether the anisotropic situation reveals the same properties or not.

Validation of the computational results. First of all, we check again the computational results of the kinetic model in the limiting cases of mean curvature flow and surface diffusion in

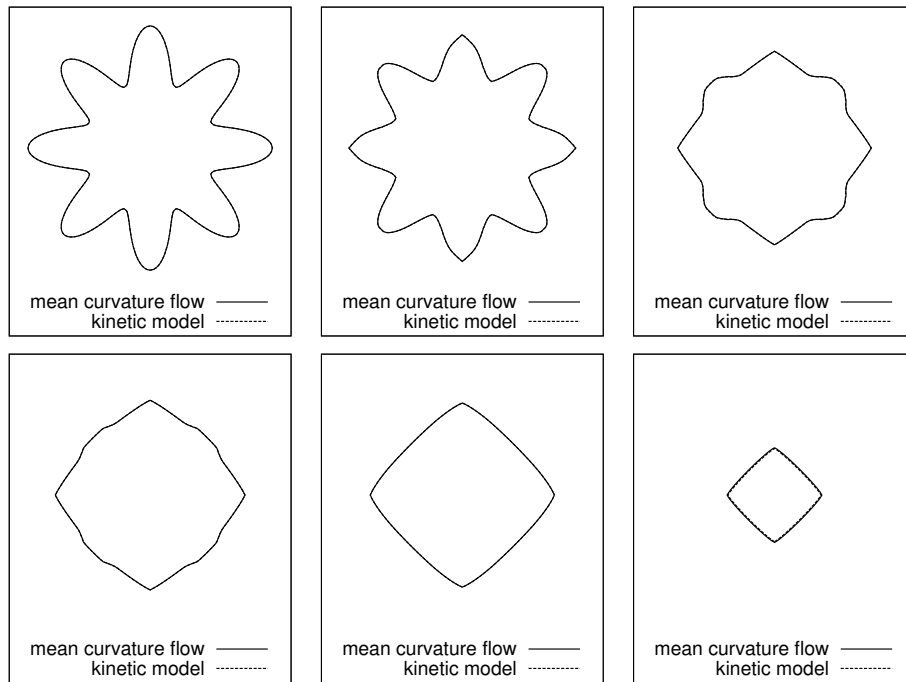


Figure 4.14: Comparison of mean curvature flow and kinetic model with $b = 0.0001$, $c = 1.0$ and $m = 0.0001$. $[0, 4] \times [0, 4]$ grid, grid size $h = 0.03125$, timestep $\Delta t = 0.001$, $\lambda = 10.0$. From top left to bottom right: $t = 0.0, 0.01, 0.05, 0.07, 0.1, 0.3$.

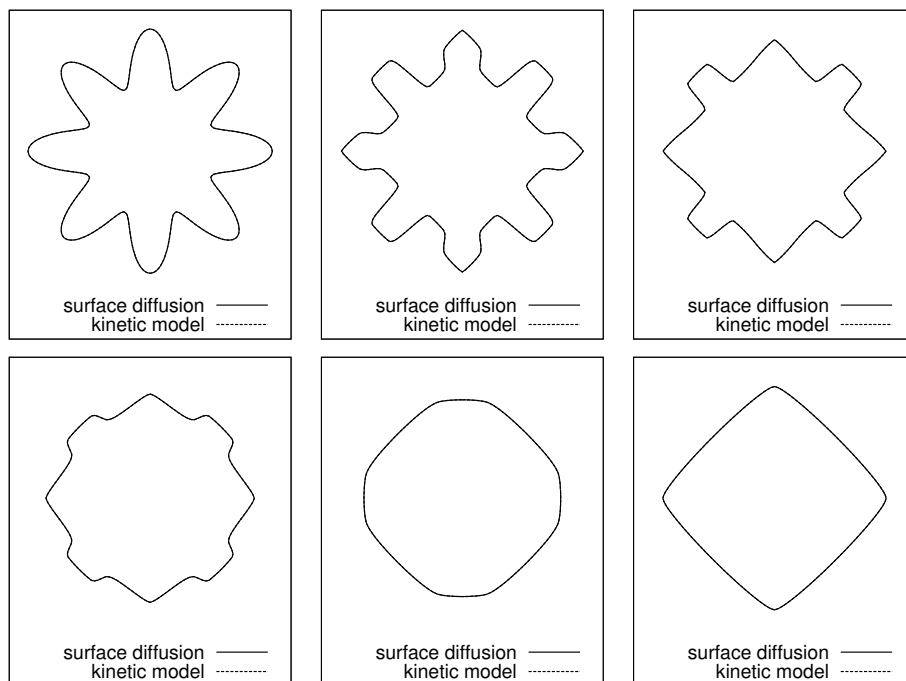


Figure 4.15: Comparison of surface diffusion and kinetic model with $b = 0.0001$, $c = 0.0001$ and $m = 1.0$. $[0, 4] \times [0, 4]$ grid, grid size $h = 0.03125$, timestep $\Delta t = 10^{-6}$, $\lambda = 10.0$. From top left to bottom right: $t = 0.0, 0.0001, 0.0005, 0.001, 0.003, 0.01$.

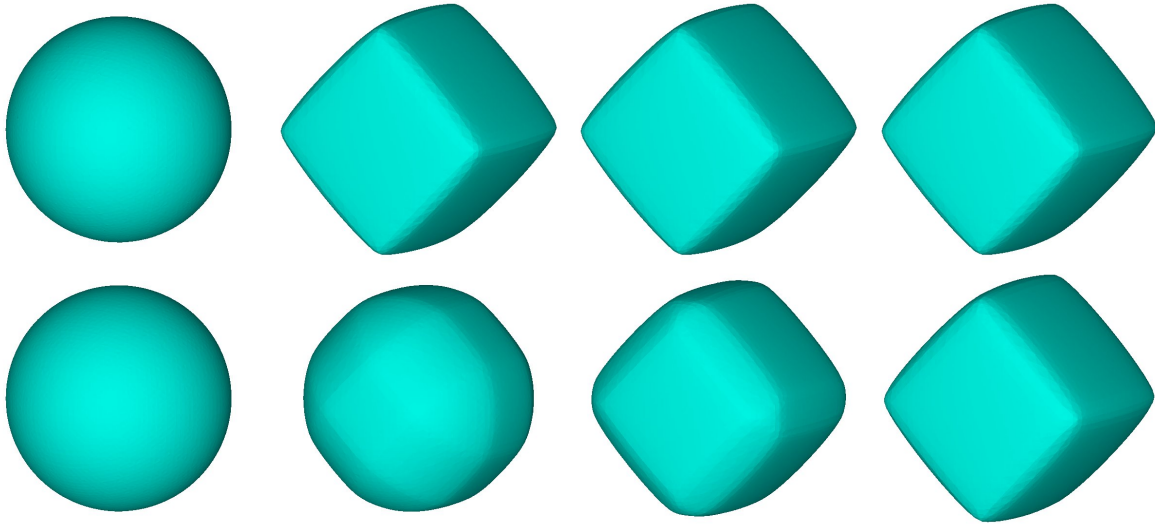


Figure 4.16: Comparison of surface diffusion (top) and surface kinetics with $b = 1.0$, $m = 1.0$ (bottom). $[0, 4] \times [0, 4] \times [0, 4]$ grid, grid size $h = 0.05$, timestep $\Delta t = 10^{-5}$ (surface diffusion) and $\Delta t = 0.0001$ (surface kinetics), $\lambda = 20.0$. From left to right: $t = 0.0, 0.008, 0.05, 0.1$.

the same way as in the isotropic situation. The comparison of the results in figure 4.14 and 4.15 confirms the correctness of our computations. The results for anisotropic mean curvature flow and the anisotropic kinetic model with the parameter choice close to mean curvature flow are undistinguishable. The same for anisotropic surface diffusion. What again is remarkable and can be observed quite well in the example with the initially star-like shape, is the difference between anisotropic mean curvature flow and anisotropic surface diffusion, in the way they evolve towards the wulffshape. Again, we note, that the property to adapt locally to the wulffshape is much stronger for anisotropic surface diffusion than for anisotropic mean curvature flow.

Comparison with surface diffusion and mean curvature flow. We compare the evolution under the anisotropic model of surface diffusion with kinetics, where again we choose the parameters $m = 1$ and $b = 1$, with the evolution under anisotropic surface diffusion and anisotropic mean curvature flow respectively. We use the initial shape of a circle in the 2D situation in figure 4.14 and the initial shape of a sphere in the 3D situation in figure 4.15. The numerical results correspond to our observations in the isotropic situation. Surface diffusion is much faster than surface diffusion with kinetics, and surface diffusion with kinetics shows the behavior of volume-conserving mean curvature flow.

Volume conservation. The change of volume in the two numerical examples for surface diffusion with kinetics measures at most 0.9%.

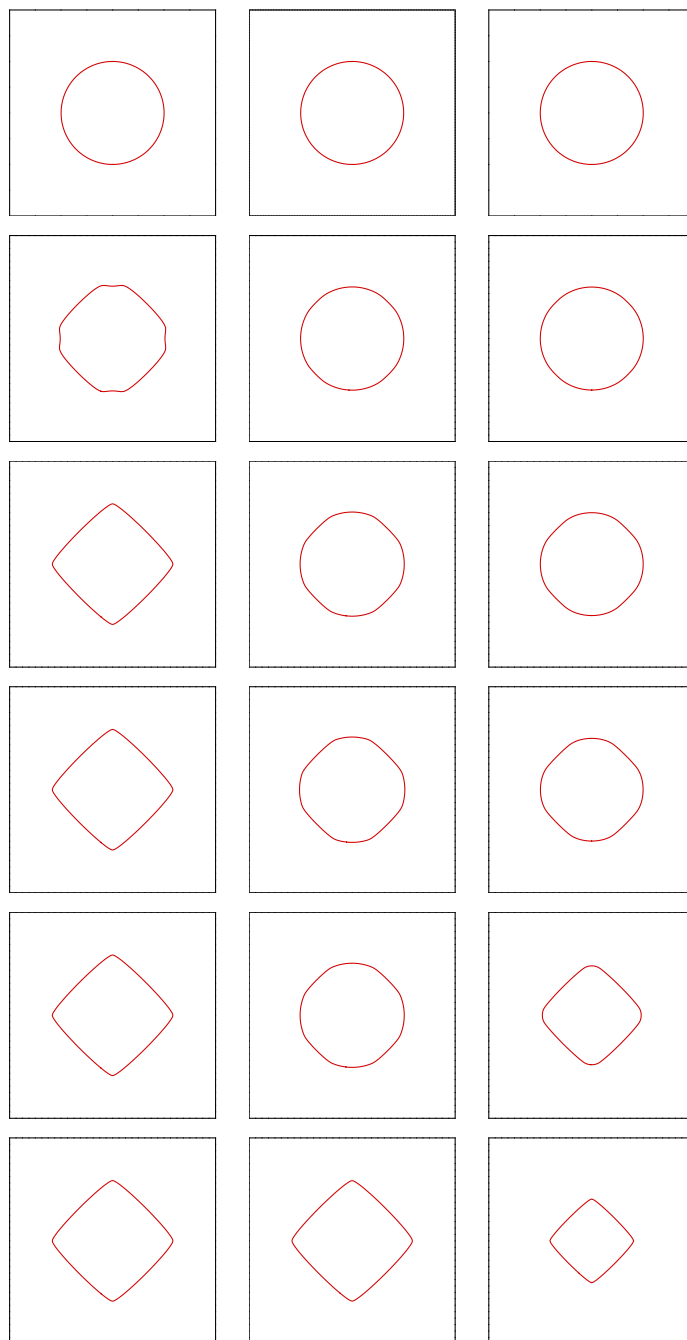


Figure 4.17: Comparison of surface diffusion (left), surface kinetics with $b = 1.0$, $m = 1.0$ (center) and mean curvature flow (right). $[0, 4] \times [0, 4]$ grid, grid size $h = 0.03125$, timestep $\Delta t = 10^{-6}$ (surface diffusion and surface kinetics) and $\Delta t = 0.001$ (mean curvature flow), $\lambda = 10.0$. From top to bottom: $t = 0.0, 0.002, 0.01, 0.02, 0.1, 0.2$.

Chapter 5

Evolution laws with strong anisotropies

Accounting for a special effect occurring in growth processes, we now consider evolution depending on non-convex anisotropy functions, also called strong anisotropies. A motivation for using non-convex anisotropy functions lies in their relation to the phenomenon of faceting in thin film growth, where one important application in 3D is the self-organized formation of quantum dots. The formation of facets may have different physical reasons. It may result from elastic stress due to lattice misfits between the substrate and the crystalline surface, see [58, 75], the occurrence of strong anisotropies during thermodynamic processes, [62, 42, 56], or many others. In this work we concentrate on the formation of facets caused by strong anisotropies.

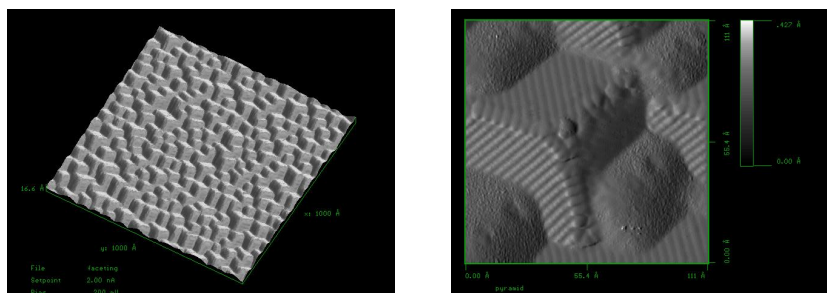


Figure 5.1: Faceted structure of a tungsten surface with zoom in on the right¹.

Let us first of all draw a brief outline of the thermodynamic process producing strong anisotropies. The structure of a film surface highly depends on the temperature in the system. At a certain material dependent temperature the film surface is completely flat. When suddenly decreasing the temperature, the surface becomes unstable. It breaks up spontaneously and forms facets at a small length scale. See figure 5.1 for the faceted structure of a tungsten surface on a nanoscale. The facets are separated by corners and edges. Whether these corners and edges are sharp or rounded also depends on the temperature. The authors in [67] experimentally found out that only for 0K the faceted structure of tungsten reveals sharp corners and edges. At an increase of temperature, corners and edges are rounded. The corner and edge roundings can be seen on the right in figure 5.1. After the formation of facets, the coarsening process starts. Rounded corners and edges, where facets change their orientation, are related to high energies. So it is energetically more favorable to reduce the number of corners and edges. This happens during coarsening, where neighboring facets merge to form bigger facets. In this work we only consider temperatures where corners and edges are rounded, because this corresponds to the

¹Figures produced with Scanning Tunneling Microscope by C.-H. Nien and T. E. Madey, see [43] and [48].

physically realistic temperature ranges. We investigate the dynamic evolution of the faceting and coarsening process towards the equilibrium shape.

Next, we discuss the problem of instability which arises by the use of strong anisotropies and how it is overcome by introducing a regularization technique which accounts for the relation between corners / edges and high energy contributions. Then we present the equations for mean curvature flow, surface diffusion and the kinetic model with non-convex anisotropies. We will see, that the regularization leads to an increase by two in the order of the equations. And finally, we discuss the computational results.

5.1 Non-convex anisotropies

The level set formulation of the evolution law $V = -H_\gamma$ results in the second order parabolic equation

$$\frac{\phi_t}{|\nabla\phi|} = \nabla \cdot D\gamma(\nabla\phi).$$

Considering the equation in 2D, where $\nabla \cdot D\gamma(\nu) = \tilde{\gamma}H$, we obtain with $|\nabla\phi| = 1$

$$\phi_t = \tilde{\gamma}\Delta\phi, \quad (5.1)$$

which is the heat equation with an orientation dependent coefficient $\tilde{\gamma}$. If the stiffness $\tilde{\gamma}$ is positive, equation (5.1) is well-posed. This is the case for convex anisotropy functions γ . But for non-convex anisotropies, the stiffness $\tilde{\gamma}$ is negative for certain orientations, and equation (5.1) is backwards parabolic in these areas and thus unstable. To illustrate what happens in the

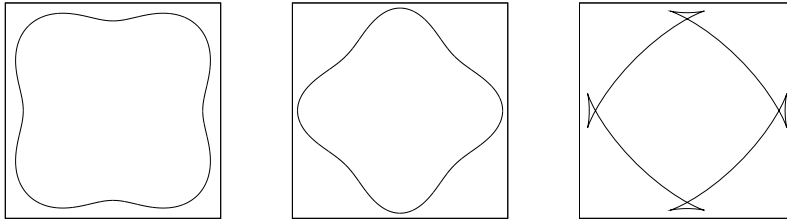


Figure 5.2: Polar plot of anisotropy function, its inverse and the corresponding wulffshape for the anisotropy defined in (5.2).

wulffshape for non-convex anisotropies let us look at figure 5.2. On the left the figure provides the polar plot of the anisotropy function

$$\gamma(p) = |p| + a \sum_{i=1}^d \frac{p_i^4}{|p|^3} \quad (5.2)$$

with $a = 1.0$. The anisotropy function is convex for values $a \leq 1/3$ and non-convex for $a > 1/3$. The polar plot of $1/\gamma$ in the middle is non-convex and by this reveals the non-convexity of γ . Due to the negative stiffness, swallowtails appear in the polar plot of $D\gamma(S^1)$ on the right. We obtain the wulffshape of γ by omitting these swallowtails. That means in the wulffshape of γ certain orientations, among them the orientations with negative stiffness, are excluded and replaced by corners. The excluded orientations are called missing orientations. Figure 5.3 illustrates the jump in the orientations at the corners of the wulffshape.

There are different approaches to deal with unstable orientations. One possibility is to allow for sharp corners and edges in the surface. For faceting in 3D under surface diffusion, this approach is followed in [74]. By the formation of sharp corners and edges the unstable

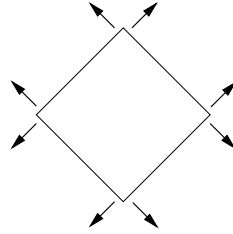


Figure 5.3: Missing orientations at the corners of the wulffshape.

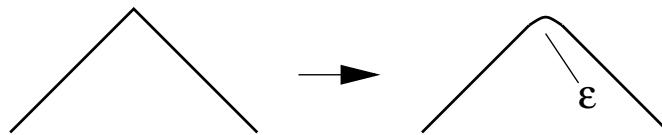
orientations are excluded from the surface and the equations become stable. Another possibility is considered in [30] where a convexification of the strong anisotropy function is used. This approach does not account for the formation of facets from an initially flat or slightly perturbed flat surface and is thus rather restrictive. Neither of the approaches presented so far results in corner and edge roundings. We therefore follow another approach which matches to this effect. It is based on a regularization of the surface free energy density γ by a higher order curvature term and has been introduced in [25] for the strong anisotropic mean curvature problem in 2D. A curvature depending anisotropy has already been proposed earlier by Herring in [39], where the equilibrium shape of faceted crystals is investigated in physical context. The authors in [53] propose a higher-order regularization including not only the mean curvature but also its derivative, which means the use of an anisotropy function of the form $\hat{\gamma}(\nu, H, \nabla_{\Gamma} H)$. The principal idea in [25] is to add a higher order term in the anisotropy function depending on the mean curvature of the surface, which gives the anisotropy

$$\hat{\gamma}(\nu, H) = \gamma(\nu) + \frac{1}{2}\epsilon^2 H^2$$

with small $\epsilon > 0$. The surface energy then reads

$$E[\Gamma] = \int_{\Gamma} \gamma + \frac{1}{2}\epsilon^2 H^2 dA, \quad (5.3)$$

which is the sum of the energy functional (4.1) considered in the previous chapters and the Willmore functional. The approach has been broadly discussed and applied in the literature. In [35] it was extended to 3D, and in [35] and [56] it was also considered for curvature regularized surface diffusion. The dynamic evolution of faceting and coarsening for one-dimensional surfaces is treated by a parametric approach in [38] and [36] for mean curvature flow and surface diffusion respectively. In [9], curvature regularized surface diffusion is considered in 2D and 3D within a graph formulation.

Figure 5.4: Corner rounding on a length scale of ϵ .

We now turn to the effect of the regularization on the evolution. Surface changes are towards energy decrease. Thus, the higher order mean curvature term in (5.3) leads to a penalization of high curvatures in the surface geometry. Sharp corners are smeared out to rounded corners. That means the dynamic evolution produced by the regularization provides the desired physical effect. The radius of the rounding is determined by the interplay of two contrary energy arguments. On the one hand a larger radius leads to larger surface area and thus higher energy. Following

this argument, the radius has to be small. On the other hand, the smaller the radius the higher the curvature, which leads to a higher energy due to the curvature term. In [60] the equilibrium shape of the regularized problem is analyzed. It is shown that the regularization (5.3) leads to corner roundings with the radius ϵ . The wulffshape of the regularized problem is now an adaption of the wulffshape of γ in figure 5.2. The sharp corners are replaced by rounded corners with the radius ϵ , see figure 5.4. The authors in [60] also proofed that if ϵ tends to zero, the wulffshape of the regularized problem converges to the wulffshape of γ .

As discussed in the previous chapters, the driving force for the evolution is the chemical potential μ which in the case of mean curvature flow and surface diffusion is the variational derivative of the energy functional in normal directions. The regularization of the energy term now changes the variational derivative to

$$\frac{\delta E}{\delta \Gamma} = H_\gamma - \epsilon^2(\Delta_\Gamma H + H(\|S\|^2 - \frac{1}{2}H^2)). \quad (5.4)$$

Here, $S = \nabla_\Gamma \nu$ is the shape operator and $\|S\|^2 = \sqrt{\text{trace}(SS^T)}$ its Frobenius norm. The second term is the variational derivative of the Willmore functional, see e.g. [71]. In 2D, equation (5.4) reads

$$\frac{\delta E}{\delta \Gamma} = \tilde{\gamma}H - \epsilon^2(\Delta_\Gamma H + \frac{1}{2}H^3).$$

In figure 5.2 areas with negative stiffness are within the missing orientations of the wulffshape. They correspond to the corners in the wulffshape and thus areas with high curvature. So the occurrence of negative stiffness in the chemical potential is equalized by the high curvature terms in the regularization.

Coarsening of a completely faceted surface can also be considered as a spinodal decomposition process of the facet orientations. The connection of the coarsening process to the equations of spinodal decomposition has been depicted e.g. in [42] and [25].

5.2 Curvature regularized mean curvature flow

In the evolution law of mean curvature flow the normal velocity of the surface motion is proportional to the negative chemical potential $\mu = \frac{\delta E}{\delta \Gamma}$, which reads

$$V = -c\mu.$$

The chemical potential (5.4) now includes the regularization of the strong anisotropy, and the evolution law (4.5) is changed to

$$\begin{aligned} V &= -c\left(H_\gamma - \epsilon^2(\Delta_\Gamma H + H(\|S\|^2 - \frac{1}{2}H^2))\right) \\ &= -c\left(H_\gamma + \epsilon^2\mu_w\right), \end{aligned} \quad (5.5)$$

where we define

$$\mu_w := -(\Delta_\Gamma H + H(\|S\|^2 - \frac{1}{2}H^2)), \quad (5.6)$$

which is the variational derivative of the Willmore energy $\int_\Gamma \frac{1}{2}H^2 dA$ with respect to variations in normal directions. With $\Delta_\Gamma H$ being a fourth order term, the evolution law for mean curvature flow has now turned from second to fourth order in its regularized version. The formulation in terms of the level set function can be achieved by replacing the mean curvature terms appropriately by their level set representation. But finding a formulation which offers an easy calculation of the weak formulation is not straight forward for the part coming in from the Willmore energy.

The authors in [27] derivate a weak formulation for isotropic Willmore flow in two different ways. First, it is calculated as the gradient descent flow of an energy functional. And to demonstrate the elegant character of the energy approach, it is afterwards verified by the naive approach of multiplying (5.6) by test functions and integrating which necessitates tedious calculations. The weak formulation provided in [27] reads

$$\begin{aligned} \int_{\Omega} \mu_w \eta \, dx &= - \int_{\Omega} (\Delta_{\Gamma} H + H(\|S\|^2 - \frac{1}{2}H^2)) \eta \, dx \\ &= -\frac{1}{2} \int_{\Omega} \frac{(|\nabla \phi \, H|)^2}{|\nabla \phi|^3} \nabla \phi \cdot \nabla \eta \, dx + \int_{\Omega} \frac{P_{\Gamma} \nabla(|\nabla \phi| \, H)}{|\nabla \phi|} \cdot \nabla \eta \, dx \end{aligned} \quad (5.7)$$

for all test functions $\eta, \xi \in C_0^{\infty}(\Omega)$. The mean curvature H brings a second order derivative into the integral terms. Following [27], we overcome this problem by introducing a new variable $\omega := -|\nabla \phi| \, H$ and splitting the equation in two equations. This results in

$$\int_{\Omega} \mu_w \eta \, dx = -\frac{1}{2} \int_{\Omega} \frac{\omega^2}{|\nabla \phi|^3} \nabla \phi \cdot \nabla \eta \, dx - \int_{\Omega} \frac{P_{\Gamma} \nabla \omega}{|\nabla \phi|} \cdot \nabla \eta \, dx \quad (5.8)$$

$$\int_{\Omega} \frac{\omega}{|\nabla \phi|} \xi \, dx = \int_{\Omega} \frac{\nabla \phi}{|\nabla \phi|} \cdot \nabla \xi \, dx \quad (5.9)$$

for all test functions $\eta, \xi \in C_0^{\infty}(\Omega)$. For the time discretization of the Willmore flow equations the authors in [27] propose to extend the operator P_{Γ} in the second integral term of equation (5.8) into

$$P_{\Gamma} = I - (I - P_{\Gamma}),$$

and then to treat the first operator implicitly and the second explicitly. By this, they obtain a symmetric linear system, and for the same reason, we also apply this extension. The discretized form of equations (5.8) and (5.9) then ends up to

$$\begin{aligned} \int_{\Omega} \mu_w^{k+1} \eta \, dx &= -\frac{1}{2} \int_{\Omega} \frac{(\omega^k)^2}{|\nabla \phi^k|_{\delta}^3} \nabla \phi^{k+1} \cdot \nabla \eta \, dx - \int_{\Omega} \frac{\nabla \omega^{k+1}}{|\nabla \phi^k|_{\delta}} \cdot \nabla \eta \, dx \\ &\quad + \int_{\Omega} \frac{(I - P_{\Gamma}^k) \nabla \omega^k}{|\nabla \phi^k|_{\delta}} \cdot \nabla \eta \, dx \end{aligned} \quad (5.10)$$

$$\int_{\Omega} \frac{\omega^{k+1}}{|\nabla \phi^k|_{\delta}} \xi \, dx = \int_{\Omega} \frac{\nabla \phi^{k+1}}{|\nabla \phi^k|_{\delta}} \cdot \nabla \xi \, dx \quad (5.11)$$

for all $\eta, \xi \in \mathcal{V}^h$. This is our discretization scheme for the regularization term μ_w . With the equations for anisotropic mean curvature flow derived in section 4.2, it is now easy to get the full discretized equations for evolution law (5.5). With (4.6), (5.8) and (5.9) the weak formulation reads

$$\begin{aligned} \int_{\Omega} \frac{1}{c} \frac{\partial_t \phi}{|\nabla \phi|} \eta \, dx &= - \int_{\Omega} D\gamma(\nabla \phi) \cdot \nabla \eta \, dx \\ &\quad - \frac{\epsilon^2}{2} \int_{\Omega} \frac{\omega^2}{|\nabla \phi|^3} \nabla \phi \cdot \nabla \eta \, dx - \epsilon^2 \int_{\Omega} \frac{P_{\Gamma} \nabla \omega}{|\nabla \phi|} \cdot \nabla \eta \, dx \end{aligned} \quad (5.12)$$

$$\int_{\Omega} \frac{\omega}{|\nabla \phi|} \xi \, dx = \int_{\Omega} \frac{\nabla \phi}{|\nabla \phi|} \cdot \nabla \xi \, dx \quad (5.13)$$

for all test functions $\eta, \xi \in C_0^{\infty}(\Omega)$. And with the semi-implicit discretization scheme of the weighted mean curvature term in (4.7) and the discretization of the regularization term in (5.10)

and (5.11) the discretized equations for (5.5) read

$$\begin{aligned}
0 &= \int_{\Omega} \frac{1}{c} \frac{(\phi^{k+1} - \phi^k)}{\tau |\nabla \phi^k|_{\delta}} \eta \, dx + \int_{\Omega} D\gamma(\nabla \phi^k) \cdot \nabla \eta \, dx \\
&+ \lambda \int_{\Omega} \gamma \left(\frac{\nabla \phi^k}{|\nabla \phi^k|_{\delta}} \right) \frac{(\nabla \phi^{k+1} - \nabla \phi^k)}{|\nabla \phi^k|_{\delta}} \cdot \nabla \eta \, dx \\
&+ \frac{\epsilon^2}{2} \int_{\Omega} \frac{(\omega^k)^2}{|\nabla \phi^k|_{\delta}^3} \nabla \phi^{k+1} \cdot \nabla \eta \, dx \\
&+ \epsilon^2 \int_{\Omega} \frac{\nabla \omega^{k+1}}{|\nabla \phi^k|_{\delta}} \cdot \nabla \eta \, dx - \epsilon^2 \int_{\Omega} \frac{(I - P_{\Gamma}^k) \nabla \omega^k}{|\nabla \phi^k|_{\delta}} \cdot \nabla \eta \, dx
\end{aligned} \tag{5.14}$$

$$0 = \int_{\Omega} \frac{\omega^{k+1}}{|\nabla \phi^k|_{\delta}} \xi \, dx - \int_{\Omega} \frac{\nabla \phi^{k+1}}{|\nabla \phi^k|_{\delta}} \cdot \nabla \xi \, dx \tag{5.15}$$

for all $\eta, \xi \in \mathcal{V}^h$. To describe the linear system which has to be solved in timestep $k+1$, we define the system matrices

$$\begin{aligned}
M_1 &:= M\left[\frac{1}{c} |\nabla \phi^k|_{\delta}^{-1}\right], & L_3 &:= L[|\nabla \phi^k|_{\delta}^{-1}], \\
M_2 &:= M[|\nabla \phi^k|_{\delta}^{-1}], & L_4 &:= L[(I - P_{\Gamma}^k) |\nabla \phi^k|_{\delta}^{-1}], \\
L_1 &:= L\left[\gamma \left(\frac{\nabla \phi^k}{|\nabla \phi^k|_{\delta}} \right) |\nabla \phi^k|_{\delta}^{-1}\right], & R_1 &:= \left(\int_{\Omega} D\gamma(\nabla \phi^k) \cdot \nabla \varphi_i \right)_i \\
L_2 &:= L[(\omega^k)^2 |\nabla \phi^k|_{\delta}^{-3}].
\end{aligned}$$

With the linear expansions

$$\phi^k = \sum_{i=1}^N \bar{\phi}_i^k \varphi_i, \quad \omega^k = \sum_{i=1}^N \bar{\omega}_i^k \varphi_i$$

the linear system reads

$$\begin{pmatrix} M_1 + \tau \lambda L_1 + \tau \frac{\epsilon^2}{2} L_2 & \tau \epsilon^2 L_3 \\ -L_3 & M_2 \end{pmatrix} \begin{pmatrix} \bar{\phi}^{k+1} \\ \bar{\omega}^{k+1} \end{pmatrix} = \begin{pmatrix} M_1 \bar{\phi}^k + \tau \lambda L_1 \bar{\phi}^k + \tau \epsilon^2 L_4 \bar{\omega}^k - \tau R_1 \\ 0 \end{pmatrix}.$$

The Schur complement approach delivers

$$(M_1 + \tau \lambda L_1 + \tau \frac{\epsilon^2}{2} L_2 + \tau \epsilon^2 L_3 M_2^{-1} L_3) \bar{\phi}^{k+1} = M_1 \bar{\phi}^k + \tau \lambda L_1 \bar{\phi}^k + \tau \epsilon^2 L_4 \bar{\omega}^k - \tau R_1.$$

Note, that the right hand side depends on the weighted curvature term $\bar{\omega}^k$ of the last timestep. In each timestep, it is calculated in a preprocessing step through $\bar{\omega}^k = M_2^{-1} L_3 \bar{\phi}^k$. Here, as well as in the application of the Schur complement, mass lumping is used for the operator M_2^{-1} . The symmetric and positive definite system is solved with a CG-solver.

5.3 Curvature regularized surface diffusion

We follow the same scheme as for curvature regularized mean curvature flow to derive the evolution law, the level set formulation and the fully discretized scheme for the evolution under curvature regularized surface diffusion. In terms of the chemical potential μ , which in the model

of surface diffusion is equal to the variational derivative of the energy functional, $\mu = \frac{\delta E}{\delta \Gamma}$, the evolution law for surface diffusion can be written as

$$V = \nabla_{\Gamma} \cdot (m \nabla_{\Gamma} \mu).$$

With the variational derivative (5.4) of the curvature regularized energy functional (5.3), the evolution law for curvature regularized surface diffusion reads

$$V = \nabla_{\Gamma} \cdot \left(m \nabla_{\Gamma} \left(H_{\gamma} - \epsilon^2 (\Delta_{\Gamma} H + H(\|S\|^2 - \frac{1}{2} H^2)) \right) \right). \quad (5.16)$$

Since the mean curvature H in level set formulation is a second order term, the regularization again leads to an increase by two in the order of the equation, which results in a 6th-order non-linear parabolic equation. With the weak formulation of anisotropic surface diffusion in (4.8) and (4.9) and the weak formulation of the regularization term $-\epsilon^2 (\Delta_{\Gamma} H + H(\|S\|^2 - \frac{1}{2} H^2))$ in (5.8) and (5.9), we obtain the weak formulation of (5.16) by

$$\begin{aligned} \int_{\Omega} \phi_t \eta \, dx &= \int_{\Omega} m |\nabla \phi| P_{\Gamma} \nabla \mu \cdot \nabla \eta \, dx \\ \int_{\Omega} \mu \xi \, dx &= - \int_{\Omega} D\gamma(\nabla \phi) \cdot \nabla \xi \, dx \\ &\quad - \frac{\epsilon^2}{2} \int_{\Omega} \frac{\omega^2}{|\nabla \phi|^3} \nabla \phi \cdot \nabla \xi \, dx - \epsilon^2 \int_{\Omega} \frac{P_{\Gamma} \nabla \omega}{|\nabla \phi|} \cdot \nabla \xi \, dx \\ \int_{\Omega} \frac{\omega}{|\nabla \phi|} \zeta \, dx &= \int_{\Omega} \frac{\nabla \phi}{|\nabla \phi|} \cdot \nabla \zeta \, dx \end{aligned}$$

for all test functions $\eta, \xi, \zeta \in C_0^{\infty}(\Omega)$. This is a system of three second order equations in weak form. We apply the semi-implicit discretization scheme of the weighted mean curvature term in (4.7) and the discretization of the regularization term in (5.10) and (5.11), and obtain the fully discrete scheme for (5.16)

$$0 = \int_{\Omega} \phi^{k+1} \eta \, dx - \int_{\Omega} \phi^k \eta \, dx - \tau \int_{\Omega} m |\nabla \phi^k|_{\delta} P_{\Gamma}^k \nabla \mu^{k+1} \cdot \nabla \eta \, dx \quad (5.17)$$

$$\begin{aligned} 0 &= \int_{\Omega} \mu^{k+1} \xi \, dx + \int_{\Omega} D\gamma(\nabla \phi^k) \cdot \nabla \xi \, dx + \lambda \int_{\Omega} \frac{\gamma(\frac{\nabla \phi^k}{|\nabla \phi^k|_{\delta}})}{|\nabla \phi^k|_{\delta}} \nabla(\phi^{k+1} - \phi^k) \cdot \nabla \eta \, dx \\ &\quad + \frac{\epsilon^2}{2} \int_{\Omega} \frac{(\omega^k)^2}{|\nabla \phi^k|_{\delta}^3} \nabla \phi^{k+1} \cdot \nabla \xi \, dx \\ &\quad + \epsilon^2 \int_{\Omega} \frac{\nabla \omega^{k+1}}{|\nabla \phi^k|_{\delta}} \cdot \nabla \xi \, dx - \epsilon^2 \int_{\Omega} \frac{(I - P_{\Gamma}^k) \nabla \omega^k}{|\nabla \phi^k|_{\delta}} \cdot \nabla \xi \, dx \end{aligned} \quad (5.18)$$

$$0 = \int_{\Omega} \frac{\omega^{k+1}}{|\nabla \phi^k|_{\delta}} \zeta \, dx - \int_{\Omega} \frac{\nabla \phi^{k+1}}{|\nabla \phi^k|_{\delta}} \cdot \nabla \zeta \, dx \quad (5.19)$$

for all $\eta, \xi, \zeta \in \mathcal{V}^h$. With the system matrices

$$\begin{aligned} M_1 &:= M[1], & L_3 &:= L[(\omega^k)^2 |\nabla \phi^k|_{\delta}^{-3}], \\ M_2 &:= M[|\nabla \phi^k|_{\delta}^{-1}], & L_4 &:= L[|\nabla \phi^k|_{\delta}^{-1}], \\ L_1 &:= L[m |\nabla \phi^k|_{\delta} P_{\Gamma}^k], & L_5 &:= L[(I - P_{\Gamma}^k) |\nabla \phi^k|_{\delta}^{-1}], \\ L_2 &:= L[|\nabla \phi^k|_{\delta}^{-1} \gamma(\frac{\nabla \phi^k}{|\nabla \phi^k|_{\delta}})], & R_1 &:= \left(\int_{\Omega} D\gamma(\nabla \phi^k) \cdot \nabla \varphi_i \right)_i \end{aligned}$$

and the linear expansions

$$\begin{aligned}\phi^{k+1} &= \sum_{i=1}^N \bar{\phi}_i^{k+1} \varphi_i, \\ \mu^{k+1} &= \sum_{i=1}^N \bar{\mu}_i^{k+1} \varphi_i, \\ \omega^{k+1} &= \sum_{i=1}^N \bar{\omega}_i^{k+1} \varphi_i,\end{aligned}$$

the linear system resulting from (5.17)-(5.18) and which has to be solved in timestep $k+1$ reads

$$\begin{pmatrix} M_1 & -\tau L_1 & \\ \lambda L_2 + \frac{\epsilon^2}{2} L_3 & M_1 & \epsilon^2 L_4 \\ -L_4 & 0 & M_2 \end{pmatrix} \begin{pmatrix} \bar{\phi}^{k+1} \\ \bar{\mu}^{k+1} \\ \bar{\omega}^{k+1} \end{pmatrix} = \begin{pmatrix} M_1 \bar{\phi}^k \\ \lambda L_2 \bar{\phi}^k + \epsilon^2 L_5 \bar{\omega}^k - R_1 \\ 0 \end{pmatrix}.$$

Again, we use a Schur complement approach to solve the system, which is now applied to a system of three equations and gives

$$\begin{aligned} \left(M_1 + \tau L_1 M_1^{-1} (\lambda L_2 + \frac{\epsilon^2}{2} L_3 + \epsilon^2 L_4 M_1^{-1} L_4) \right) \bar{\phi}^{k+1} = \\ M_1 \bar{\phi}^k + \tau L_1 M_1^{-1} (\lambda L_2 \bar{\phi}^k + \epsilon^2 L_5 \bar{\omega}^k - R_1). \end{aligned}$$

As for curvature regularized mean curvature flow, the weighted curvature term $\bar{\omega}^k$ is calculated in a preprocessing step by $\bar{\omega}^k = M_2^{-1} L_4 \bar{\phi}^k$ in each timestep. The inverse matrices M_1^{-1} and M_2^{-1} are approximated with mass lumping. The non-symmetric linear system is solved with the Krylov-subspace method GMRES.

In [12], the semi-implicit time-discretization schemes, which have been presented in this section for curvature regularized surface diffusion and in the previous section for curvature regularized mean curvature flow, are derived within a gradient flow formulation. Furthermore, stability analysis is provided therein within the gradient flow framework, which guarantees stability for small timesteps of $\Delta t \sim h^4$ and $\Delta t \sim h^2$ respectively.

5.4 Kinetic model with curvature regularized anisotropy

The evolution law for the kinetic model with curvature regularization is obtained by using the variational derivative (5.4) of the curvature regularized energy functional (5.3) in the evolution law of the kinetic model (3.9) and (3.10) in its general formulation in terms of the variational derivative of an energy functional. The evolution law then reads

$$V = \nabla_{\Gamma} \cdot (m \nabla_{\Gamma} \mu) - c \mu \quad (5.20)$$

$$bV = -\left(H_{\gamma} - \epsilon^2 (\Delta_{\Gamma} H + H(\|S\|^2 - \frac{1}{2} H^2)) \right) + \mu \quad (5.21)$$

with the coefficients m , c and b as in section 3.3. Again, this is a 6th order non-linear parabolic equation. We derive the weak formulation by using the weak formulation of the regularization

term $-\epsilon^2(\Delta_\Gamma H + H(\|S\|^2 - \frac{1}{2}H^2))$, given in (5.8) and (5.9), which provides

$$\begin{aligned}
\int_{\Omega} \phi_t \eta \, dx &= \int_{\Omega} m |\nabla \phi| P_\Gamma \nabla \mu \cdot \nabla \eta \, dx + \int_{\Omega} c |\nabla \phi| \mu \eta \, dx \\
\int_{\Omega} b \frac{\phi_t}{|\nabla \phi|} \xi \, dx &= - \int_{\Omega} D\gamma(\nabla \phi) \cdot \nabla \xi \, dx \\
&\quad - \frac{\epsilon^2}{2} \int_{\Omega} \frac{\omega^2}{|\nabla \phi|^3} \nabla \phi \cdot \nabla \xi \, dx - \epsilon^2 \int_{\Omega} \frac{P_\Gamma \nabla \omega}{|\nabla \phi|} \cdot \nabla \xi \, dx \\
&\quad - \int_{\Omega} \mu \xi \, dx \\
\int_{\Omega} \frac{\omega}{|\nabla \phi|} \zeta \, dx &= \int_{\Omega} \frac{\nabla \phi}{|\nabla \phi|} \cdot \nabla \zeta \, dx
\end{aligned}$$

for all test functions $\eta, \xi, \zeta \in C_0^\infty(\Omega)$. This is a system of three second order equations in weak form. Our semi-implicit discretization scheme, which treats linear terms implicitly and non-linear terms explicitly, the semi-implicit treatment of the weighted mean curvature term in (4.7), and the discretization of the regularization term in (5.10) and (5.11) result in the fully discrete scheme for the evolution law (5.20) and (5.21) by

$$\begin{aligned}
0 &= \int_{\Omega} \phi^{k+1} \eta \, dx - \int_{\Omega} \phi^k \eta \, dx - \tau \int_{\Omega} m |\nabla \phi^k|_\delta P_\Gamma^k \nabla \mu^{k+1} \cdot \nabla \eta \, dx \\
&\quad - \tau \int_{\Omega} c |\nabla \phi^k|_\delta \mu^{k+1} \eta \, dx
\end{aligned} \tag{5.22}$$

$$\begin{aligned}
0 &= \int_{\Omega} b \frac{\phi^{k+1}}{|\nabla \phi^k|_\delta} \xi \, dx - \int_{\Omega} b \frac{\phi^k}{|\nabla \phi^k|_\delta} \xi \, dx + \tau \int_{\Omega} D\gamma\left(\frac{\nabla \phi^k}{|\nabla \phi^k|_\delta}\right) \cdot \nabla \xi \, dx \\
&\quad + \tau \lambda \int_{\Omega} |\nabla \phi^k|_\delta^{-1} \gamma\left(\frac{\nabla \phi^k}{|\nabla \phi^k|_\delta}\right) \nabla(\phi^{k+1} - \phi^k) \cdot \nabla \xi \, dx \\
&\quad + \tau \frac{\epsilon^2}{2} \int_{\Omega} \frac{(\omega^k)^2}{|\nabla \phi^k|_\delta^3} \nabla \phi^{k+1} \cdot \nabla \xi \, dx \\
&\quad + \tau \epsilon^2 \int_{\Omega} \frac{\nabla \omega^{k+1}}{|\nabla \phi^k|_\delta} \cdot \nabla \xi \, dx - \tau \epsilon^2 \int_{\Omega} \frac{(I - P_\Gamma^k) \nabla \omega^k}{|\nabla \phi^k|_\delta} \cdot \nabla \xi \, dx \\
&\quad + \tau \int_{\Omega} \mu^{k+1} \xi \, dx
\end{aligned} \tag{5.23}$$

$$0 = \int_{\Omega} \frac{\omega^{k+1}}{|\nabla \phi^k|_\delta} \zeta \, dx - \int_{\Omega} \frac{\nabla \phi^{k+1}}{|\nabla \phi^k|_\delta} \cdot \nabla \zeta \, dx \tag{5.24}$$

for all $\eta, \xi, \zeta \in \mathcal{V}^h$. With the system matrices

$$\begin{aligned}
M_1 &:= M[1], & L_2 &:= L[|\nabla \phi^k|_\delta^{-1} \gamma\left(\frac{\nabla \phi^k}{|\nabla \phi^k|_\delta}\right)], \\
M_2 &:= M[c |\nabla \phi^k|_\delta], & L_3 &:= L[(\omega^k)^2 |\nabla \phi^k|_\delta^{-3}], \\
M_3 &:= M[b |\nabla \phi^k|_\delta^{-1}], & L_4 &:= L[|\nabla \phi^k|_\delta^{-1}], \\
M_4 &:= M[|\nabla \phi^k|_\delta^{-1}], & L_5 &:= L[(I - P_\Gamma^k) |\nabla \phi^k|_\delta^{-1}], \\
L_1 &:= L[m |\nabla \phi^k|_\delta P_\Gamma^k], & R_1 &:= \left(\int_{\Omega} D\gamma\left(\frac{\nabla \phi^k}{|\nabla \phi^k|_\delta}\right) \cdot \nabla \varphi_i \, dx \right)_i
\end{aligned}$$

and the linear expansions

$$\begin{aligned}\phi^{k+1} &= \sum_{i=1}^N \bar{\phi}_i^{k+1} \varphi_i, \\ \mu^{k+1} &= \sum_{i=1}^N \bar{\mu}_i^{k+1} \varphi_i, \\ \omega^{k+1} &= \sum_{i=1}^N \bar{\omega}_i^{k+1} \varphi_i,\end{aligned}$$

the linear system resulting from (5.22)-(5.23) and which has to be solved in timestep $k+1$ reads

$$\begin{pmatrix} M_1 & -\tau M_2 - \tau L_1 & 0 \\ M_3 + \tau \lambda L_2 + \tau \frac{\epsilon^2}{2} L_3 & \tau M_1 & \tau \epsilon^2 L_4 \\ -L_4 & 0 & M_4 \end{pmatrix} \begin{pmatrix} \bar{\phi}^{k+1} \\ \bar{\mu}^{k+1} \\ \bar{\omega}^{k+1} \end{pmatrix} = \begin{pmatrix} M_1 \bar{\phi}^k \\ M_3 \bar{\phi}^k + \tau \lambda L_2 \bar{\phi}^k + \tau \epsilon^2 L_5 \bar{\omega}^k - \tau R_1 \\ 0 \end{pmatrix}.$$

Again, we use a Schur complement approach to solve the system, which is now applied to a system of three equations and gives

$$\begin{aligned} &\left(M_1 + (M_2 + L_1) M_1^{-1} (M_3 + \tau \lambda L_2 + \tau \frac{\epsilon^2}{2} L_3 + \tau \epsilon^2 L_4 M_4^{-1} L_4) \right) \bar{\phi}^{k+1} = \\ &M_1 \bar{\phi}^k + (M_2 + L_1) M_1^{-1} (M_3 \bar{\phi}^k + \tau \lambda L_2 \bar{\phi}^k + \tau \epsilon^2 L_5 \bar{\omega}^k - \tau R_1). \end{aligned}$$

The weighted curvature term $\bar{\omega}^k$ is calculated in a preprocessing step by $\bar{\omega}^k = M_4^{-1} L_4 \bar{\phi}^k$ in each timestep. The inverse matrices M_1^{-1} and M_4^{-1} are approximated with mass lumping. The non-symmetric linear system is solved with the Krylov-subspace method GMRES.

5.5 Energy dissipation and volume conservation

Energy dissipation and volume conservation for the curvature regularized versions of mean curvature flow, surface diffusion and the kinetic model follow with the same argumentation as in section 3.1, 3.2 and 3.3 applied to the energy functional (5.3) and its variational derivative (5.4).

5.6 Numerical results

In all numerical examples the non-convex anisotropy function (5.2) is used. If not stated otherwise, we choose $a = 1.0$ for the parameter controlling the strength of the anisotropy, and $\epsilon = 0.1$ for the curvature regularization parameter. For curvature regularized mean curvature flow the coefficient $c = 1.0$ is used, and for curvature regularized surface diffusion the mobility coefficient $m = 1.0$. In the kinetic model with curvature regularization we restrict to surface diffusion with kinetics, and choose the parameters $m = 1.0$ and $b = 1.0$. In all our numerical examples, we use the parameter $\lambda = 1.0$ in the semi-implicit discretization scheme of the weighted mean curvature term.

Closed curves and surfaces evolve towards the wulffshape of the anisotropy function γ , changed to rounded corners and edges on a length of the regularization parameter ϵ . For the 2D situation the wulffshape of γ is plotted in figure 5.2. If we smear out the corners on the length scale ϵ , we obtain the shape, closed curves asymptotically evolve to. We notice, that for our choice of parameter ($a = 1.0$), the asymptotical shape does not reveal completely flat areas. The lines connecting the rounded corners are slightly curved. But if we chose very large values

for the anisotropy parameter, $a \rightarrow \infty$, nearly all orientations would be in the range of missing orientations, and the asymptotical shape would have facets (flat lines).

For non-closed curves and surfaces the evolving shape develops facets separated by rounded corners and edges. In the case of curves, we have two, and in the case of surfaces we have four characteristic facet orientations for our four-fold anisotropy. The facet orientations are given through the anisotropy function and are the orientations at the boundary from allowed to missing orientations and vice versa, which in our 2D example are the orientations at the self intersection points in the polar plot of $D\gamma$, see figure 5.2. The characteristic facet orientations, or facet angles in 2D, can be determined by calculating these self intersection points.

Before presenting our numerical results, we comment on the choice of the grid and timestep size in the simulations. First the spatial grid size h is connected to the regularization parameter ϵ as $h \sim \epsilon$, since ϵ is the length scale on which the rounding of the corners in the wulffshape happens, which should be resolved by the grid. And second, the time step τ is chosen as

$$\begin{aligned} \tau &\sim \frac{h^4}{\epsilon^2} \sim h^2 && \text{mean curvature,} \\ \tau &\sim \frac{h^6}{\epsilon^2} \sim h^4 && \text{surface diffusion.} \end{aligned}$$

5.6.1 Mean curvature flow

Closed curves and surfaces. We start with the evolution of a circle and demonstrate the evolution towards the wulffshape. Figure 5.5 shows the evolution. For the unstable orientations at $\theta = 0, \pi/2, \pi, 3\pi/2$ oscillations can be observed, which lead to a local hill-valley structure, which subsequently coarsens and forms the final rounded corner. The shape at $t = 0.035$ is not a steady state. The evolution law is not volume conserving and the curve continues to shrink in time. However, the shape does not change after $t = 0.035$.

As a second example, we have a look at the three-dimensional counterpart, a sphere, and its development towards the wulffshape. Figure 5.6 first shows the evolution of the sphere towards the wulffshape and then the shrinking of the closed surface.

Next, we consider the evolution of a cube in figure 5.7. The regularization parameter is chosen smaller than in the last example. Starting at the edges of the cube the closed surface locally adopts to the wulffshape. A hill-valley structure develops on each face of the cube, which then coarsens from the outer to the inner part until the wulffshape is reached, followed by the shrinking process. Looking at the parameters, a comparably small timestep is chosen with respect to the grid size h and the regularization parameter ϵ , which allows the tracking of the fast evolution of the surface.

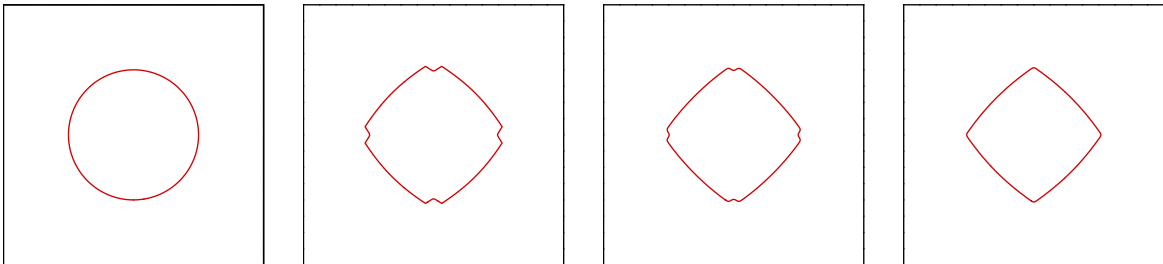


Figure 5.5: Evolution of closed curve to wulffshape under reg. MCF. $[0, 4] \times [0, 4]$ -grid, $h = 0.015625$, $a = 3.0$, $\epsilon = 0.05$, $\tau = 10^{-5}$. From left to right: zero level set at time $t = 0.0, 0.01, 0.025, 0.035$.

Non-closed curves and surfaces. Next, we deal with an interface, whose shape is not a graph at $t = 0$. Figure 5.8 shows the evolution at several time instants. Oscillations can be observed on the flat parts with orientation $\theta = 0$. The remaining parts develop towards a shape with rounded corners connected by nearly straight segments ("facets") (top row of figure 5.8). Due to the periodic boundary conditions, this is not the energy minimizing shape. The surface energy can further be reduced by decreasing the number of rounded corners and the overall curve length, which leads to the final steady state (bottom row of figure 5.8). The numerically measured facet angle at $t = 1.0$ is 26.6 degrees, while the predicted facet angle is 28.8 degrees.

We now deal with a setting, which is close to the described application of thermal annealing and the formation of a hill-valley structure. For these simulations it is useful to consider a linear stability analysis for the orientation $\theta = 0$, see e.g. [25]. Provided the stiffness $\tilde{\gamma}(0) = \gamma(0) + \gamma''(0)$ is negative, the orientation $\theta = 0$ is unstable with most unstable wavelength λ_{max} given by

$$\lambda_{max} = \frac{2\pi\sqrt{2}\epsilon}{\sqrt{|\tilde{\gamma}(0)|}} \quad \text{with} \quad |\tilde{\gamma}(0)| = |1 - 3a|.$$

Choosing $\epsilon = 0.1$, $a = 1.0$ yields $\lambda_{max} \approx 0.63$. As depicted in figure 5.9, a randomly perturbed horizontal line ($\theta = 0$) develops a hill-valley pattern with wavelength $\lambda = 4/6 \approx \lambda_{max}$. After this initial stage, faceting and subsequent coarsening takes place. The numerically obtained facet angle at $t = 0.3$ is 26.1 degrees, measured at the highest kink, which is close to the predicted facet angle (28.2 degrees).

In figure 5.10 the initial curve is a superposition of sine functions. Figure 5.10 shows its evolution. The numerically measured facet angle of the final shape at $t = 0.9$ is 23.4 degrees and agrees very well with the predicted facet angle of 24.1 degrees.

We now turn to a three-dimensional setting and simulate the spinodal decomposition of a randomly perturbed initially flat surface into a hill-valley structure and its subsequent coarsening. Figure 5.11 shows the evolution of the zero level set at various times. At a first stage a hill-valley structure emerges (spinodal decomposition). After the formation of facets and rounded corners and edges, coarsening starts to take place.

5.6.2 Surface diffusion

Closed curves and surfaces. We again start with a closed curve. Figure 5.12 shows the evolution of a circle towards the wulffshape. The volume is conserved. In contrast to the curvature regularized mean curvature flow problem, oscillations do not occur for the chosen parameter, since the most unstable wavelength is too large.

The evolution of the sphere to the wulffshape is depicted in figure 5.13. In difference to curvature regularized mean curvature flow, we see here the volume conserving behavior.

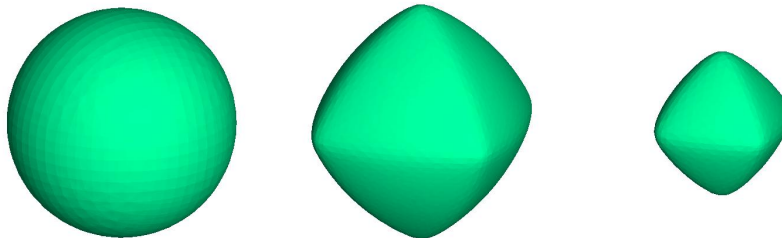


Figure 5.6: Evolution of closed surface to wulffshape under reg. MCF. $[0, 4] \times [0, 4] \times [0, 4]$ -grid, $h = 0.0625$, $\tau = 10^{-4}$, reinitialization every 50th time step. From left to right: zero level set at time $t = 0.0, 0.04, 0.16$.

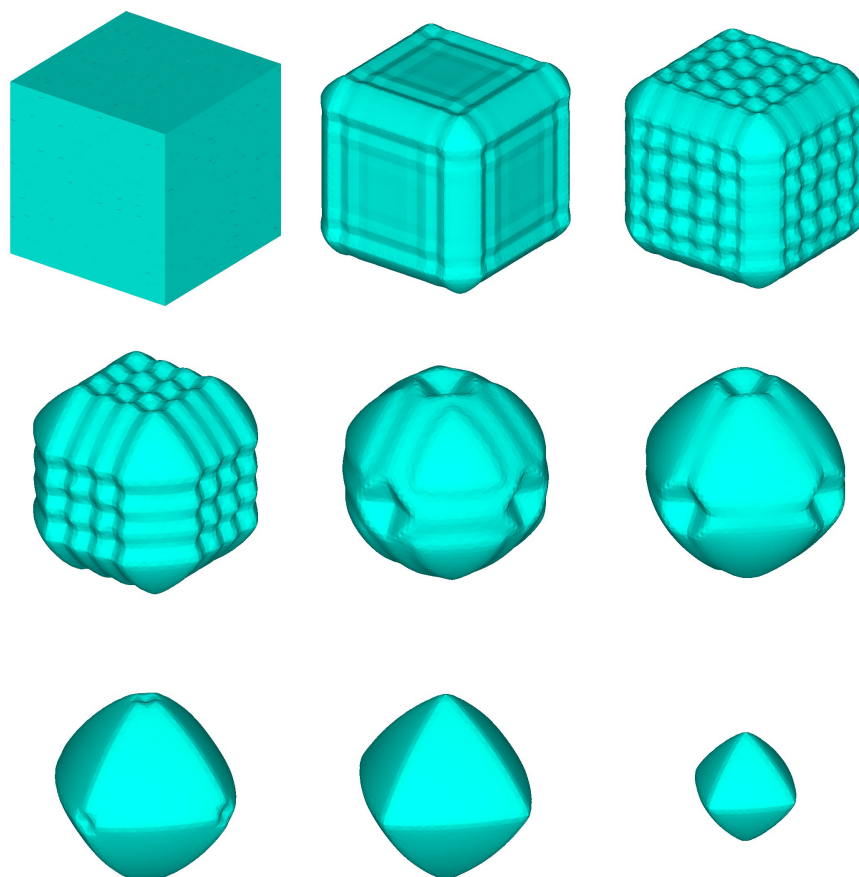


Figure 5.7: Evolution of closed surface to wulffshape under reg. MCF. $[0, 4] \times [0, 4] \times [0, 4]$ -grid, $h = 0.05$, $\epsilon = 0.07$, timestep $\Delta t = 10^{-4}$. From top left to bottom right: $t = 0.0, 0.004, 0.008, 0.02, t = 0.04, 0.05, 0.08, 0.09, 0.15$.

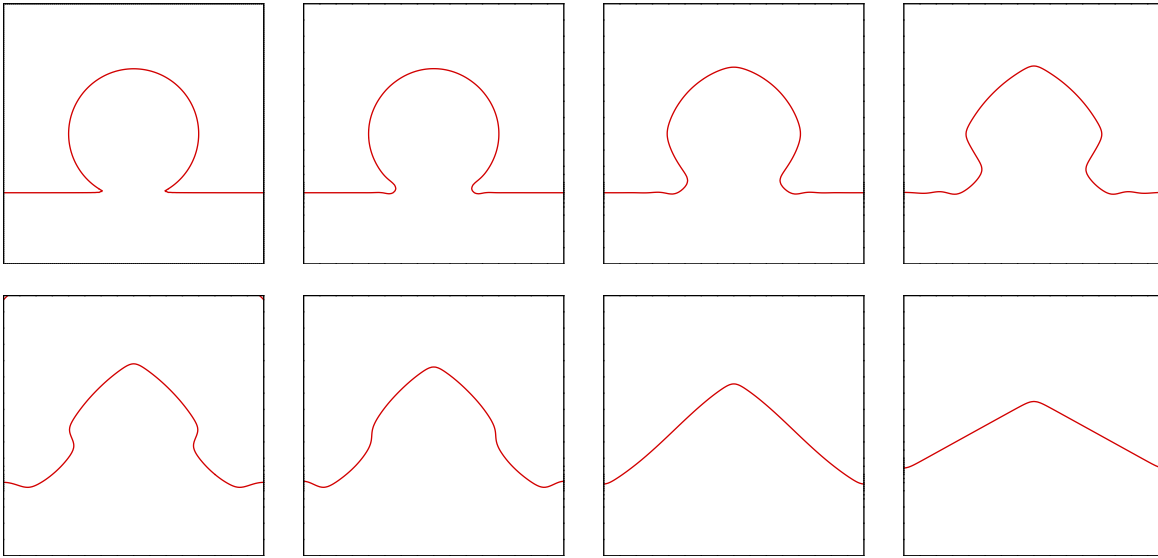


Figure 5.8: Faceting of zero level set under reg. MCF. $[0, 4] \times [0, 4]$ -grid, $h = 0.03125$, $\tau = 10^{-5}$, reinitialization every 10th time step. From top left to bottom right: zero level set at time $t = 0.0, 0.001, 0.01, 0.03, 0.08, 0.1, 0.2, 1.0$.

Figure 5.14 shows the evolution of a cube towards the wulffshape. As under curvature regularized mean curvature flow a hill-valley structure develops on the faces of the circle, which coarsens to the wulffshape.

Non-closed curves and surfaces. Figure 5.15 shows the evolution of an omega-like shape at various time steps. The oscillations on the flat parts are much more pronounced than in the case of curvature regularized anisotropic mean curvature flow. As expected for the higher order equation the time scale at which these oscillations occur and form a local hill-valley structure is much smaller than in the previous section. However, the formation of the predicted facet angle of the final steady state needs much more time as compared to curvature regularized mean curvature flow.

Again, we compute the most unstable wavelength λ_{max} from a linear stability analysis for $\theta = 0$.

$$\lambda_{max} = 2\pi\epsilon\sqrt{\frac{3}{2|\tilde{\gamma}(0)|}} \quad \text{with} \quad |\tilde{\gamma}(0)| = |1 - 3a|$$

Choosing $\epsilon = 0.1$, $a = 1.0$ yields $\lambda_{max} \approx 0.544$. In figure 5.16 we observe the spinodal decomposition of a randomly perturbed horizontal line into a hill-valley pattern with wavelength $\lambda = 4/7 \approx \lambda_{max}$ and subsequent faceting and coarsening.

Figure 5.17 shows the evolution of a superposition of sine functions. The damping of the high frequencies is much faster if compared with curvature regularized mean curvature flow.

We now turn to a three-dimensional setting and simulate the spinodal decomposition of a randomly perturbed initially flat surface into a hill-valley structure and its subsequent coarsening. Figure 5.18 shows the evolution of the zero level set at various times. The formation of facets and the rounded corners and edges can clearly be observed. After the evolution of the right facet angles, coarsening starts. Again this is qualitatively similar to the case of curvature regularized anisotropic mean curvature flow but happens on a smaller time scale.

Volume conservation and energy dissipation. Figure 5.19 shows the volume conserving and energy dissipating behavior for the example in figure 5.15. The volume is preserved within a tolerance of 4%.

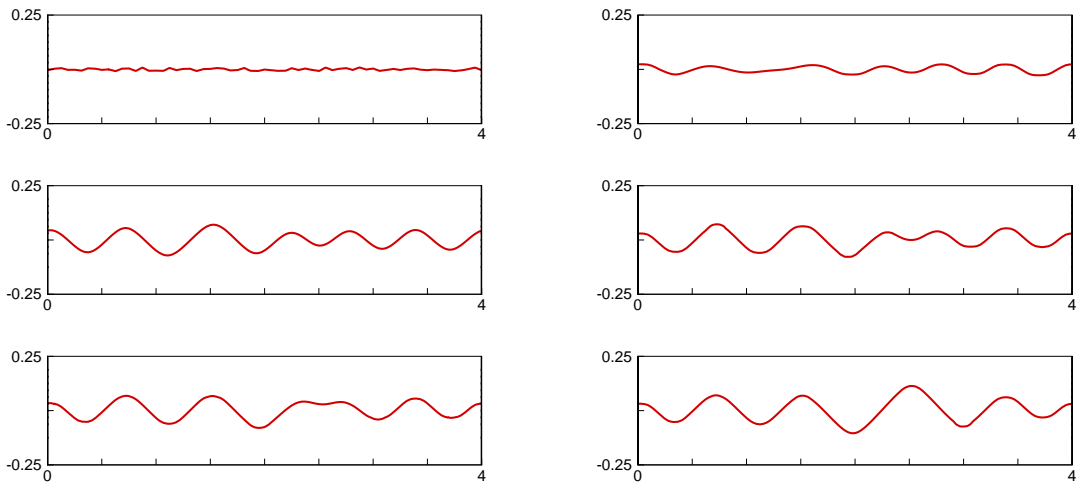


Figure 5.9: Faceting and coarsening of zero level set under reg. MCF. $[0, 4] \times [0, 2]$ -grid, $h = 0.03125$, $\tau = 10^{-6}$. From top left to bottom right: zero level set at time $t = 0.0, 0.035, 0.09, 0.16, 0.2, 0.3$.

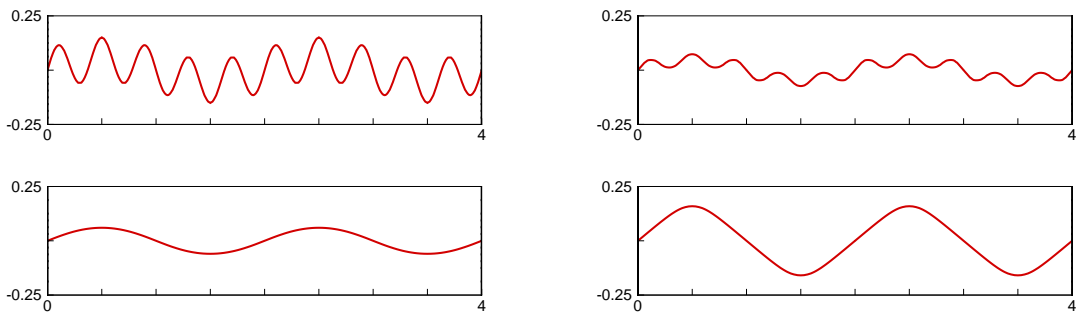


Figure 5.10: Faceting of zero level set under reg. MCF. $[0, 4] \times [0, 2]$ -grid, $h = 0.03125$, $a = \frac{2}{3}$, $\tau = 10^{-6}$. From top left to bottom right: zero level set at time $t = 0.0, 0.003, 0.05, 0.9$.

5.6.3 Kinetic model

In the numerical examples for the kinetic model with curvature regularization, we concentrate on a comparison of surface diffusion ($m = 1$) and surface diffusion with kinetics ($m = 1, b = 1$).

Closed curves and surfaces. Figure 5.20 shows the evolution of a circle towards the wulffshape. It can be observed, that the time scale necessary to reach the equilibrium shape is different for surface diffusion and surface diffusion with kinetics. Under the presence of the kinetic term the evolution slows down. In both cases the unstable orientations for $0, \pi/2, \pi$ and $3\pi/2$ lead to the formation of wrinkles with the allowed orientations, which subsequently coarsen.

Figure 5.21 confirms the observation on different time scales in the evolution for the same example in three dimensions. Here the initial shape is a sphere. The wrinkling is not observed in this configuration, even for smaller grid sizes.

Non-closed curves. The second example shows the evolution of a perturbed straight line. The perturbation is a superposition of sines. The high frequencies are damped in both cases and a hill-valley pattern forms. After this initial stage, faceting and subsequent coarsening takes place, see figure 5.22. The difference between the two cases is again in the time scale. The damping is much faster for surface diffusion. The same is true for the coarsening process.

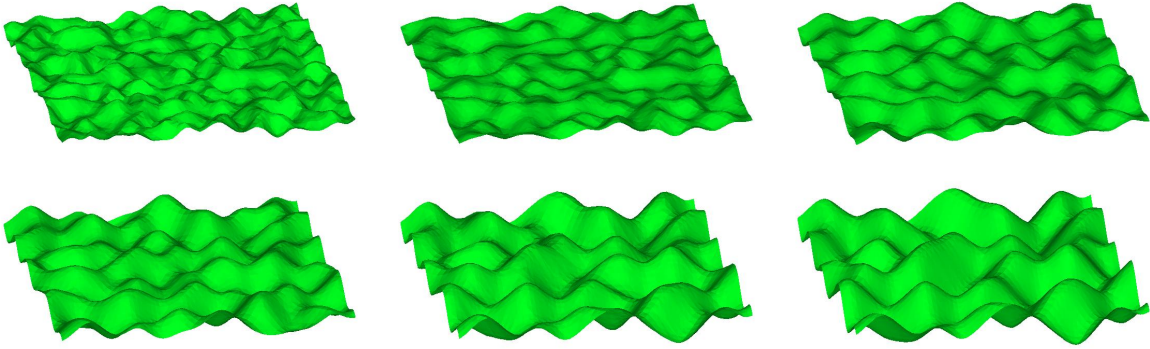


Figure 5.11: Faceting and coarsening of zero level set under reg. MCF. $[0, 4] \times [0, 4] \times [0, 1]$ -grid, $h = 0.0625$, $\tau = 10^{-5}$. From top left to bottom right: zero level set at time $t = 0.001, 0.004, 0.02, 0.04, 0.08, 0.12$.

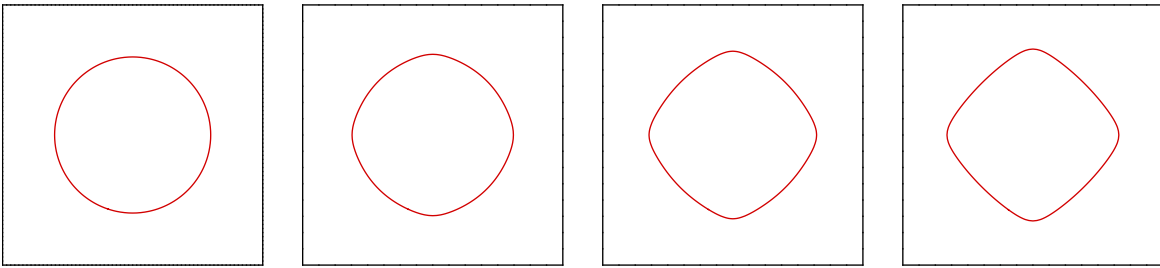


Figure 5.12: Evolution of closed curve to wulffshape under reg. SD. $[0, 4] \times [0, 4]$ -grid, $h = 0.0625$, $\tau = 10^{-6}$, $\epsilon = 0.2$, reinitialization every 50th time step. From left to right: zero level set at time $t = 0.0, 0.001, 0.003, 0.01$.

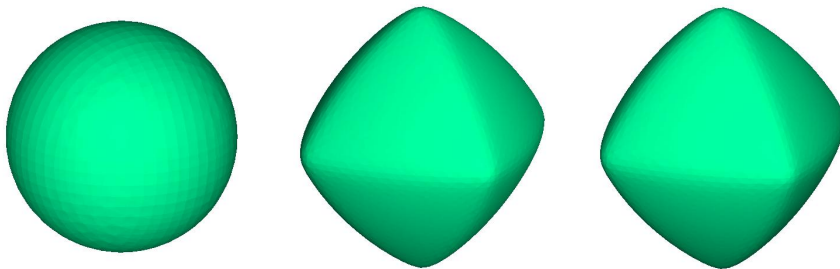


Figure 5.13: Evolution of closed surface to wulffshape under reg. SD. $[0, 4] \times [0, 4] \times [0, 4]$ -grid, $h = 0.0625$, $\tau = 10^{-6}$, reinitialization every 50th timestep. From left to right: zero level set at time $t = 0.0, 0.001, 0.007$.

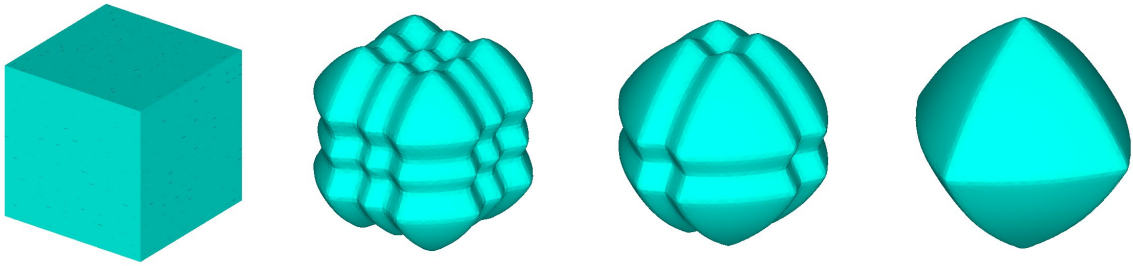


Figure 5.14: Evolution of closed surface to wulffshape under reg. SD. $[0, 4] \times [0, 4] \times [0, 4]$ -grid, grid size $h = 0.05$, timestep $\Delta t = 10^{-6}$. From left to right: $t = 0.0, 0.001, 0.005, 0.01$.

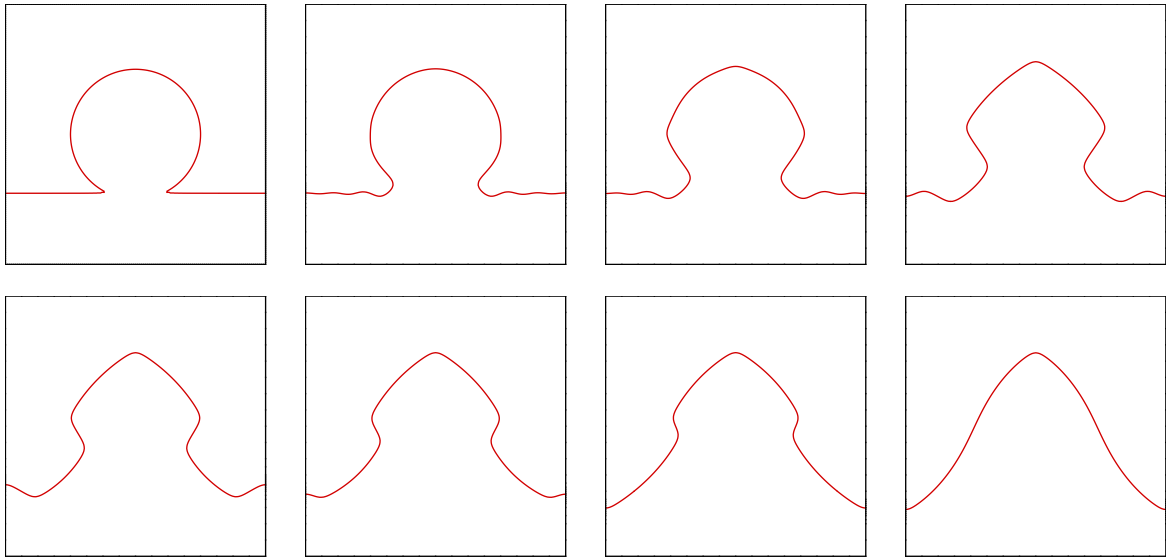


Figure 5.15: Faceting of zero level set under reg. SD. $[0, 4] \times [0, 4]$ -grid, $h = 0.03125$, $\tau = 5 \times 10^{-8}$, reinitialization every 100th timestep. From top left to bottom right: zero level set at time $t = 0.0, 0.0001, 0.0005, 0.01, 0.02, 0.03, 0.058$.

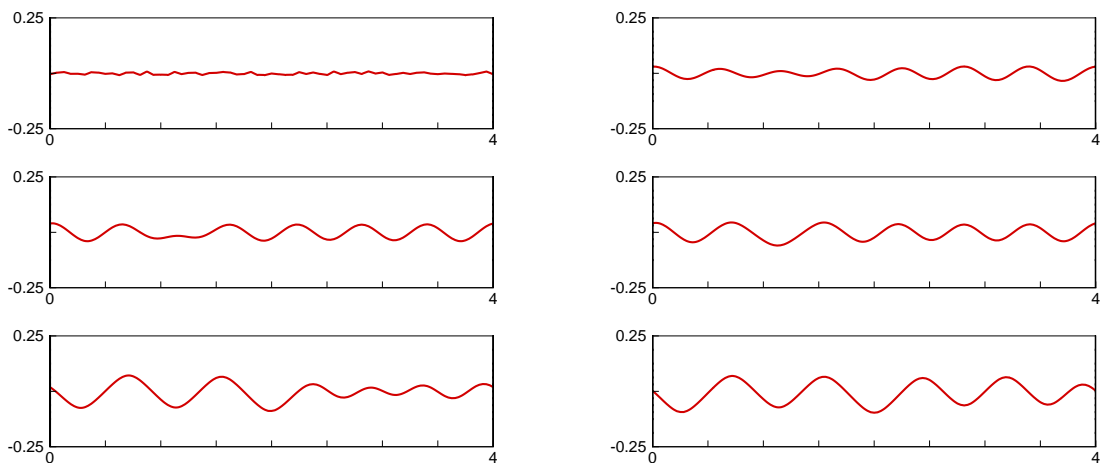


Figure 5.16: Faceting and coarsening of zero level set under reg. SD. $[0, 4] \times [0, 2]$ -grid, $h = 0.03125$, $\tau = 10^{-7}$, reinitialization every 50th time step. From top left to bottom right: zero level set at time $t = 0.0, 0.0004, 0.0017, 0.002, 0.016, 0.018$.

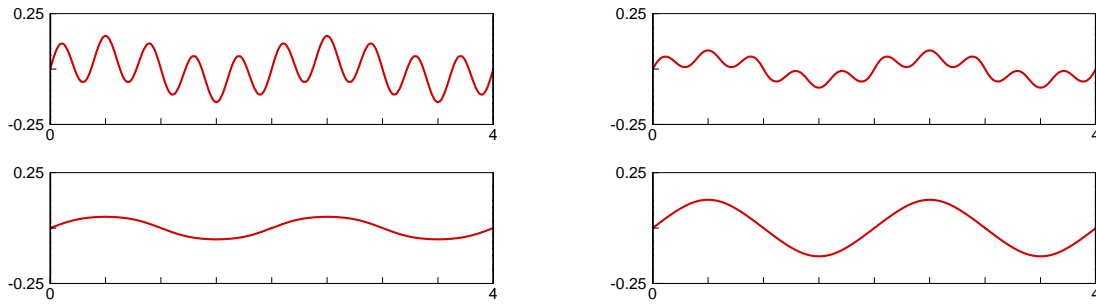


Figure 5.17: Faceting of zero level set under reg. SD. $[0, 4] \times [0, 2]$ -grid, $h = 0.03125$, $a = \frac{2}{3}$, $\epsilon = 0.2$, $\tau = 10^{-8}$ until $t = 10^{-5}$, $\tau = 10^{-7}$ until $t = 2 \times 10^{-5}$, then $\tau = 10^{-6}$, reinitialization every 50th timestep. From top left to bottom right: zero level set at time $t = 0.0$, 5×10^{-6} , 2×10^{-5} , 0.081 .

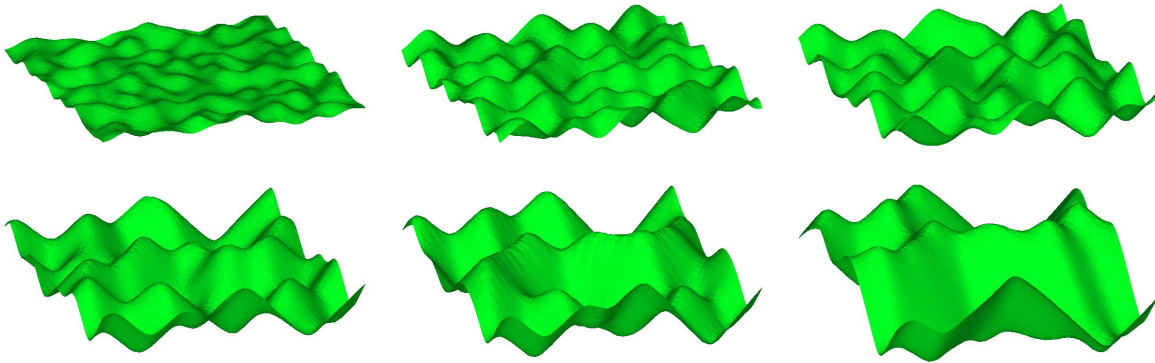


Figure 5.18: Faceting and coarsening of zero level set under reg. SD. $[0, 4] \times [0, 4] \times [0, 1]$ -grid, $h = 0.0625$, $\tau = 5 \times 10^{-6}$. From top left to bottom right: zero level set at time $t = 0.0001$, 0.002 , 0.006 , 0.012 , 0.016 , 0.035 .

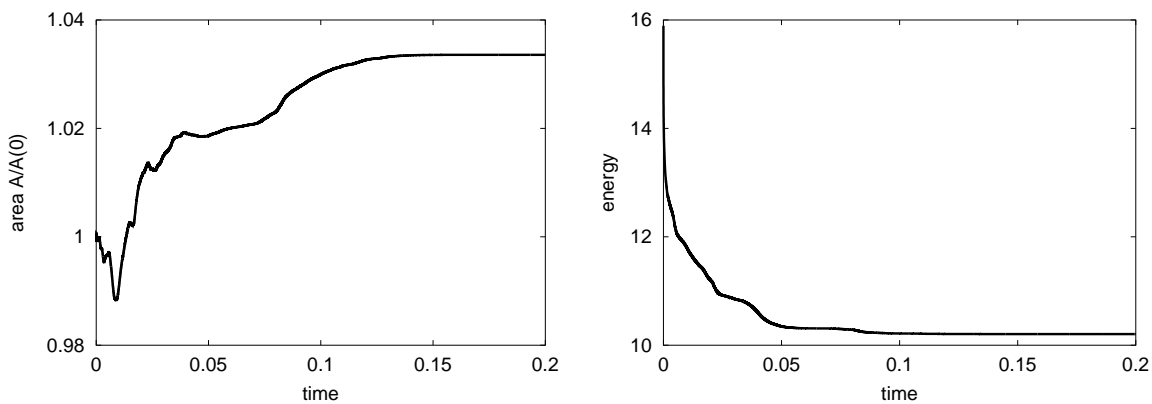


Figure 5.19: Area conservation (left) and energy dissipation (right) for curvature regularized surface diffusion in figure 5.15.

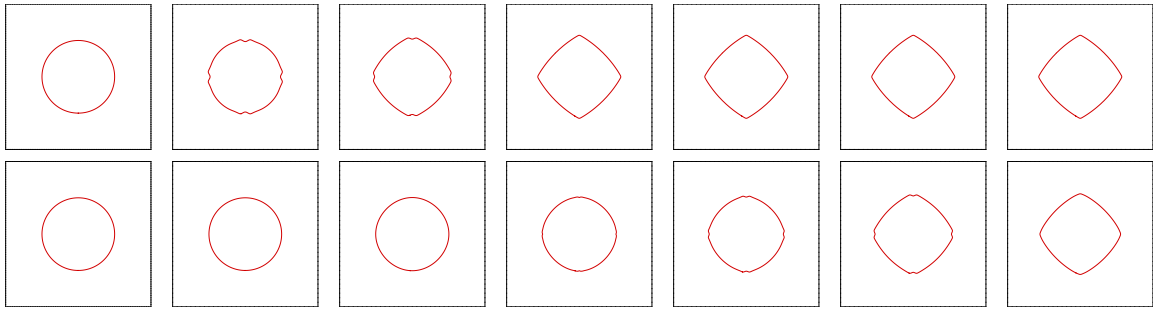


Figure 5.20: 2-D case: (top row) evolution by surface diffusion, (bottom row) evolution by surface diffusion with kinetics. The times from left to right are $t = 0.0, 0.0001, 0.002, 0.005, 0.01, 0.03, 0.042$. For surface diffusion the wulffshape is reached at $t = 0.002$.

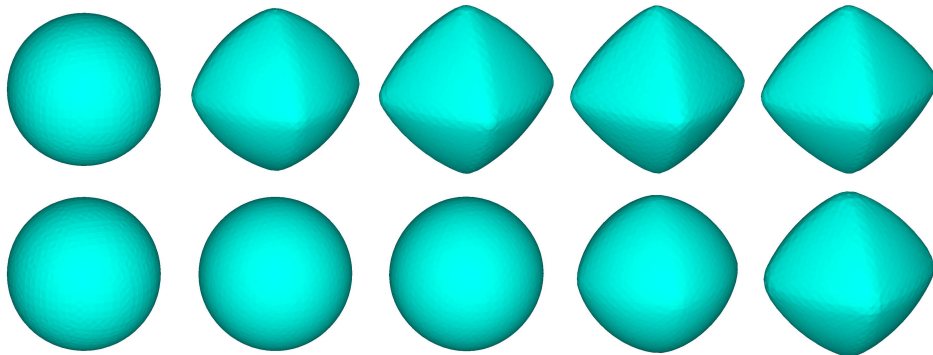


Figure 5.21: 3-D case:(top row) evolution by surface diffusion, (bottom row) evolution by surface diffusion with kinetics. The times from left to right are $t = 0.0, 0.001, 0.01, 0.02, 0.03$. For surface diffusion the wulffshape is reached at $t = 0.01$.

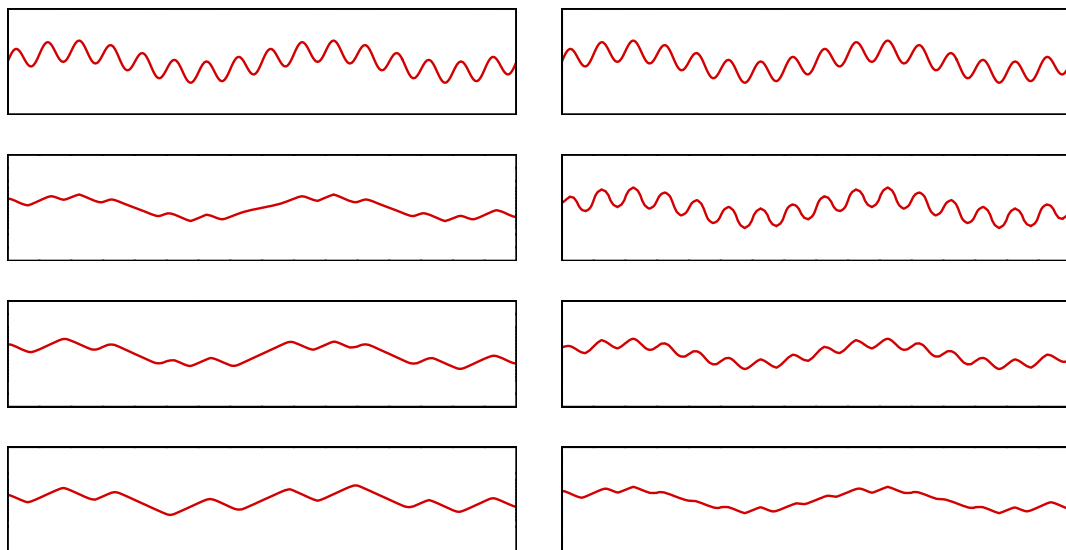


Figure 5.22: (left column) evolution by surface diffusion, (right column) evolution by surface diffusion with kinetics. The times from top to bottom are $t = 0.0, 0.0001, 0.001, 0.01$.

Chapter 6

Adatom model

In the models for thin film growth discussed so far the chemical potential μ is determined only through geometrical terms, such as the mean curvature or the weighted mean curvature of the surface. We now present a model where the chemical potential is described in the more physical understanding in terms of free adatoms. Free adatoms are assumed to play an important role in solid-vapor interfaces. Adatoms are mobile atoms which are not attached to a fixed position on the film surface. They move around on the surface until they attach to surface defects. On the other hand, atoms incorporated in the surface can lower their chemical bonds to the surface and become mobile or even detach from the surface. To account for these adatoms, our model now includes a further component for the description of the evolving surface. In addition to the surface geometry or shape, it describes the density of free adatoms on the surface. We will see that the adatom distribution is related to the surface geometry and its evolution. The adatom model can be considered as a generalization of the kinetic model. We will show that by neglecting the adatom density ($u = 0$), we regain the kinetic model.

The model has been introduced by Fried and Gurtin in [33] within the framework of configurational forces. In [10] the model is analyzed in detail in isotropic situation and numerically solved with a graph formulation. A phase field approximation for the isotropic situation is provided in [54]. In [65] a variational derivation from an energy functional is presented. In this work, we follow the approach in [65] for the description of the model.

The dependency on free adatoms is reflected in the surface free energy density γ , which now also depends on the adatom density u . We employ an energy density function of the form

$$\gamma(\nu, u) = \gamma_1(\nu) + \gamma_2(u),$$

where γ_1 is the orientation dependent anisotropy function which determined in the previous chapters the surface free energy density. This form of $\gamma(\nu, u)$ splits the dependency on ν and u and treats the adatom density isotropically. The actual function γ is not known for any material. So its form could be much more complicated, which would lead to a different model. Our choice of γ leads to the model presented in [33]. The energy functional then reads

$$E[\Gamma, u] = \int_{\Gamma} \gamma(\nu, u) dA. \quad (6.1)$$

Using the principles of local mass balance and thermodynamic consistency, the following equations are derived in [65] by a variational approach for this energy functional

$$u_t + V + uHV = \nabla_{\Gamma} \cdot \left(m \nabla_{\Gamma} \frac{\delta E}{\delta u} \right) - c \frac{\delta E}{\delta u} \quad (6.2)$$

$$bV + \frac{\delta E}{\delta \Gamma} - (1 + uH) \frac{\delta E}{\delta u} = 0. \quad (6.3)$$

With

$$\frac{\delta E}{\delta u} = \partial_u \gamma = \mu \quad (6.4)$$

$$\frac{\delta E}{\delta \Gamma} = H_{\gamma_1} + \gamma_2 H \quad (6.5)$$

this gives the equations of the adatom model

$$u_t + V + uHV = \nabla_{\Gamma} \cdot (m \nabla_{\Gamma} \mu) - c\mu \quad (6.6)$$

$$\mu = \partial_u \gamma \quad (6.7)$$

$$bV + H_{\gamma_1} + \gamma_2 H - \mu - uH\mu = 0 \quad (6.8)$$

with the coefficients m , c and b as in the kinetic model in section 3.3. Equation (6.7) defines the chemical potential in terms of the adatom density. Considering only equation (6.8) in steady state ($V = 0$), the influence of the surface geometry on the adatom density becomes clear. If we neglect the adatom density in equations (6.6) and (6.8) by setting $u = 0$ and use the surface free energy $\gamma = \gamma_1$, we obtain the equations of the kinetic model in section 4.4. The chemical potential in this case is interpreted as $\mu = bV + H_{\gamma}$.

Again, we use a curvature regularization term in the energy functional, which leads to smeared out corners and edges on the small length scale ϵ . The energy functional in its regularized version reads

$$E[\Gamma, u] = \int_{\Gamma} \gamma(\nu, u) + \epsilon^2 \frac{1}{2} H^2 dA.$$

With

$$\begin{aligned} \frac{\delta E}{\delta u} &= \mu, \\ \frac{\delta E}{\delta \Gamma} &= H_{\gamma_1} + \gamma_2 H - \epsilon^2 \left(\Delta_{\Gamma} H + H (\|S\|^2 - \frac{1}{2} H^2) \right), \end{aligned}$$

and the equations (6.2) and (6.3), the model in its regularized form is given through

$$u_t + V + uVH = \nabla_{\Gamma} \cdot (m \nabla_{\Gamma} \mu) - c\mu \quad (6.9)$$

$$\mu = \partial_u \gamma \quad (6.10)$$

$$bV + H_{\gamma_1} + \gamma_2 H - \epsilon^2 \left(\Delta_{\Gamma} H + H (\|S\|^2 - \frac{1}{2} H^2) \right) = \mu + uH\mu. \quad (6.11)$$

In [10] the author shows in isotropic situation that the energy (6.1) can become non-convex for large adatom densities and rough surfaces, and states that this is in difference to the energy (4.1) used when neglecting free adatoms, where the energy is always convex in isotropic and weak anisotropic situation (convex anisotropy function). Furthermore, the author establishes a stability condition which in isotropic situation ensures stability if $1 + \gamma_2(u) - \mu \geq 0$. We therefore state, that the regularization here might not only be of use in strong anisotropic situation, where it serves to produce rounded corners and edges and to stabilize backwards parabolic equations, but might also stabilize the equations in weak anisotropic situation. Here the risk to get non-convex energies is probably higher than in isotropic situation. If the mean curvature H is much larger than the weighted mean curvature H_{γ_1} , the term $H_{\gamma_1} + \gamma_2 H - uH\mu$ may become negative and the equations backwards parabolic.

Equations (6.9)-(6.11) represent a diffusion equation for the adatom density on an evolving surface. Theoretical results for such problems are rare and also numerical methods are much less developed than for equations defined in \mathbb{R}^d . Only recently various numerical approaches are introduced. In [28] a direct approach by parametric finite elements is proposed to solve a

diffusion equation on an evolving interface. Therein, the evolution of the surface is given by a time dependent function independent from the surface geometry and the diffusing material. For complicated movements severe problems to maintain the regularity of the surface mesh have to be overcome. These problems can be avoided by using an implicit representation of the surface through a level set function or phase-field approximation. In [1] and [73] diffusion equations on evolving surfaces represented by a level set representation are treated numerically. However, both approaches are restricted to evolving curves.

In the rest of this chapter, we present the numerical treatment of equations (6.9)-(6.11) with level sets. The variable μ in equations (6.9) and (6.11) is replaced by an explicit choice of γ_2 in (6.10), which results in a coupled system of two equations, where the surface and the adatom density are the unknowns. We apply an operator splitting approach. In each timestep, equations (6.9) and (6.11) are solved separately. Equation (6.9) is interpreted as diffusion equation for the adatom density u for a given surface Γ , and equation (6.11) as evolution equation for the surface Γ for given u and μ . Several numerical examples for adatom diffusion on terrace or step boundaries (2D) and for adatom diffusion on film surfaces (3D) will be given. We present examples in isotropic and strong anisotropic situation.

6.1 Level set formulation

We derive a level set formulation of equations (6.6) and (6.8) in divergence form, which allows an easy calculation of the weak formulation of the equations. With the weak formulation of the regularization term provided in section 5.2, we obtain the weak formulation of the adatom model in its curvature regularized version, which is equations (6.9) and (6.11), in the next section.

Using the level set formulation of the normal velocity, (weighted) mean curvature and surface laplacian in (2.12), (2.14), (4.3) and (2.16), and multiplying the first equation with $|\nabla\phi|$ provides for (6.6) and (6.8) the equations

$$\begin{aligned} u_t|\nabla\phi| - \phi_t - u(\nabla \cdot \frac{\nabla\phi}{|\nabla\phi|})\phi_t - \nabla \cdot (m|\nabla\phi|P_\Gamma\nabla\mu) + c\mu|\nabla\phi| &= 0 \\ -b\frac{\phi_t}{|\nabla\phi|} + \nabla \cdot D\gamma_1(\nabla\phi) + \gamma_2(u)\nabla \cdot \frac{\nabla\phi}{|\nabla\phi|} - \mu - u(\nabla \cdot \frac{\nabla\phi}{|\nabla\phi|})\mu &= 0. \end{aligned}$$

Several terms are not in divergence form. We rewrite these terms through

$$\begin{aligned} u\phi_t\nabla \cdot \frac{\nabla\phi}{|\nabla\phi|} &= \nabla \cdot (u\phi_t\frac{\nabla\phi}{|\nabla\phi|}) - \frac{\nabla\phi}{|\nabla\phi|} \cdot (\phi_t\nabla u + u\nabla\phi_t) \\ \gamma_2(u)\nabla \cdot \frac{\nabla\phi}{|\nabla\phi|} &= \nabla \cdot (\gamma_2(u)\frac{\nabla\phi}{|\nabla\phi|}) - \mu\nabla u \cdot \frac{\nabla\phi}{|\nabla\phi|} \\ u\mu\nabla \cdot \frac{\nabla\phi}{|\nabla\phi|} &= \nabla \cdot (u\mu\frac{\nabla\phi}{|\nabla\phi|}) - \frac{\nabla\phi}{|\nabla\phi|} \cdot (\mu\nabla u + u\nabla\mu), \end{aligned}$$

where we used $\nabla(\gamma_2(u)) = \gamma_2'(u)\nabla u = \mu\nabla u$ in the second equation. The level set formulation for equations (6.6) and (6.8) then reads

$$\begin{aligned} 0 &= u_t|\nabla\phi| - \phi_t - \nabla \cdot (u\phi_t\frac{\nabla\phi}{|\nabla\phi|}) + \frac{\nabla\phi}{|\nabla\phi|} \cdot (\phi_t\nabla u + u\nabla\phi_t) \\ &\quad - \nabla \cdot (m|\nabla\phi|P_\Gamma\nabla\mu) + c\mu|\nabla\phi| \end{aligned} \tag{6.12}$$

$$\begin{aligned} 0 &= -b\frac{\phi_t}{|\nabla\phi|} + \nabla \cdot D\gamma_1(\nabla\phi) + \nabla \cdot (\gamma_2(u)\frac{\nabla\phi}{|\nabla\phi|}) \\ &\quad - \mu - \nabla \cdot (u\mu\frac{\nabla\phi}{|\nabla\phi|}) + u\frac{\nabla\phi}{|\nabla\phi|} \cdot \nabla\mu. \end{aligned} \tag{6.13}$$

6.2 Weak formulation and discretization

Because the equations have become quite long, we first derive the weak formulation without the regularization part, and add the regularizing terms afterwards. Multiplying equations (6.12) and (6.13) with test functions and integration by parts gives the weak formulation

$$\begin{aligned}
0 &= \int_{\Omega} |\nabla\phi| u_t \eta \, dx - \int_{\Omega} \phi_t \eta \, dx + \int_{\Omega} u \phi_t \frac{\nabla\phi}{|\nabla\phi|} \cdot \nabla\eta \, dx \\
&\quad + \int_{\Omega} \frac{\nabla\phi}{|\nabla\phi|} \cdot (\phi_t \nabla u + u \nabla\phi_t) \eta \, dx \\
&\quad + \int_{\Omega} m |\nabla\phi| P_{\Gamma} \nabla\mu \cdot \nabla\eta \, dx + \int_{\Omega} c |\nabla\phi| \mu \eta \, dx \\
0 &= \int_{\Omega} b \frac{\phi_t}{|\nabla\phi|} \xi \, dx + \int_{\Omega} D\gamma_1(\nabla\phi) \cdot \nabla\xi \, dx + \int_{\Omega} \gamma_2(u) \frac{\nabla\phi}{|\nabla\phi|} \cdot \nabla\xi \, dx \\
&\quad + \int_{\Omega} \mu \xi \, dx - \int_{\Omega} u \mu \frac{\nabla\phi}{|\nabla\phi|} \cdot \nabla\xi \, dx - \int_{\Omega} u \nabla\mu \cdot \frac{\nabla\phi}{|\nabla\phi|} \xi \, dx
\end{aligned}$$

for all test functions $\eta, \xi \in C_0^\infty(\Omega)$. With the weak formulation of the regularization term $-(\Delta_{\Gamma} H + H(\|S\|^2 - \frac{1}{2}H^2))$ in (5.8) and (5.9), the weak formulation of (6.9) and (6.11) reads

$$\begin{aligned}
0 &= \int_{\Omega} |\nabla\phi| u_t \eta \, dx - \int_{\Omega} \phi_t \eta \, dx + \int_{\Omega} u \phi_t \frac{\nabla\phi}{|\nabla\phi|} \cdot \nabla\eta \, dx \\
&\quad + \int_{\Omega} \frac{\nabla\phi}{|\nabla\phi|} \cdot (\phi_t \nabla u + u \nabla\phi_t) \eta \, dx \\
&\quad + \int_{\Omega} m |\nabla\phi| P_{\Gamma} \nabla\mu \cdot \nabla\eta \, dx + \int_{\Omega} c |\nabla\phi| \mu \eta \, dx \tag{6.14}
\end{aligned}$$

$$\begin{aligned}
0 &= \int_{\Omega} b \frac{\phi_t}{|\nabla\phi|} \xi \, dx + \int_{\Omega} D\gamma_1(\nabla\phi) \cdot \nabla\xi \, dx + \int_{\Omega} \gamma_2(u) \frac{\nabla\phi}{|\nabla\phi|} \cdot \nabla\xi \, dx \\
&\quad + \frac{\epsilon^2}{2} \int_{\Omega} \frac{\omega^2}{|\nabla\phi|^3} \nabla\phi \cdot \nabla\eta \, dx + \epsilon^2 \int_{\Omega} \frac{P_{\Gamma} \nabla\omega}{|\nabla\phi|} \cdot \nabla\eta \, dx \\
&\quad + \int_{\Omega} \mu \xi \, dx - \int_{\Omega} u \mu \frac{\nabla\phi}{|\nabla\phi|} \cdot \nabla\xi \, dx - \int_{\Omega} u \nabla\mu \cdot \frac{\nabla\phi}{|\nabla\phi|} \xi \, dx \tag{6.15}
\end{aligned}$$

$$0 = \int_{\Omega} \frac{\omega}{|\nabla\phi|} \zeta \, dx - \int_{\Omega} \frac{\nabla\phi}{|\nabla\phi|} \cdot \nabla\zeta \, dx. \tag{6.16}$$

for all test functions $\eta, \xi, \zeta \in C_0^\infty(\Omega)$.

We assume that the chemical potential μ depends linearly on the adatom density u . This allows for an implicit treatment of μ in the discretization in terms where μ enters linearly in the equations. The relation between μ and u is given through (6.10). We use the function

$$\gamma_2(u) = \frac{1}{2} \alpha u^2$$

with a positive parameter α , which gives

$$\mu = \partial_u \gamma_2(u) = \alpha u. \tag{6.17}$$

We replace μ by the relation (6.17) in the discretization.

Applying our semi-implicit discretization scheme on equations (6.14)-(6.16) is not straight forward. For example in the operator $\int_{\Omega} u \phi_t \frac{\nabla\phi}{|\nabla\phi|} \cdot \nabla\eta \, dx$ both unknowns ϕ and u are involved and enter linearly in the equations. It is not clear, which unknown to treat implicitly and which one

explicitly. Treating ϕ implicitly whenever possible and only treating u implicitly when ϕ does not occur in the operator or is treated explicitly, would lead to a nearly full explicit treatment of u . In order to obtain a more explicit scheme, we do not solve equations (6.14)-(6.16) as a system of three equations in this situation but apply an operator splitting approach, which first solves (6.15) and (6.16) as equations for the unknown ϕ and then (6.14) as equation for u . We apply our semi-implicit discretization scheme for each part as usual.

With the semi-implicit discretization of the weighted mean curvature term in (4.7) and the discretization of the regularization term in (5.10) and (5.11), the semi-implicit discretization of equations (6.15) and (6.16) reads

$$\begin{aligned}
0 &= \int_{\Omega} b \frac{\phi^{k+1}}{|\nabla \phi^k|_{\delta}} \xi \, dx - \int_{\Omega} b \frac{\phi^k}{|\nabla \phi^k|_{\delta}} \xi \, dx \\
&+ \tau \int_{\Omega} D\gamma_1(\nabla \phi^k) \cdot \nabla \xi \, dx + \tau \lambda \int_{\Omega} \frac{\gamma_1(\frac{\nabla \phi^k}{|\nabla \phi^k|_{\delta}})}{|\nabla \phi^k|_{\delta}} \nabla(\phi^{k+1} - \phi^k) \cdot \nabla \eta \, dx \\
&+ \tau \frac{\epsilon^2}{2} \int_{\Omega} \frac{(\omega^k)^2}{|\nabla \phi^k|_{\delta}^3} \nabla \phi^{k+1} \cdot \nabla \eta \, dx \\
&+ \tau \epsilon^2 \int_{\Omega} \frac{\nabla \omega^{k+1}}{|\nabla \phi^k|_{\delta}} \cdot \nabla \eta \, dx - \tau \epsilon^2 \int_{\Omega} \frac{(I - P_{\Gamma}^k) \nabla \omega^k}{|\nabla \phi^k|_{\delta}} \cdot \nabla \eta \, dx \\
&+ \tau \alpha \int_{\Omega} u^k \xi \, dx - \tau \frac{\alpha}{2} \int_{\Omega} (u^k)^2 \frac{\nabla \phi^{k+1}}{|\nabla \phi^k|_{\delta}} \cdot \nabla \xi \, dx - \tau \alpha \int_{\Omega} u^k \nabla u^k \cdot \frac{\nabla \phi^{k+1}}{|\nabla \phi^k|_{\delta}} \xi \, dx \quad (6.18)
\end{aligned}$$

$$0 = \int_{\Omega} \frac{\omega^{k+1}}{|\nabla \phi^k|_{\delta}} \zeta \, dx - \int_{\Omega} \frac{\nabla \phi^{k+1}}{|\nabla \phi^k|_{\delta}} \cdot \nabla \zeta \, dx \quad (6.19)$$

for all $\xi, \zeta \in \mathcal{V}^h$. And the semi-implicit discretization of equation (6.14) results in

$$\begin{aligned}
0 &= \int_{\Omega} |\nabla \phi^{k+1}|_{\delta} u^{k+1} \eta \, dx - \int_{\Omega} |\nabla \phi^{k+1}|_{\delta} u^k \eta \, dx \\
&- \int_{\Omega} (\phi^{k+1} - \phi^k) \eta \, dx + \int_{\Omega} u^{k+1} (\phi^{k+1} - \phi^k) \frac{\nabla \phi^{k+1}}{|\nabla \phi^{k+1}|_{\delta}} \cdot \nabla \eta \, dx \\
&+ \int_{\Omega} \frac{\nabla \phi^{k+1}}{|\nabla \phi^{k+1}|_{\delta}} \cdot ((\phi^{k+1} - \phi^k) \nabla u^{k+1} + u^{k+1} \nabla(\phi^{k+1} - \phi^k)) \eta \, dx \\
&+ \tau \alpha \int_{\Omega} m |\nabla \phi^{k+1}|_{\delta} P_{\Gamma}^{k+1} \nabla u^{k+1} \cdot \nabla \eta \, dx + \tau \alpha \int_{\Omega} c |\nabla \phi^{k+1}|_{\delta} u^{k+1} \eta \, dx \quad (6.20)
\end{aligned}$$

for all $\eta \in \mathcal{V}^h$. In equations (6.18) and (6.19) the variable ϕ^{k+1} is calculated in dependence on ϕ^k and u^k , and the solution of equation (6.20) provides u^{k+1} in terms of ϕ^{k+1} , ϕ^k and u^k .

In equation (6.20) the adatom density u^k is the approximation of the adatom density at the new interface given through ϕ^{k+1} . The interface moves in normal direction. To ensure that u^k has appropriate values at the new interface, we extend the adatom density in direction normal to the interface at the beginning of each timestep. The extension is calculated by an adaption of our redistancing algorithm described in section 2.4. More details will be given below. Computational experiments showed a significant difference in the results when using the extension of the adatom density or not. The difference has mainly been measured by looking at energy dissipation and volume conservation. So in timestep $k+1$ the following steps are performed:

1. Extend the adatom density u^k normal to the interface Γ given through the level set function ϕ^k .
2. Calculate ω^k with respect to ϕ^k (see below).

3. Calculate ϕ^{k+1} with equations (6.18) and (6.19).
4. Calculate u^{k+1} with equation (6.20).

We finally come to the description of the linear systems resulting from equations (6.18)-(6.20) and their solution. In chapter 3 notations $M[f]$, $L[f]$ and $L[A]$ for mass and stiffness matrices have been introduced. In the discretized equations of the adatom model, in addition, first order operators arise. We describe these terms using

$$F[v] := \left(\int_{\Omega} v \cdot \nabla \varphi_i \varphi_j dx \right)_{ij}$$

with vector fields $v : \Omega \rightarrow \mathbb{R}^d$. With the system matrices

$$\begin{aligned} M_1 &:= M[|\nabla \phi^k|_{\delta}^{-1}], & L_1 &:= L[(\omega^k)^2 |\nabla \phi^k|_{\delta}^{-3}], \\ M_2 &:= M[1], & L_3 &:= L[|\nabla \phi^k|_{\delta}^{-1}], \\ M_3 &:= M[b |\nabla \phi^k|_{\delta}^{-1}], & L_4 &:= L[(I - P_{\Gamma}^k) |\nabla \phi^k|_{\delta}^{-1}], \\ M_4 &:= M[c |\nabla \phi^k|_{\delta}], & L_5 &:= L[\gamma_1 \left(\frac{\nabla \phi^k}{|\nabla \phi^k|_{\delta}} \right) |\nabla \phi^k|_{\delta}^{-1}], \\ M_5 &:= M[|\nabla \phi^{k+1}|_{\delta}], & L_6 &:= L[m |\nabla \phi^k|_{\delta} P_{\Gamma}^{k+1}], \\ M_6 &:= M[|\nabla \phi^{k+1}|_{\delta}^{-1} \nabla \phi^{k+1} \cdot \nabla (\phi^{k+1} - \phi^k)], & L_7 &:= L[(u^k)^2 |\nabla \phi^k|_{\delta}^{-1}], \\ F_1 &:= F[u^k \nabla u^k |\nabla \phi^k|_{\delta}^{-1}], & G &:= \left(\int_{\Omega} D\gamma_1(\nabla \phi^k) \cdot \nabla \varphi_i dx \right)_i \\ F_2 &:= F[(\phi^{k+1} - \phi^k) |\nabla \phi^{k+1}|_{\delta}^{-1} \nabla \phi^{k+1}], \end{aligned}$$

and the linear expansions

$$\begin{aligned} \phi^{k+1} &= \sum_{i=1}^N \bar{\phi}_i^{k+1} \varphi_i, \\ \omega^{k+1} &= \sum_{i=1}^N \bar{\omega}_i^{k+1} \varphi_i, \\ u^{k+1} &= \sum_{i=1}^N \bar{u}_i^{k+1} \varphi_i, \end{aligned}$$

the linear system for equations (6.18) and (6.19) reads

$$\begin{pmatrix} M_3 + \tau \frac{\epsilon^2}{2} L_1 + \tau \lambda L_5 & \tau \epsilon^2 L_3 \\ -\tau \frac{\alpha}{2} L_7 - \tau \alpha F_1 & \\ -L_3 & M_1 \end{pmatrix} \begin{pmatrix} \bar{\phi}^{k+1} \\ \bar{\omega}^{k+1} \end{pmatrix} = \begin{pmatrix} -\tau \alpha M_2 \bar{u}^k + M_3 \bar{\phi}^k + \tau \epsilon^2 L_4 \bar{\omega}^k \\ +\tau \lambda L_5 \bar{\phi}^k - \tau G \\ 0 \end{pmatrix}$$

We use a Schur complement approach to solve the system for the unknown ϕ^{k+1} , which gives

$$\begin{aligned} (M_3 + \tau \frac{\epsilon^2}{2} L_1 + \tau \lambda L_5 - \tau \frac{\alpha}{2} L_7 - \tau \alpha F_1 + \tau \epsilon^2 L_3 M_1^{-1} L_3) \bar{\phi}^{k+1} \\ = -\tau \alpha M_2 \bar{u}^k + M_3 \bar{\phi}^k + \tau \epsilon^2 L_4 \bar{\omega}^k + \tau \lambda L_5 \bar{\phi}^k - \tau G, \end{aligned}$$

where $\bar{\omega}^k$ is again calculated via $\bar{\omega}^k = M_1^{-1}L_3\phi^k$ and the inverse M_1^{-1} is obtained with mass lumping. The Schur complement system is solved by a GMRES-solver, as the system matrix might not be positive definite for the time steps used. And the linear system for equation (6.20) reads

$$[M_5 + (F_2 + F_2^T) + M_6 + \tau\alpha L_6 + \tau\alpha M_4] \bar{u}^{k+1} = M_5 \bar{u}^k + M_2(\bar{\phi}^{k+1} - \bar{\phi}^k).$$

It is solved by a GMRES-solver.

6.3 Extension of adatom density

In the redistancing algorithm described in section 2.4, the correct distance information is spread iteratively from the interface to all grid vertices. In each iteration step local distance updates are performed on each element. The updates provide the shortest distance with respect to the distances in neighboring grid vertices. After the algorithm has finished, each grid vertex holds the shortest distance, which is the normal distance, to the interface. That means, the redistancing algorithm spreads information in direction normal to the interface. This property is now used to extend the adatom density in normal direction. The redistancing algorithm is adapted in such a way, that, in addition to the distance information, the local updates also include an update on the adatom density.

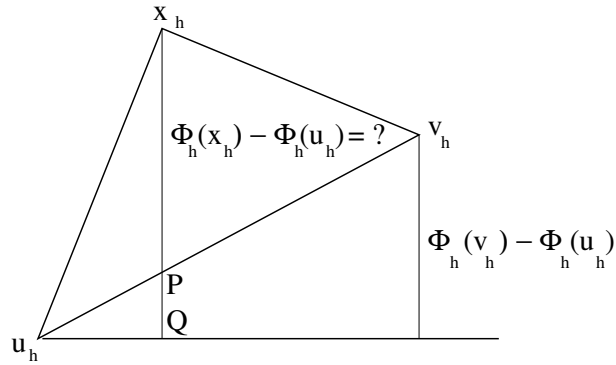


Figure 6.1: Local update in redistancing and extension algorithm for vertex x_h .

Updates of the adatom density on a grid vertex are performed if and only if a distance update is done, that means when the calculated new distance is smaller than the current distance at the vertex. We now assume that a distance update is performed. To recall how the updates work, let us look at figure 6.1. It illustrates the local update in 2D for the vertex x_h on a grid element with vertices u_h , v_h and x_h . The vertical line through the vertex x_h is the local approximation of the normal direction. In the local element-based update the approximated distance $\phi_h(x_h)$ of x_h to the interface is calculated under the assumption that $\phi_h(u_h)$ and $\phi_h(v_h)$ are the correct distances of u_h and v_h to the interface. It computes the distance

$$\phi_h(x_h) - \phi_h(u_h),$$

which is the distance of x_h to Q , and afterwards obtains the approximated distance $\phi_h(x_h)$ through

$$\phi_h(x_h) = \phi_h(u_h) + (\phi_h(x_h) - \phi_h(u_h)).$$

What is essential in the algorithm is the way the distance of x_h to Q is calculated. This is done as the sum of the distances of x_h to P and of P to Q , see [8] for details. In particular, the coordinates of P are calculated. Since we want to extend the adatom density in normal direction, the correct local extension is to set the adatom density in x_h to its value in P . The

adatom density in P is calculated by an interpolation of the adatom densities in u_h and v_h . That means the algorithm for the extension of the adatom density is only a slight adaption of the redistancing algorithm. See section 2.4 for more details on the redistancing algorithm.

6.4 Energy dissipation and volume conservation

It is sufficient to consider equations (6.6)-(6.8). Energy dissipation and volume conservation then follows for equations (6.9)-(6.11) with the same argumentation as in section 5.5. A transformation of (6.6)-(6.8) and equations (6.4) and (6.5) provide

$$\begin{aligned} u_t &= -(1 + uH)V + \nabla_\Gamma \cdot (m\nabla_\Gamma \mu) - c\mu \\ \mu &= \frac{\delta E}{\delta u} \\ (1 + uH)\frac{\delta E}{\delta u} &= bV + \frac{\delta E}{\delta \Gamma}. \end{aligned}$$

With the coefficients m , b and c being non-negative, energy dissipation then is ensured with the time derivative (2.10) through

$$\begin{aligned} \frac{d}{dt}E[\Gamma(t), u(\cdot, t)] &= \int_{\Gamma(t)} u_t \frac{\delta E}{\delta u} dA + \int_{\Gamma(t)} V \frac{\delta E}{\delta \Gamma} dA \\ &= - \int_{\Gamma(t)} V(1 + uH) \frac{\delta E}{\delta u} dA + \int_{\Gamma(t)} \nabla_\Gamma \cdot (m\nabla_\Gamma \frac{\delta E}{\delta u}) \frac{\delta E}{\delta u} dA - \int_{\Gamma(t)} c(\frac{\delta E}{\delta u})^2 dA \\ &\quad + \int_{\Gamma(t)} V \frac{\delta E}{\delta \Gamma} dA \\ &= - \int_{\Gamma(t)} bV^2 dA - \int_{\Gamma(t)} V \frac{\delta E}{\delta \Gamma} dA - \int_{\Gamma(t)} m(\nabla_\Gamma \frac{\delta E}{\delta u})^2 dA - \int_{\Gamma(t)} c(\frac{\delta E}{\delta u})^2 dA \\ &\quad + \int_{\Gamma(t)} V \frac{\delta E}{\delta \Gamma} dA \\ &\leq 0. \end{aligned}$$

The mass $mass(t)$ of the solid phase $B(t)$ at time t is now not only determined through the volume of the bounded domain $B(t)$, but has also contributions from the free adatoms on $\Gamma(t)$,

$$mass(t) = \int_{B(t)} 1 dx + \int_{\Gamma(t)} u dA. \quad (6.21)$$

The transport theorems (2.7) and (2.8) provide the change of mass

$$\begin{aligned} \frac{d}{dt}mass(t) &= \frac{d}{dt} \left(\int_{B(t)} 1 dx + \int_{\Gamma(t)} u dA \right) \\ &= \int_{\Gamma(t)} V dA + \int_{\Gamma(t)} u_t + uVH + \frac{\partial u}{\partial \nu} V dA \\ &= \int_{\Gamma(t)} V + u_t + uVH dA \\ &= \int_{\Gamma(t)} \nabla_\Gamma \cdot (m\nabla_\Gamma \mu) dA - \int_{\Gamma(t)} c\mu dA \\ &= - \int_{\Gamma(t)} c\mu dA, \end{aligned}$$

where the third equality follows from the constant extension of u in normal direction, which gives $\frac{\partial u}{\partial \nu} = 0$, the fourth equality from equation (6.6) and the last equality from integration by parts. Thus the evolution is mass conserving for $c = 0$.

6.5 Numerical results

The computational examples are chosen such that the effect of the free adatoms is highlighted. For that purpose, we compare the results with those in the kinetic model (5.20) and (5.21), in which the adatom density is neglected. We restrict to examples without attachment-detachment, i.e. we use the attachment rate $c = 0$ (surface diffusion with kinetics), which provides volume conserving examples. Furthermore, we fix the surface mobility to $m = 1.0$ and the kinetic coefficient to $b = 1.0$ in all our examples.

We will see that the changes in the adatom density distribution seem to be related to the local mean curvature terms, as mean curvature in isotropic situation and an interplay between mean curvature and weighted mean curvature in anisotropic situation, and the normal velocity, which again depends on the curvature. In the isotropic case the relation to the mean curvature has already been observed in [10] within a numerical study using a graph formulation. A comparison to results with a phase-field approximation in isotropic situation in [54], furthermore supports our observations.

If not stated otherwise we choose $\alpha = 1.0$ in the relation (6.17) of the chemical potential to the adatom density, $\lambda = 1.0$ in the semi-implicit discretization of the weighted mean curvature term, and a regularization parameter $\epsilon = 0.1$. The computational grid is again adaptively refined at the interface and with h denoting the grid size at the interface, we use timesteps Δt of about $\Delta t \leq h^4/\epsilon^2$. To obtain an appropriate resolution of rounded corners and edges we choose $h \sim \epsilon$, which provides a timestep restriction $\Delta t \leq h^2$ for our semi-implicit time discretization scheme. However, to track fast changes in the interface and to account for the operator splitting, the timestep is chosen smaller in some examples. In all our computational examples, we choose a constant initial adatom density.

6.5.1 Isotropic situation

We first of all discuss the isotropic situation ($\gamma_1 = 1$), which has been solved numerically within a graph formulation in [10] and with a phase-field approximation in [54]. The author in [10] analyzed the equilibrium shape corresponding to the energy (6.1), which in this situation reads

$$E[\Gamma, u] = \int_{\Gamma} 1 + \gamma_2(u) \, dA.$$

The author proves that for non-closed surfaces the equilibrium shape is the flat interface with vanishing adatom density $u = 0$. This corresponds to the equilibrium shape in the model of surface diffusion with kinetics. For closed surfaces it is shown that the equilibrium shape is a spherical shape (as in the model for surface diffusion with kinetics) with a constant adatom density. But in difference to non-closed surfaces, the adatom density is positive. The volume enclosed by the surface is not conserved under evolution. It increases if adatoms are incorporated into the solid and decreases if atoms of the solid become mobile again.

Circular shape. We start with a simple example, the evolution of a circle with radius $r_0 = 1.0$ and initial constant adatom density $u_0 = 0.6$. In [54] the analytical steady state solution for this problem is provided. Therein the adatom density u_{eq} in equilibrium is given through

$$u_{eq} = \frac{1}{2} \sqrt{\frac{8}{3} - \frac{8}{3}r_0^2 - \frac{16}{3}r_0u_0 + 2\sqrt{\frac{16}{3} + \left(\frac{4}{3} - \frac{4}{3}r_0^2 - \frac{8}{3}r_0u_0\right)^2}}.$$

The radius of the circle in equilibrium can be calculated using the mass conservation property. Under the assumption that the shape remains circular and the adatom density constant, and for $B(t)$ the domain enclosed by $\Gamma(t)$ at time t , we have the mass of the solid phase at time t

$$mass(t) = |B(t)| + u(t)|\Gamma(t)|,$$

which is equal to the initial mass, $mass(t) = mass(0)$, due to mass conservation. For our choice of initial radius and adatom density this gives $u_{eq} = 0.77766$ and $r_{eq} = 0.897$, which our computations match quite well, see figure 6.2. Furthermore, the results confirm that the evolving shape stays circular and the adatom density constant.

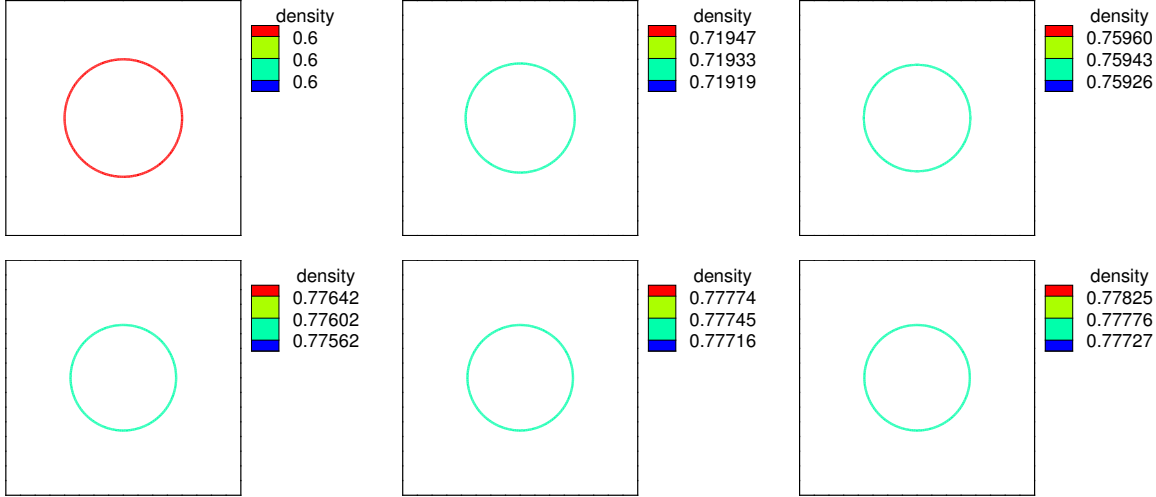


Figure 6.2: Isotropic evolution of interface and adatom density. Simulation parameters: $[0, 4] \times [0, 4]$ grid, grid size $h = 0.03125$, timestep $\Delta t = 10^{-4}$, $u_0 = 0.6$, initial radius of circle $r_0 = 1.0$. From top left to bottom right: $t = 0.0, 0.5, 1.0, 2.0, 3.0, 3.06$.

Closed curve. We now turn to a more complex example for isotropic evolution of a closed curve, the evolution of a star-shaped curve obtained by a regular perturbation of a circle. The evolution is in agreement with results from a phase-field approximation in [54]. The perturbations smooth out and the shape becomes circular. The adatom density adjusts to the local curvature and the normal velocity. In regions with highest positive mean curvature and fastest motion in negative normal direction the adatom density attains its maximum and in regions with smallest negative mean curvature and fastest motion in positive normal direction the adatom density attains its minimum. When Γ reaches a circular shape, the adatom density becomes constant and further increases to its equilibrium value, which is non-zero as expected and depends on the initial configuration.

Non-closed curve. Figure 6.4 shows the evolution of an interface with the shape of a sine function and the evolution of the adatom density on it. In agreement with the results obtained by a graph formulation [10] and a phase-field formulation [54] the curve becomes flat and the adatom density adjusts to the local curvature and velocity. After a straight line is formed the adatom density converges to zero as expected.

In figure 6.5 the evolution is compared with the model of surface diffusion with kinetics in which adatoms are neglected. Again the results agree, with the only difference, that the height in the adatom model is higher, which results from the additional mass from the adatoms, which become incorporated during the evolution. From a numerical point of view an additional difference is observed. The time steps in the adatom model can be chosen larger than for the model of surface diffusion with kinetics. This results from the diffusion character of the adatom model, and has already been speculated in [33].

Mass conservation. For the verification of the mass conservation, the mass is calculated with the formula (6.21), which includes the geometric volume and the adatom density. The evolution in figure 6.3 only leads to the very small change in mass of 0.04%, and the evolution in figure 6.4 reveals a minor mass change of about 1.2%.

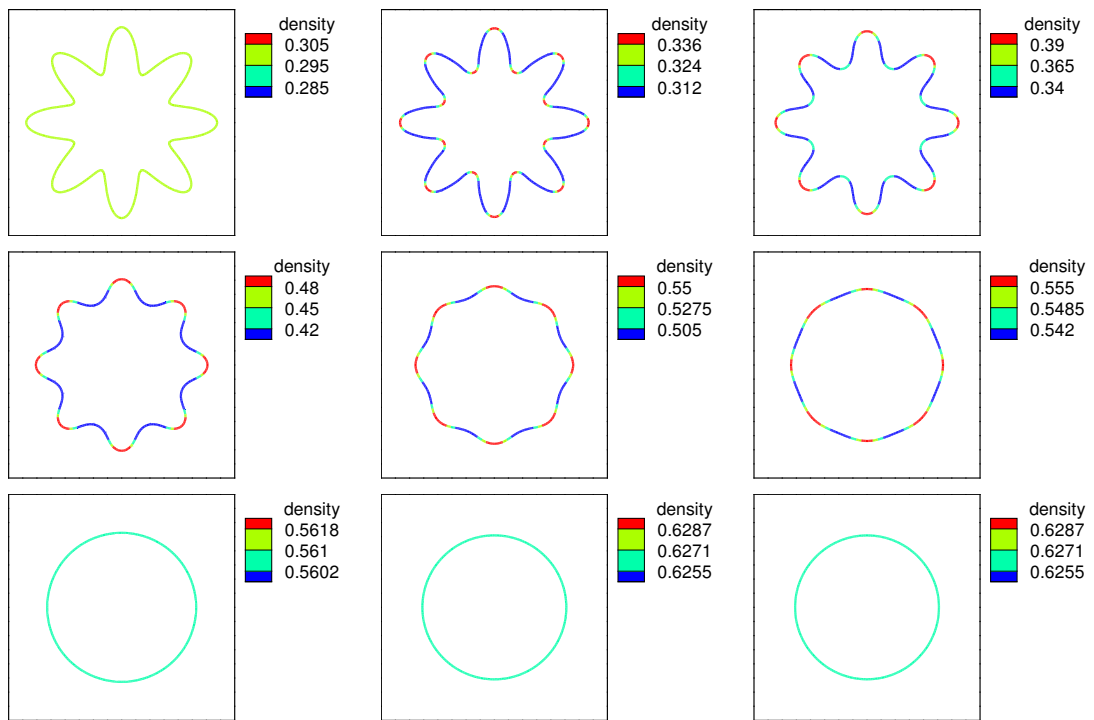


Figure 6.3: Isotropic evolution of interface and adatom density. Simulation parameters: $[0, 4] \times [0, 4]$ grid, grid size $h = 0.03125$, timestep $\Delta t = 10^{-5}$, $u_0 = 0.3$. From top left to bottom right: $t = 0.0, 0.002, 0.01, 0.03, 0.06, 0.09, 0.2, 2.5, 3.0$.

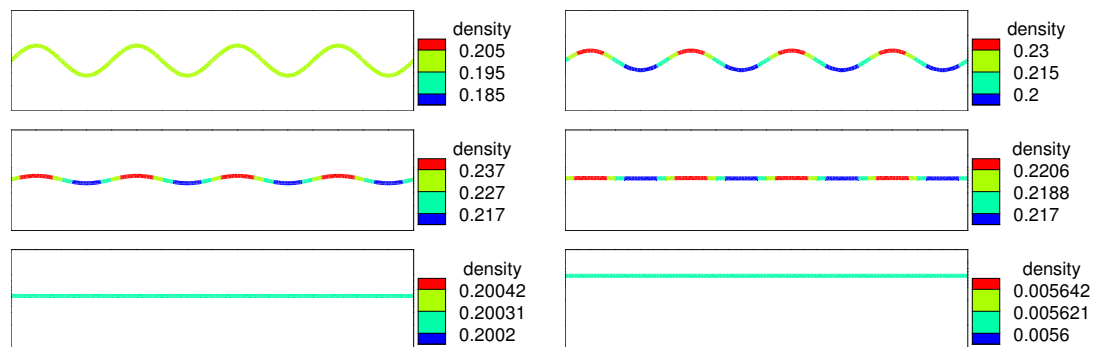


Figure 6.4: Isotropic evolution of interface and adatom density. Simulation parameters: $[0, 4] \times [-0.5, 0.5]$ grid, grid size $h = 0.03125$, timestep $\Delta t = 10^{-5}$, $u_0 = 0.2$. From top left to bottom right: $t = 0.0, 0.01, 0.03, 0.09, 0.2, 7.0$.

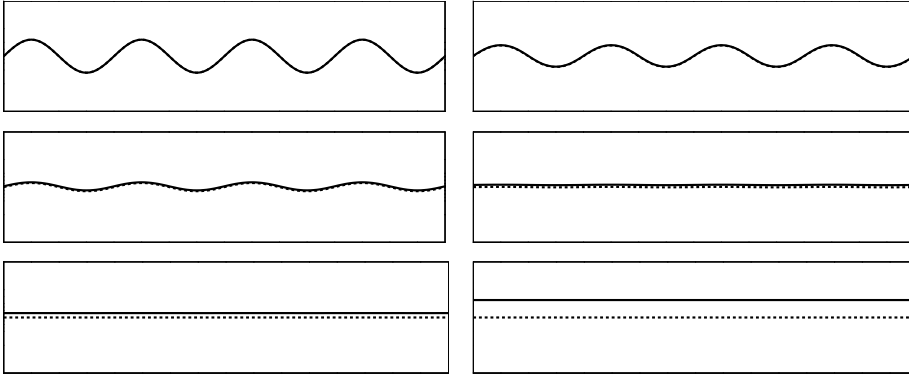


Figure 6.5: Isotropic evolution: comparison of adatom model (solid) and kinetic model (dashed). Simulation parameters: $[0, 4] \times [-0.5, 0.5]$ grid, grid size $h = 0.03125$, timestep $\Delta t = 10^{-5}$ (adatom model) and $\Delta t = 5 \times 10^{-6}$ (kinetic model). In adatom model: $u_0 = 0.2$. From top left to bottom right: $t = 0.0, 0.01, 0.03, 0.09, 0.2, 1.3$.

6.5.2 Strong anisotropic situation

As in the previous simulations with strong anisotropies, we use the non-convex anisotropy function

$$\gamma(p) = |p| + a \sum_{i=1}^d \frac{p_i^4}{|p|^3}.$$

If not stated otherwise, we choose $a = 2.0$. Concerning the adatom density in equilibrium state, we will see in our computational examples that the adatom density decreases for non-closed surfaces after reaching a constant value. We suppose that it slowly converges to zero. We further suppose that it becomes constant with a non-zero value for closed surfaces, which would be the same behavior as under isotropic evolution. In particular, the adatom density does not adjust to the local mean curvature.

Closed curve. Figure 6.7 shows the evolution of a circle and the adatom density on it. During the evolution to the wulffshape (where we mean only the shape and not the volume conservation), the adatom concentration adjusts to the local weighted mean curvature and velocity and becomes constant after the wulffshape is reached. The weighted mean curvature is initially large in regions which tend towards facets and small in regions which later become corners. To illustrate the interplay between the mean curvature and the weighted mean curvature of the adatom density during the evolution towards the final equilibrium value, we have chosen a small

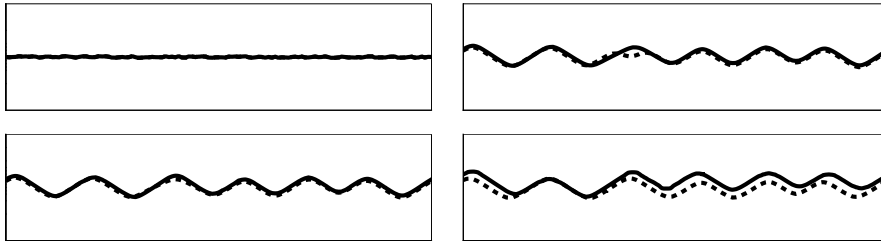


Figure 6.6: Anisotropic evolution: comparison of adatom model (solid) and kinetic model (dashed). Simulation parameters: $[0, 4] \times [-0.5, 0.5]$ grid, grid size $h = 0.03125$, timestep $\Delta t = 10^{-5}$ (adatom model) and $\Delta t = 5 \times 10^{-6}$ (kinetic model). In adatom model: $u_0 = 0.2$. From top left to bottom right: $t = 0.0, 0.07, 0.08, 0.4$.

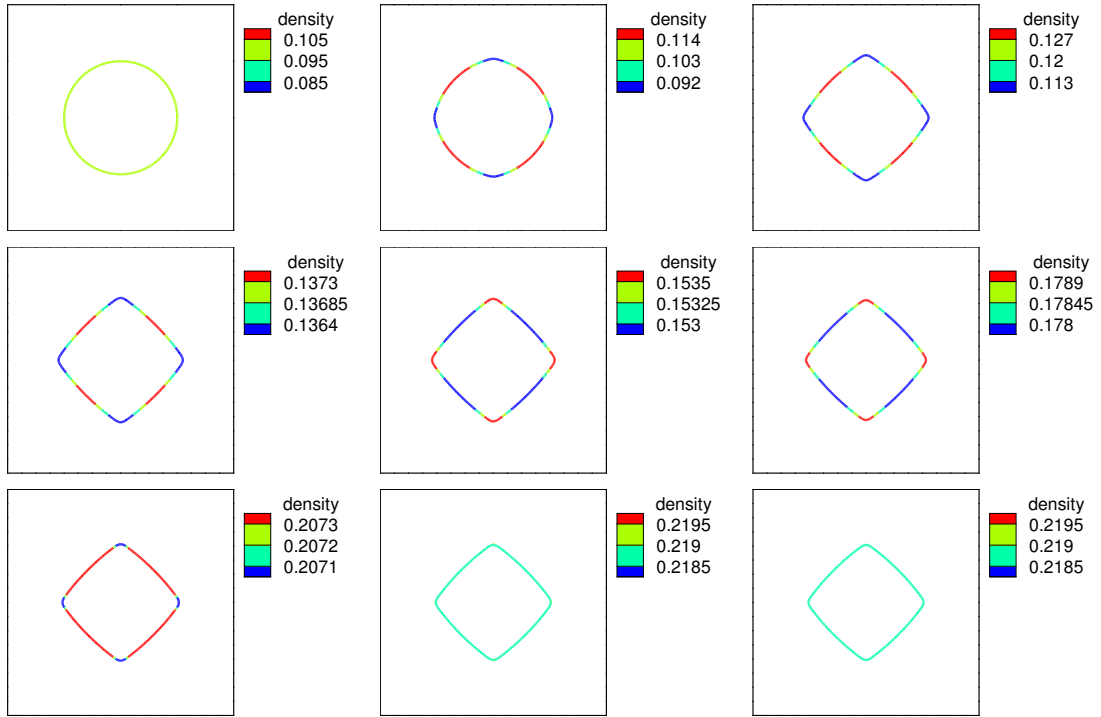


Figure 6.7: Anisotropic evolution of interface and adatom density. Simulation parameters: $[0, 4] \times [0, 4]$ grid, grid size $h = 0.03125$, timestep $\Delta t = 10^{-5}$, $u_0 = 0.1$, $\alpha = 10.0$. From top left to bottom right: $t = 0.0, 0.005, 0.02, 0.04, 0.06, 0.1, 0.2, 0.5, 1.0$.

resolution in the color bar. The adatom density is slightly higher in the corners than on the facets.

If we compare this evolution with the model of surface diffusion with kinetics in which adatoms are neglected, we obtain similar results on the dynamics and the equilibrium shape, see figure 6.8. The only difference is the size of the final shape, as in the model of surface diffusion with kinetics conservation in mass results in conservation in area, which is not the case in the adatom model. Here the area can be reduced by increasing the adatom density. Numerically we can again use larger time steps in the adatom model.

Non-closed curves. Figure 6.9 shows the evolution of an interface with the shape of a sine function and the evolution of the adatom density on it. We observe the facet formation and the adjustment of the adatom density to the local curvature and velocity. After the facets are formed

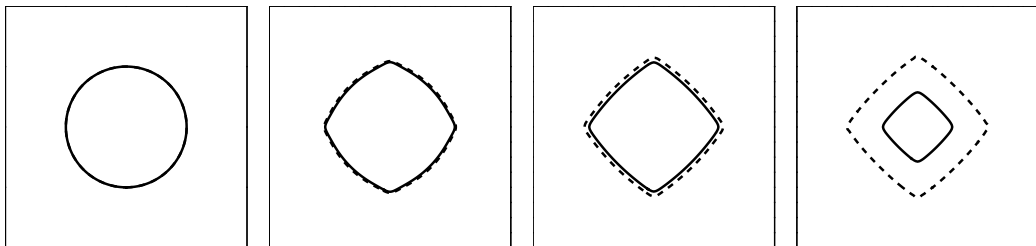


Figure 6.8: Anisotropic evolution: comparison of adatom model (solid) and kinetic model (dashed). Simulation parameters: $[0, 4] \times [0, 4]$ grid, grid size $h = 0.03125$, timestep $\Delta t = 10^{-5}$ (adatom model) and $\Delta t = 5 \times 10^{-6}$ (kinetic model). In adatom model: $u_0 = 0.1$. From left to right: $t = 0.0, 0.01, 0.03, 0.2$.

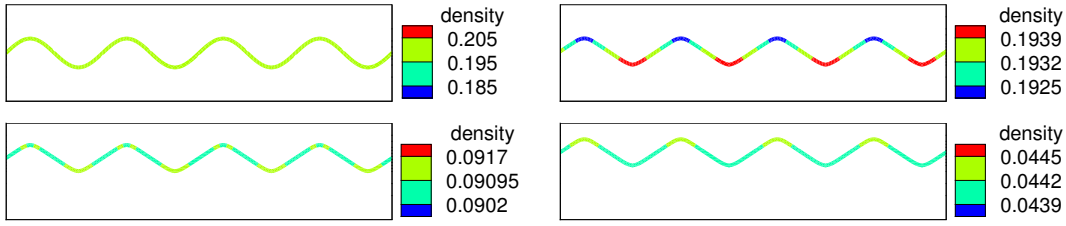


Figure 6.9: Anisotropic evolution of interface and adatom density. Simulation parameters: $[0, 4] \times [-1.0, 1.0]$ grid (shown here: $[0, 4] \times [-0.5, 0.5]$), grid size $h = 0.03125$, timestep $\Delta t = 10^{-5}$, $u_0 = 0.2$. From top left to bottom right: $t = 0.0, 0.09, 1.0, 2.0$.

the adatom density is reduced. It seems to converge towards zero. The structure however is not stable, due to the corner energy resulting from the regularization. Thus coarsening is expected, which will reduce the number of corners.

To further study the effect of coarsening on the adatom distribution, we now start from an initially unstable orientation. In figure 6.11 we start with a straight line with small random perturbations and in 6.12 with a slightly bent straight line. Both evolution processes show the spinodal decomposition into allowed orientations and the subsequent coarsening of the structure. The influence of the coarsening event on the adatom density can clearly be observed. During coarsening the interface moves fast. High velocities in the coarsening areas result in a smaller adatom density where the interface moves in positive normal direction and a higher adatom density where the interface moves in negative normal direction.

Again, we compare this evolution with the model of surface diffusion with kinetics. Figure 6.6 shows the qualitative agreement. Numerically we can again use larger time steps in the adatom model.

Non-closed surfaces. In figure 6.13 the evolution starts with a randomly perturbed initial surface within an unstable orientation. Again, the facet formation and the subsequent coarsening of the surface morphology can be observed. The adatom density adjusts rather to the velocity than to the local curvature. Again, it increases in regions with fast motion in negative normal direction and decreases in regions moving in normal direction. If we start with a periodic structure and a constant initial adatom density, we observe a symmetric coarsening in which four mounds collapse to form one mound, see figure 6.14. This symmetry probably is a result of the 4-fold symmetry of the anisotropy function.

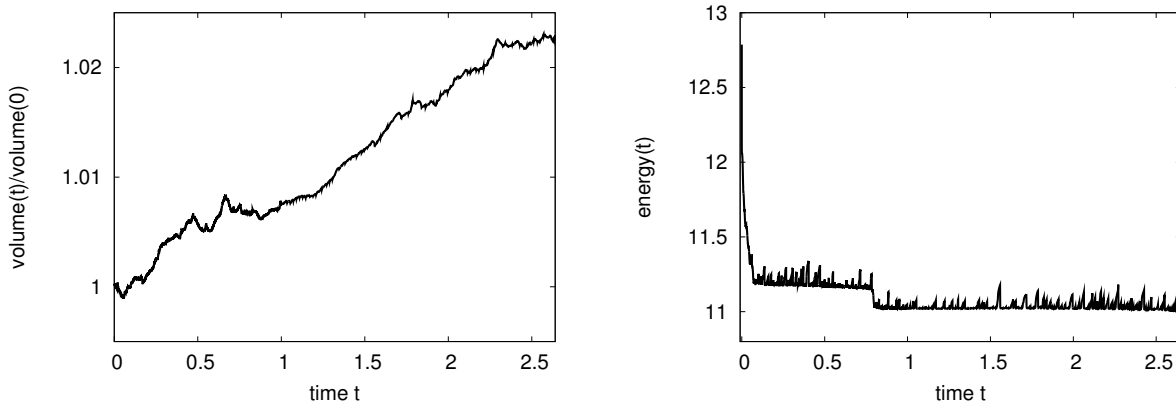


Figure 6.10: Change of volume (left) and energy dissipation (right) during the evolution with the adatom model for the example in figure 6.11.

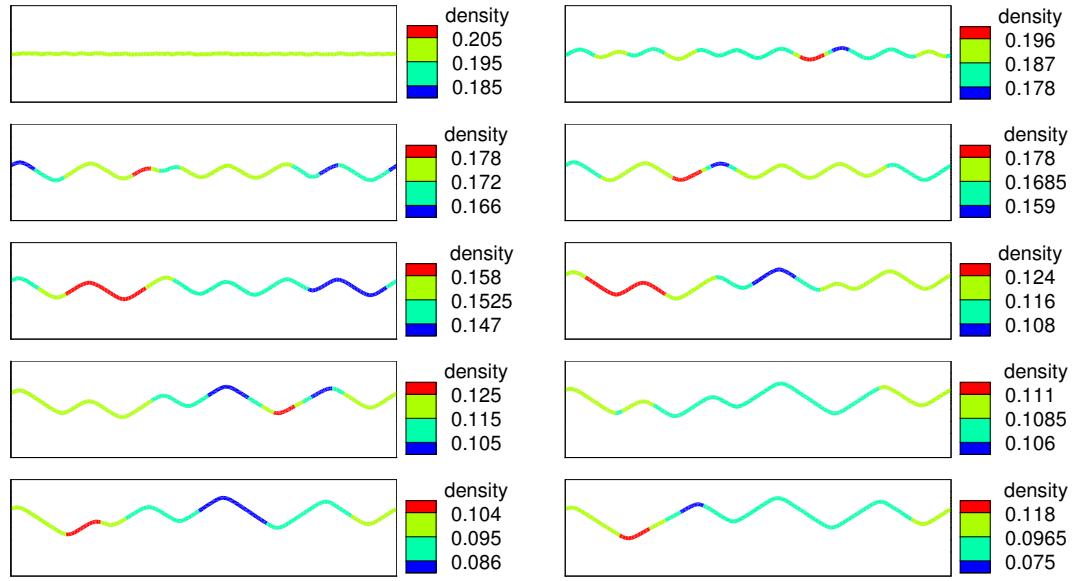


Figure 6.11: Anisotropic evolution of interface and adatom density. Simulation parameters: $[0, 4] \times [-1.0, 1.0]$ grid (shown here: $[0, 4] \times [-0.5, 0.5]$), grid size $h = 0.03125$, timestep $\Delta t = 10^{-5}$, $u_0 = 0.2$. From top left to bottom right: $t = 0.0, 0.02, 0.06, 0.07, 0.2, 0.76, 0.8, 1.2, 2.6, 2.64$.

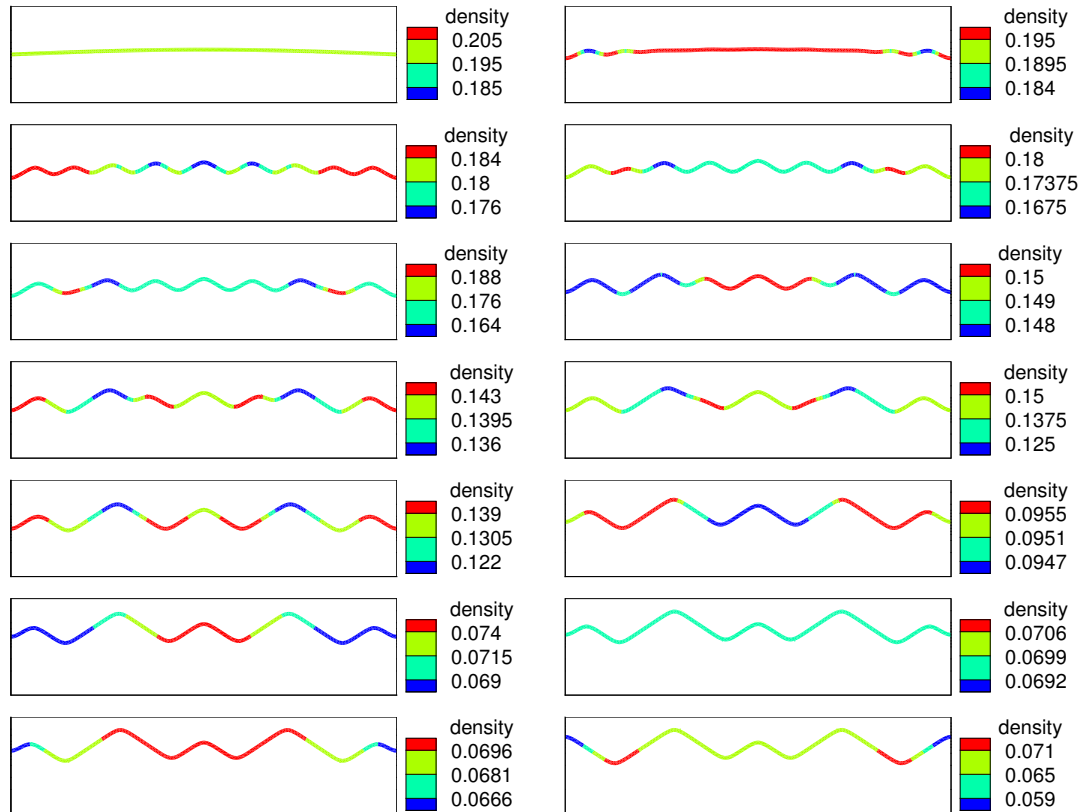


Figure 6.12: Anisotropic evolution of interface and adatom density. Simulation parameters: $[0, 4] \times [-1.0, 1.0]$ grid (shown here: $[0, 4] \times [-0.5, 0.5]$), grid size $h = 0.03125$, timestep $\Delta t = 10^{-5}$, $u_0 = 0.2$. From top left to bottom right: $t = 0.0, 0.008, 0.02, 0.07, 0.08, 0.3, 0.4, 0.42, 0.43, 0.9, 1.4, 2.4, 2.5, 2.6$.

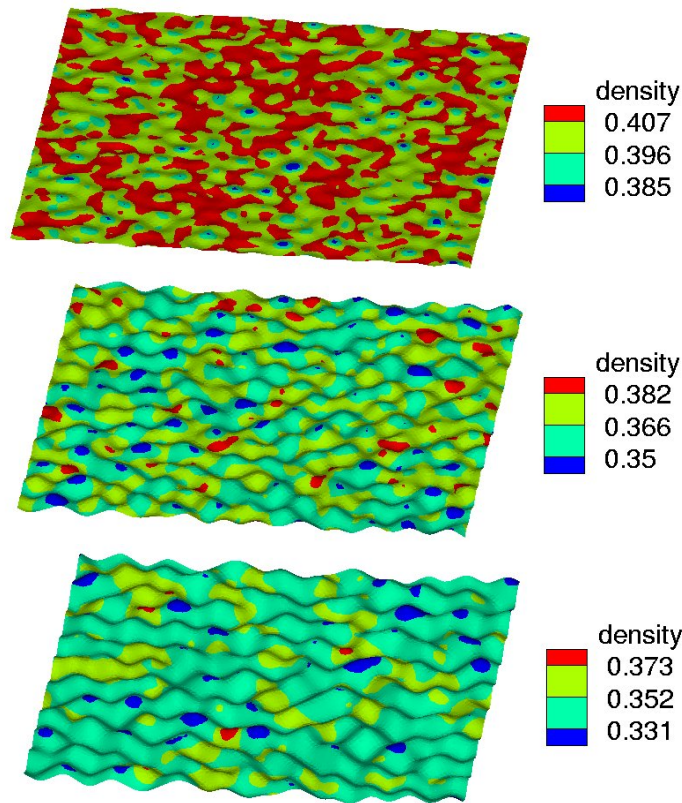


Figure 6.13: Anisotropic evolution of interface and adatom density. Simulation parameters: $[-2.0, 2.0] \times [-2.0, 2.0] \times [-0.5, 0.5]$ grid, grid size $h = 0.03125$, timestep $\Delta t = 10^{-5}$, $\epsilon = 0.07$, $u_0 = 0.4$. From top to bottom: $t = 0.001, 0.005, 0.014$.

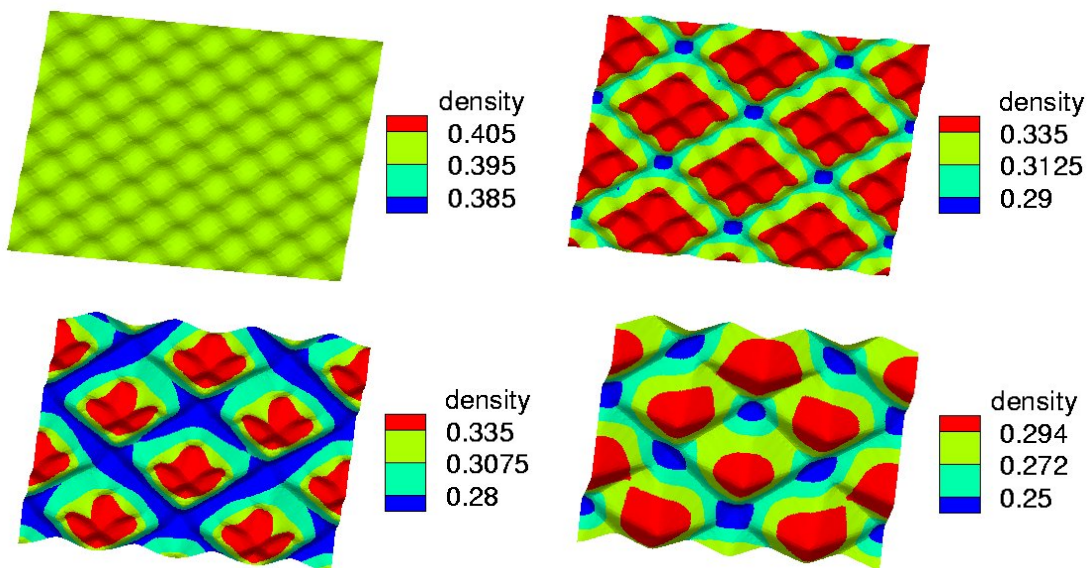


Figure 6.14: Anisotropic evolution of interface and adatom density. Simulation parameters: $[-2.0, 2.0] \times [-2.0, 2.0] \times [-0.5, 0.5]$ grid, grid size $h = 0.05$, timestep $\Delta t = 10^{-4}$, $\epsilon = 0.07$, $u_0 = 0.4$. From top left to bottom right: $t = 0.0, 0.05, 0.1, 0.15$.

Mass conservation and energy dissipation. The numerical examples in this subsection show a mass change of at most 2.8%. The change of mass and energy in time is shown in figure 6.10 for the example in figure 6.11. In the energy plot therein, the fast energy decrease during the coarsening processes at the time intervals from $t = 0.76$ to $t = 0.8$ and from $t = 2.6$ to $t = 2.64$ can be observed quite well.

In our simulations the parameters have been chosen to show the applicability of the algorithm. Especially, the physical range for the adatom density between 0 and 1 is not guaranteed by the algorithm. A study with more realistic physical parameters would be interesting. A challenging task is also to explore the influence of free adatoms on coarsening laws as derived in [37] and [70].

Chapter 7

Geodesic evolution laws

In the previous chapters we have considered planar motion of curves and motion of surfaces in three-dimensional Eukclidean space. We now focus on geometric evolution equations of curves but drop the restriction to planar space. The evolution of curves constrained to two-dimensional surfaces is presented. As example, we treat again mean curvature flow and surface diffusion, which in the context of evolution on surfaces are called geodesic mean curvature flow and geodesic surface diffusion. Isotropy is considered. The evolution laws now read

$$V_g = -\kappa_g \quad \text{and} \quad V_g = \Delta_g \kappa_g,$$

with the intrinsic normal velocity V_g , the intrinsic mean curvature κ_g of the curve on the surface and the intrinsic Laplacian Δ_g of the curve on the surface. PDEs on surfaces can be found e.g. in ice accretion on cold surfaces in materials science [47], texture generation and tangential flow field visualization in computer graphics [68, 26] and brain imaging in image processing [31]. Geodesic mean curvature flow has already been treated in several works, with finite differences in [17] and [16] and with finite elements in [29]. The authors in [34] numerically solve fourth order PDEs on surfaces with finite difference schemes, and in [29] the level set equation of geodesic surface diffusion is presented, but no numerical results for geodesic surface diffusion are known so far.

For the computational treatment in addition to a representation of the evolving curve an appropriate approximation of the surface is needed. The approaches vary from surface triangulations [68, 26, 29] over the use of parameterization planes [18, 40, 6, 61] to implicit surface representations [7, 16, 17, 34, 11]. The first approach requires the creation of a surface mesh. This might be a tricky task. However, there are many sophisticated mesh generation algorithms and software packages, in particular in the field of computer aided design. Numerical problems arise when the mesh is not sufficiently regular. The second approach makes use of a parametric function, which gives the surface as the image of a planar domain under this function. The problem on the surface is projected on the planar domain. In the last approach mentioned the surface is given implicitly as a level set, typically the zero level set, of a function. As we deal with two-dimensional surfaces this function is defined in \mathbb{R}^3 , thus again we have an increase in dimension. The computational overhead has to be compensated by using narrow bands or adaptively refined meshes at the surface. The advantage of this approach is that standard space discretizations can be used, where the numerics behind is well understood. We present the finite element treatment for the surface mesh approach and the implicit surface representation and compare numerical results. PDEs on implicit surfaces have been introduced in [7]. Further works in this context are [17, 31, 34] using finite difference schemes and [11] in the finite element framework.

7.1 Level set method for geodesic evolution laws

Transferring PDEs from Euklidian space to surfaces formally means a switch from gradients to their counterparts on surfaces, namely tangential or surface gradients. A comparison of the equations presented in this chapter with the equations in chapter 3 shows this analogy. We derive the equations for the motion of $(d-1)$ -dimensional surfaces on d -dimensional surfaces. In \mathbb{R}^3 this is the motion of curves on two-dimensional surfaces. We will therefore from now on refer to moving curves on surfaces. The evolving curve C is represented by the zero level set $\{u = 0\}$ of a function u defined in the neighborhood of the surface Γ in \mathbb{R}^{d+1} . The curve moves in intrinsic normal direction

$$\nu_g = \frac{\nabla_\Gamma u}{|\nabla_\Gamma u|}$$

with a velocity depending on its mean curvature (geodesic curvature)

$$\kappa_g = \nabla_\Gamma \cdot \nu_g = \nabla_\Gamma \cdot \frac{\nabla_\Gamma u}{|\nabla_\Gamma u|}.$$

With V_g being the velocity in intrinsic normal direction, the level set equation in intrinsic form reads

$$u_t + V_g |\nabla_\Gamma u| = 0. \quad (7.1)$$

It describes the motion of the curve on the surface. It delivers an expression for the intrinsic normal velocity in terms of u , which is

$$V_g = -\frac{u_t}{|\nabla_\Gamma u|}. \quad (7.2)$$

Geodesic mean curvature flow with the evolution law

$$V_g = -\kappa_g$$

relates the intrinsic normal velocity to minus the geodesic curvature. Using the expression for the intrinsic normal velocity (7.2) we obtain the level set representation for geodesic mean curvature flow

$$\frac{u_t}{|\nabla_\Gamma u|} = \nabla_\Gamma \cdot \frac{\nabla_\Gamma u}{|\nabla_\Gamma u|}.$$

In a similar way we can consider motion by geodesic surface diffusion

$$V_g = \Delta_g \kappa_g.$$

Here the intrinsic normal velocity is given by the intrinsic Laplacian of C on Γ of the geodesic curvature. Thus Δ_g depends on C and Γ . In level set representation geodesic surface diffusion, rewritten as a system of two second order equations for u and v , reads

$$\begin{aligned} u_t &= \nabla_\Gamma \cdot (|\nabla_\Gamma u| (I - \nu_g \otimes \nu_g) \nabla_\Gamma v) \\ v &= \nabla_\Gamma \cdot \frac{\nabla_\Gamma u}{|\nabla_\Gamma u|}. \end{aligned}$$

7.1.1 Level set method for geodesic evolution laws on implicit surfaces

We now define the surface Γ as the zero level line of the level set function ϕ defined in a domain $\Omega \subseteq \mathbb{R}^{d+1}$ containing Γ . Our PDEs can now be understood as PDEs defined on a set of surfaces in Euklidean space, each surface given by a specific level line of ϕ . The level set function u is now also defined on Ω and the evolving curve C is given as the intersection $C = \{x \in \Omega \mid \phi(x) = u(x) = 0\}$. Again, following [7] and [29], the PDEs of interest can be formulated in terms of gradients in the Euklidean space. The level set equation (7.1) now reads in its extended version to Ω

$$u_t + V_g |(I - \nu \otimes \nu) \nabla u| = 0,$$

where (2.2) has been employed to represent the surface gradient in terms of the surface normal. We can define the intrinsic normal and the intrinsic curvature (geodesic curvature) to each level line of u and ϕ through the functions u and ϕ . Doing so for the curve C , which is the zero level line of u and which evolves on the zero level line of ϕ , gives with (2.2) and (2.15)

$$\nu_g = \frac{(I - \nu \otimes \nu) \nabla u}{|(I - \nu \otimes \nu) \nabla u|}, \quad \kappa_g = \frac{1}{|\nabla \phi|} \nabla \cdot (|\nabla \phi| \frac{(I - \nu \otimes \nu) \nabla u}{|(I - \nu \otimes \nu) \nabla u|}).$$

The level set representation for geodesic mean curvature flow on an implicitly defined surface thus reads

$$\frac{u_t}{|(I - \nu \otimes \nu) \nabla u|} = \frac{1}{|\nabla \phi|} \nabla \cdot (|\nabla \phi| \frac{(I - \nu \otimes \nu) \nabla u}{|(I - \nu \otimes \nu) \nabla u|}). \quad (7.3)$$

In the same way we obtain the level set representation for geodesic surface diffusion on implicitly defined surfaces as

$$u_t = \frac{1}{|\nabla \phi|} \nabla \cdot (|\nabla \phi| |(I - \nu \otimes \nu) \nabla u| (I - \nu_g \otimes \nu_g) (I - \nu \otimes \nu) \nabla v) \quad (7.4)$$

$$v = \frac{1}{|\nabla \phi|} \nabla \cdot (|\nabla \phi| \frac{(I - \nu \otimes \nu) \nabla u}{|(I - \nu \otimes \nu) \nabla u|}). \quad (7.5)$$

7.2 Discretization

7.2.1 Discretization for the surface mesh approach

Modern finite element toolboxes are not restricted to meshes in Euklidean space, but work on non-planar spaces as well. This is due to the fact that finite elements on non-planar meshes can be defined in a standard way. After space discretization, i.e. on surface meshes, surface gradients and gradients are the same, because the calculation of gradients in finite element framework is done locally on mesh elements, which are plane. Thus surface gradients are treated in a natural way. The weak formulation and the discretization of equations look the same as in their counterpart in Euklidean space, except that gradients are replaced by surface gradients and the integration domain is a surface, and we just mentioned that this makes no difference for implementations. In our finite element toolbox AMDiS, see [2] and [69], no changes in the implementation and definition of equations are needed for the change from planar space to surfaces. The only requirement is an appropriate surface mesh.

To show the analogy to the formulation for curves moving in planar space in sections 3.1 and 3.2, we present the weak form for geodesic mean curvature flow and geodesic surface diffusion on triangulated surfaces, which is

$$\int_{\Gamma} \frac{u_t \eta}{|\nabla_{\Gamma} u|} dA = - \int_{\Gamma} \frac{\nabla_{\Gamma} u \cdot \nabla_{\Gamma} \eta}{|\nabla_{\Gamma} u|} dA$$

and

$$\begin{aligned}\int_{\Gamma} u_t \eta \, dA &= - \int_{\Gamma} |\nabla_{\Gamma} u| (I - \nu \otimes \nu) \nabla_{\Gamma} \psi \cdot \nabla_{\Gamma} \eta \, dA \\ \int_{\Gamma} \psi \xi \, dA &= \int_{\Gamma} \frac{\nabla_{\Gamma} u \cdot \nabla_{\Gamma} \xi}{|\nabla_{\Gamma} u|} \, dA,\end{aligned}$$

respectively, with test functions $\eta, \xi \in C_0^{\infty}(\Gamma)$.

We note that it is not straight forward to apply finite difference schemes on surface meshes, because the standard approximation schemes for derivatives of second or higher order involve points of different surface meshes.

7.2.2 Discretization for the implicit surface approach

The implicitly defined surface Γ is embedded into a simple domain Ω . The weak form of equations (7.3) and (7.4)-(7.5), which are here equations in Ω , reads

$$\int_{\Omega} \frac{u_t |\nabla \phi|}{|(I - \nu \otimes \nu) \nabla u|} \eta \, dx = - \int_{\Omega} |\nabla \phi| \frac{(I - \nu \otimes \nu) \nabla u}{|(I - \nu \otimes \nu) \nabla u|} \cdot \nabla \eta \, dx$$

and

$$\begin{aligned}\int_{\Omega} |\nabla \phi| u_t \eta \, dx &= \int_{\Omega} |\nabla \phi| |(I - \nu \otimes \nu) \nabla u| (I - \nu_g \otimes \nu_g) (I - \nu \otimes \nu) \nabla v \cdot \nabla \eta \, dx \\ \int_{\Omega} |\nabla \phi| v \xi \, dx &= - \int_{\Omega} |\nabla \phi| \frac{(I - \nu \otimes \nu) \nabla u}{|(I - \nu \otimes \nu) \nabla u|} \cdot \nabla \xi \, dx,\end{aligned}$$

respectively, with test functions $\eta, \xi \in C_0^{\infty}(\Omega)$.

The domain Ω is again chosen in a way which allows for easy triangulation. This is no restriction because the only requirement on Ω is that it contains the surface Γ . After space and time discretization, the discretized equations for geodesic mean curvature flow are given through

$$\begin{aligned}\int_{\Omega} \frac{u^{k+1} |\nabla \phi|_{\delta}}{|(I - \nu \otimes \nu) \nabla u^k|_{\delta}} \eta \, dx - \int_{\Omega} \frac{u^k |\nabla \phi|_{\delta}}{|(I - \nu \otimes \nu) \nabla u^k|_{\delta}} \eta \, dx + \\ \tau \int_{\Omega} |\nabla \phi|_{\delta} \frac{(I - \nu \otimes \nu) \nabla u^{k+1}}{|(I - \nu \otimes \nu) \nabla u^k|_{\delta}} \cdot \nabla \eta \, dx = 0.\end{aligned}\quad (7.6)$$

With the linear expansion $u = \sum_{i=1}^N \bar{u}_i \varphi_i$ and

$$\begin{aligned}M_1 &:= M[|\nabla \phi|_{\delta} |(I - \nu \otimes \nu) \nabla u^k|_{\delta}^{-1}], \\ L_1 &:= L[|\nabla \phi|_{\delta} |(I - \nu \otimes \nu) \nabla u^k|_{\delta}^{-1} (I - \nu \otimes \nu)]\end{aligned}$$

the linear system corresponding to (7.6) then reads

$$(M_1 + \tau L_1) \bar{u}^{k+1} = M_1 \bar{u}^k.$$

We solve the linear system with the Krylov subspace method BiCGStab2.

In a similar way the discretization for geodesic surface diffusion results in

$$\begin{aligned}\int_{\Omega} |\nabla \phi|_{\delta} u^{k+1} \eta \, dx - \int_{\Omega} |\nabla \phi|_{\delta} u^k \eta \, dx - \\ \tau \int_{\Omega} |\nabla \phi|_{\delta} |(I - \nu \otimes \nu) \nabla u^k|_{\delta} (I - \nu_g^k \otimes \nu_g^k) (I - \nu \otimes \nu) \nabla v^{k+1} \cdot \nabla \eta \, dx = 0\end{aligned}\quad (7.7)$$

$$\int_{\Omega} |\nabla \phi|_{\delta} v^{k+1} \xi \, dx + \int_{\Omega} |\nabla \phi|_{\delta} \frac{(I - \nu \otimes \nu) \nabla u^{k+1}}{|(I - \nu \otimes \nu) \nabla u^k|_{\delta}} \cdot \nabla \xi \, dx = 0,\quad (7.8)$$

where $\nu_g^k = \frac{(I - \nu \otimes \nu) \nabla u^k}{|(I - \nu \otimes \nu) \nabla u^k|}$ is the intrinsic surface normal in the last timestep. With the linear expansions $u = \sum_{i=1}^N \bar{u}_i \varphi_i$ and $v = \sum_{i=1}^N \bar{v}_i \varphi_i$, and the matrices

$$\begin{aligned} M_1 &:= M[|\nabla \phi|_\delta], \\ L_1 &:= L[|\nabla \phi|_\delta | (I - \nu \otimes \nu) \nabla u^k |_\delta (I - \nu_g^k \otimes \nu_g^k) (I - \nu \otimes \nu)], \\ L_2 &:= L[|\nabla \phi|_\delta | (I - \nu \otimes \nu) \nabla u^k |_\delta (I - \nu \otimes \nu)], \end{aligned}$$

the linear system corresponding to (7.7) and (7.8) reads

$$\begin{pmatrix} M_1 & -\tau L_1 \\ L_2 & M_1 \end{pmatrix} \begin{pmatrix} \bar{u}^{k+1} \\ \bar{v}^{k+1} \end{pmatrix} = \begin{pmatrix} M_1 \bar{u}^k \\ 0 \end{pmatrix}.$$

The linear system is solved with a Schur complement approach

$$(M_1 + \tau L_1 M_1^{-1} L_2) \bar{u}^{k+1} = M_1 \bar{u}^k$$

and the Krylov subspace method BiCGStab2.

7.3 Numerical results

Numerical results and a comparison of the two discussed approaches are presented. We do not use redistancing of the level set function u . Therefore it is possible to show the simultaneous evolution of different level lines of u . In the implicit surface approach, we apply mesh adaptivity at the surface Γ to keep computational costs low. Again, the criterion for mesh refinement is the distance to the surface, which is controlled by the level set function ϕ . The mesh adaption is illustrated in figure 7.1.

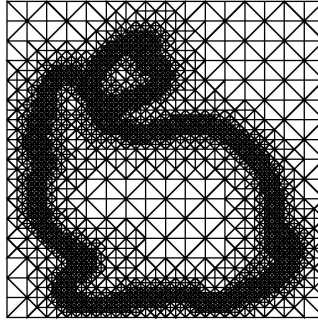


Figure 7.1: Cut through adaptive grid used for calculations shown in figures 7.10 and 7.11. Adaptive grid refinement at the implicit surface $\phi = 0$. The complete grid has 192.000 grid points.

7.3.1 Geodesic mean curvature flow

To validate our computations for geodesic mean curvature flow on implicit surfaces, we consider the evolution of a circle on a sphere, where the exact solution can be calculated easily, and compare our computational results for different grid sizes and timesteps with the exact evolution. The evolution of a circle with initial radius R_0 on a sphere with radius r gives at time t a circle with radius

$$R(t) = \left(r^2 - \left(\frac{t}{r} + (r^2 - R_0^2)^{1/2} \right) \right)^{1/2}.$$

In our example we choose $r = 1.0$ and $R_0 = 0.3$. The evolution is shown in figure 7.2 and analyzed in figure 7.3. The figure shows that the choice of grid size $h = 0.0625$ and timestep $\Delta t = h^2$ is appropriate.

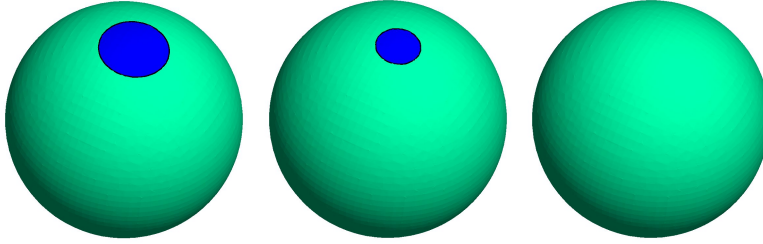


Figure 7.2: Geodesic mean curvature flow with level set representation of the surface: evolution of circle. $[0, 4] \times [0, 4] \times [0, 4]$ grid with 30.000 grid points, grid size $h = 0.0625$ at the surface and timestep $\Delta t = h^2 = 0.0039$. From left to right: $t = 0.0$, $t = 0.0273$, $t = 0.0468$.

Figures 7.6 and 7.8 show the evolution under geodesic mean curvature flow for different level lines on the sphere and the torus, respectively. In these figures, results for a triangulated surface (surface mesh) and an implicit surface are compared. Up to minor differences, the results are undistinguishable. This is a further test for the correctness of our computations. However, the computational costs for the implicit surface approach are higher. In figure 7.8 the initial closed curves on the torus are circles with a superposition of sine functions with two different frequencies. As expected, the high frequencies are damped first before the lower frequencies vanish on a larger time scale. Figure 7.10 shows the evolution of a sine function under geodesic mean curvature flow on the bunny.

7.3.2 Geodesic surface diffusion

To validate our computations for geodesic surface diffusion on implicit surfaces, we check the volume conservation property. We consider the example in figure 7.4 for different grid sizes and timesteps. The volume conserving behavior is presented in figure 7.5. Again, the figure shows that the choice of grid size $h = 0.0625$ and timestep $\Delta t = h^4$ is appropriate.

Again, we compare results of geodesic surface diffusion for triangulated and implicit surfaces, see figure 7.7 and 7.9. The match of the results confirms the correctness of our computations. Figure 7.11 shows the evolution of a sine function under geodesic surface diffusion on the bunny.

7.4 An application of geodesic mean curvature flow in image denoising

In image processing the diffusion or heat equation plays an important role. One important example is the ROF model for image denoising proposed by Rudin, Osher and Fatemi in [55]. With its adaption in [44], which yields to circumvent strong timestep restrictions, it can be considered as mean curvature flow with a forcing term. We present it here as an application of geodesic mean curvature flow.

For an initial noisy image u_0 , the evolution equation in \mathbb{R}^{d+1} in level set formulation is

$$u_t = |\nabla u| \left(\nabla \cdot \frac{\nabla u}{|\nabla u|} - 2\lambda(u - u_0) \right)$$

with the forcing term coefficient λ . The equation can also be applied on surfaces which gives

$$u_t = |\nabla_{\Gamma} u| \left(\nabla_{\Gamma} \cdot \frac{\nabla_{\Gamma} u}{|\nabla_{\Gamma} u|} - 2\lambda(u - u_0) \right),$$

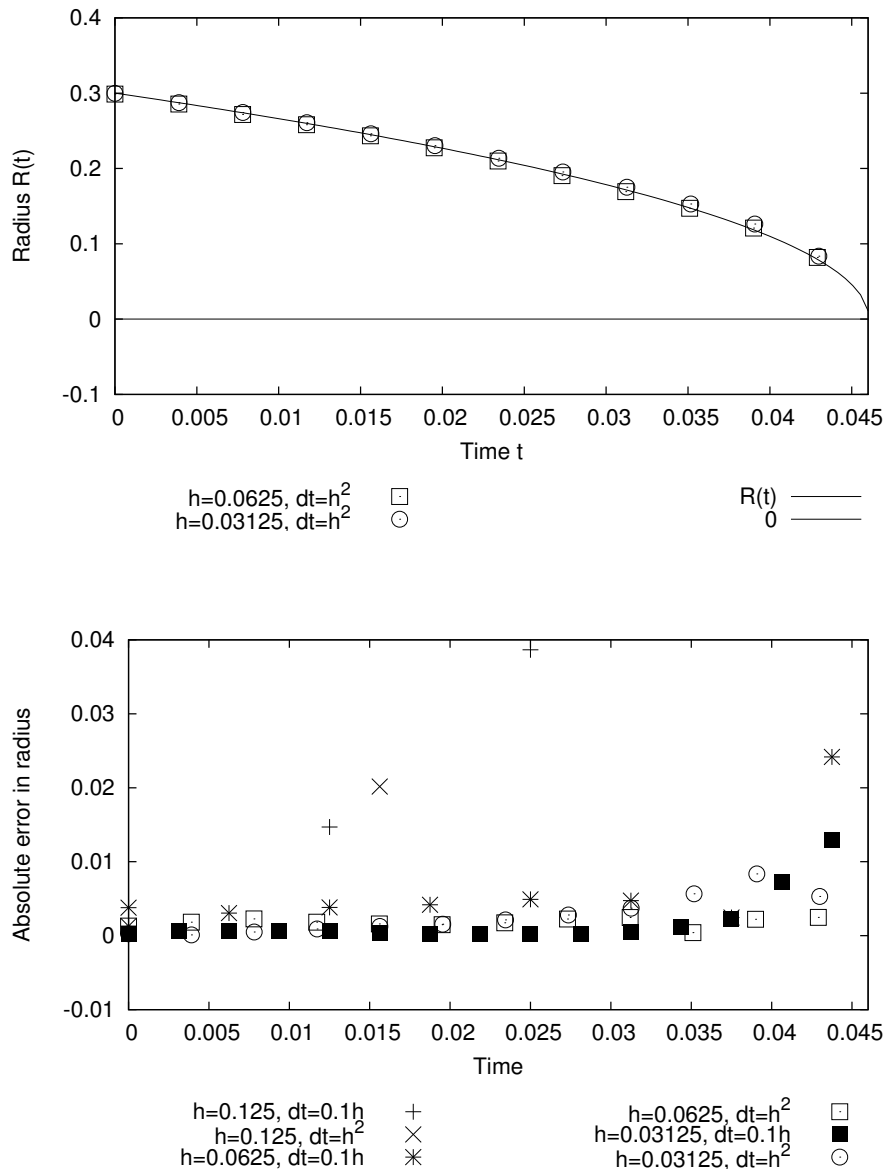


Figure 7.3: Geodesic mean curvature flow with level set representation of the surface: evolution of a circle with initial radius $R_0 = 0.3$ on a sphere with radius $r = 1.0$ with different grid sizes and timesteps, see figure 7.2. Above: comparison of the exact evolution of the circle with computational results with grid sizes $h = 0.0625$ and $h = 0.03125$ and timestep $\Delta t = h^2$. Below: absolute error in the radius with grid sizes $h = 0.125, 0.0625$ and 0.03125 and timesteps $\Delta t = 0.1h$ and h^2 resp.

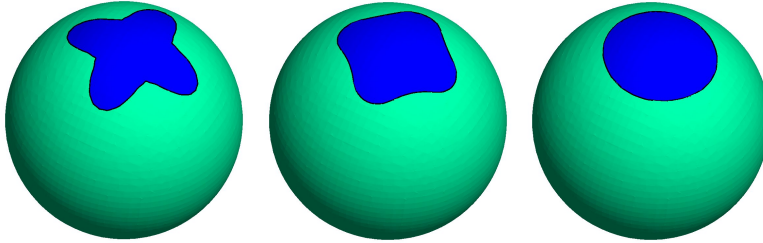


Figure 7.4: Geodesic surface diffusion with level set representation of the surface: evolution of star-shaped closed curve. $[0, 4] \times [0, 4] \times [0, 4]$ grid with 30.000 grid points, grid size $h = 0.0625$ at the surface and timestep $\Delta t = h^4 = 1.5 \times 10^{-5}$. From left to right: $t = 0.0$, $t = 0.0003$, $t = 0.00105$.

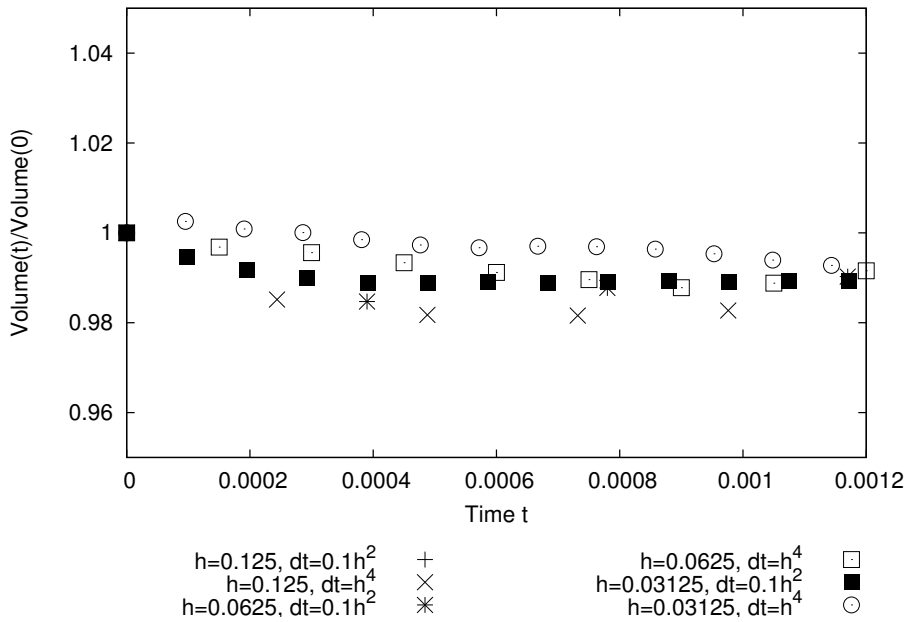


Figure 7.5: Geodesic surface diffusion with level set representation of the surface: volume conservation for the example in figure 7.4 for different grid sizes $h = 0.125, 0.0625$ and 0.03125 and timesteps $\Delta t = 0.1h^2$ and h^4 resp.

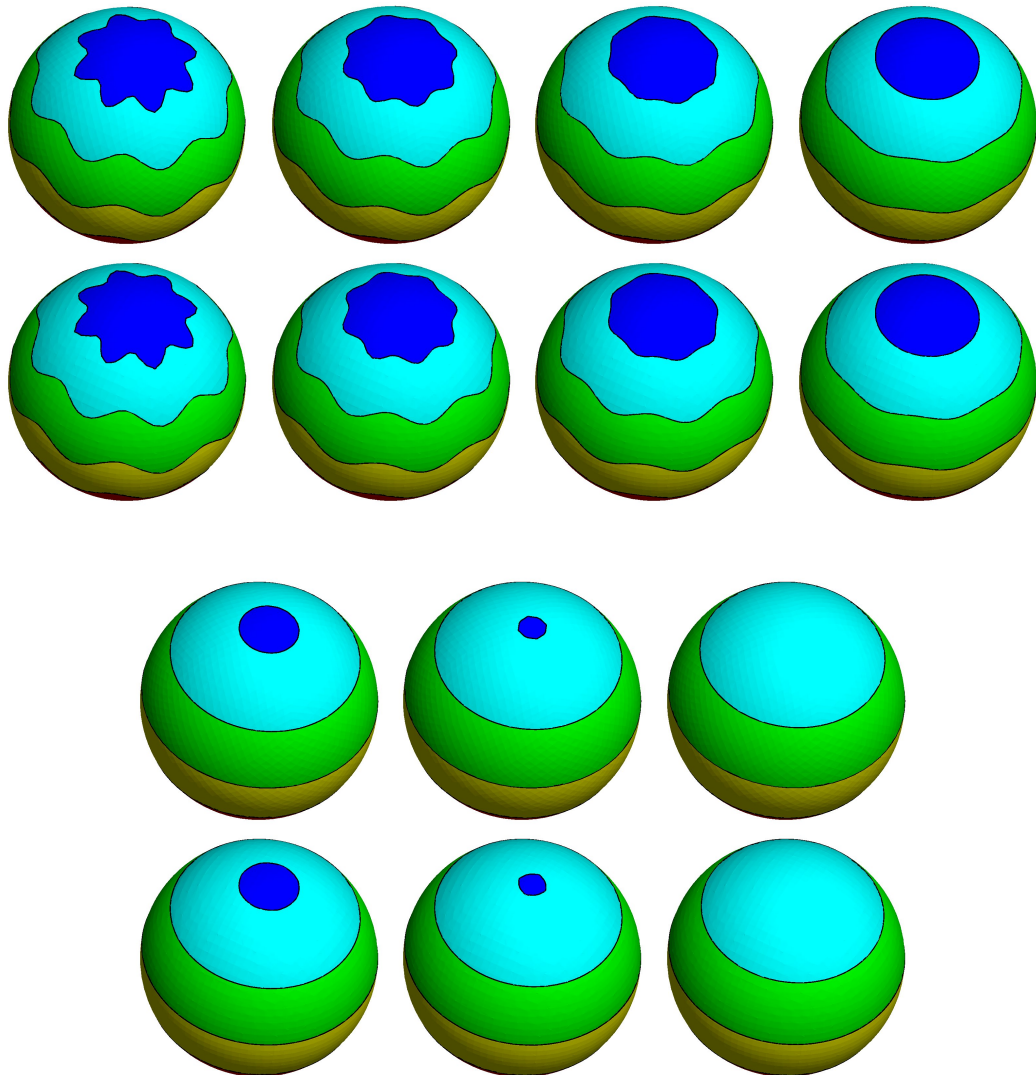


Figure 7.6: Geodesic mean curvature flow with triangulation of the surface (first and third row) and level set representation of the surface (second and fourth row). Parametric approach: 3.000 grid points, grid size $h = 0.064$ and timestep $\Delta t = 0.004$. Level set approach: $[0, 4] \times [0, 4] \times [0, 4]$, grid with 30.000 grid points, grid size $h = 0.0625$ at the surface and timestep $\Delta t = 0.004$. From top left to bottom right: $t = 0.0, 0.004, 0.008, 0.02, 0.096, 0.12, 0.14$.

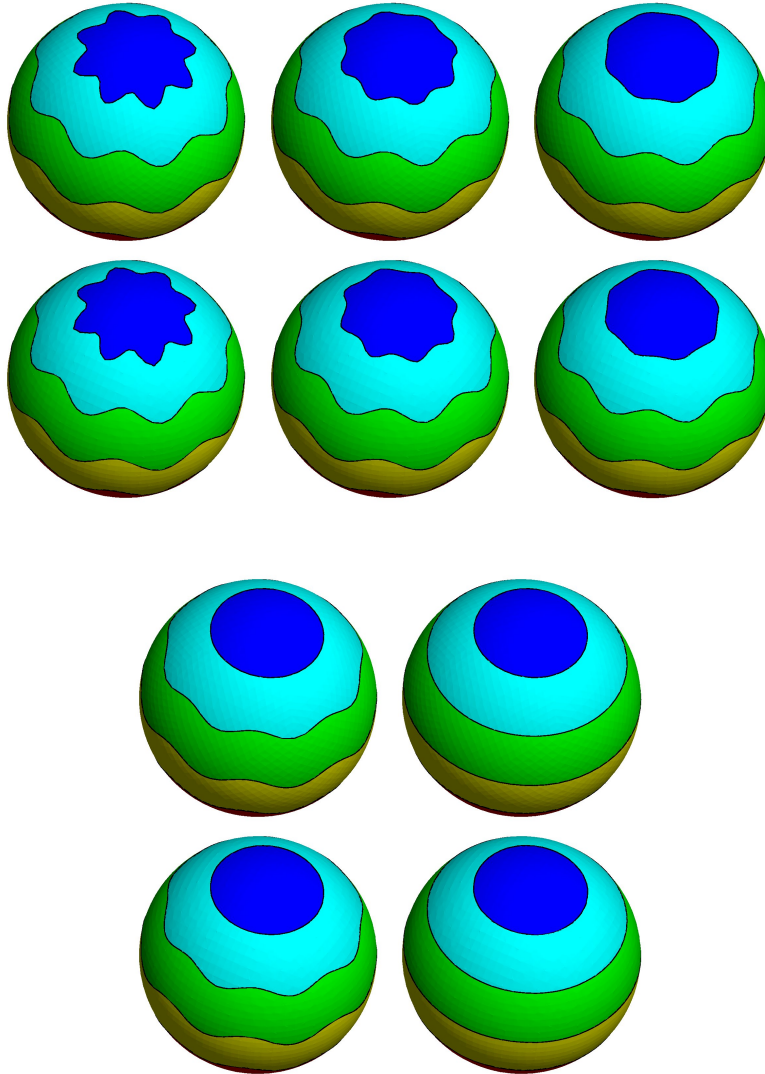


Figure 7.7: Geodesic surface diffusion with triangulation of the surface (first and third row) and level set representation of the surface (second and fourth row). Parametric approach: 3.000 grid points, grid size $h = 0.064$ and timestep $\Delta t = 1.0 \times 10^{-5}$. Level set approach: $[0, 4] \times [0, 4] \times [0, 4]$, grid with 30.000 grid points, grid size $h = 0.0625$ at the surface and timestep $\Delta t = 1.0 \times 10^{-5}$. From top left to bottom right: $t = 0.0, 0.00002, 0.00004, 0.0001, 0.001$.

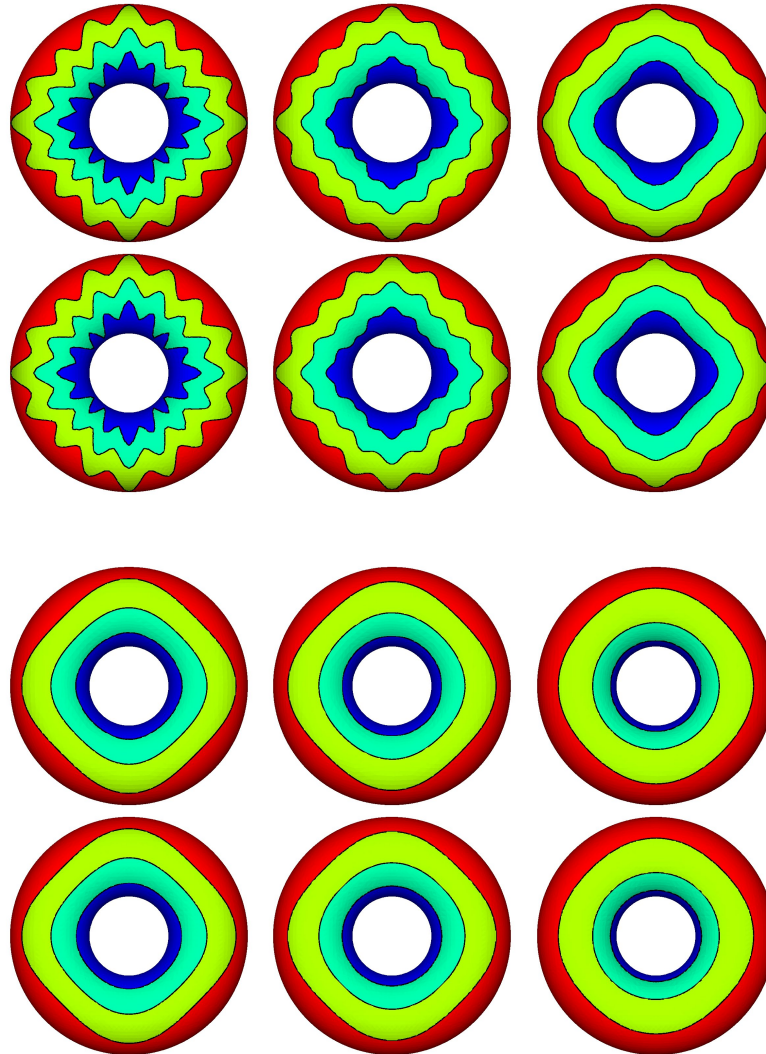


Figure 7.8: Geodesic mean curvature flow with triangulation of the surface (first and third row) and level set representation of the surface (second and fourth row). Parametric approach: 8.200 grid points, grid size $h = 0.048$ and timestep $\Delta t = 0.001$. Level set approach: $[0, 4] \times [0, 4] \times [0, 4]$, grid with 91.000 grid points, grid size $h = 0.005$ at the surface and timestep $\Delta t = 0.001$. From top left to bottom right: $t = 0.0, 0.004, 0.01, 0.06, 0.1, 0.2$.

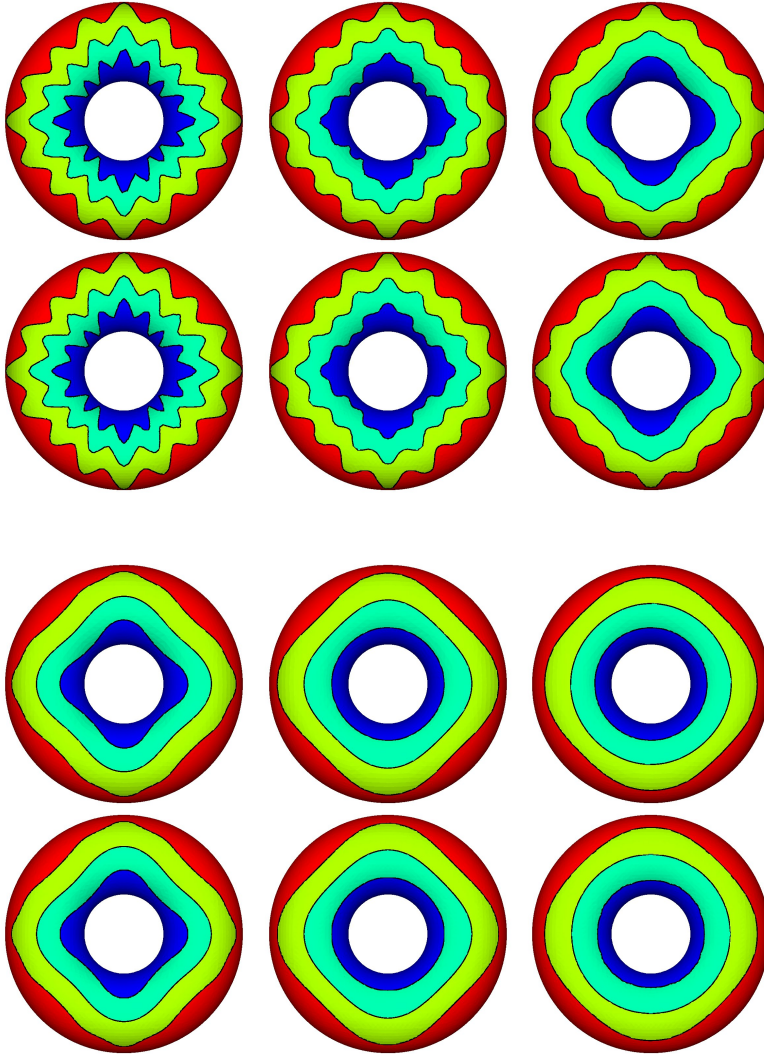


Figure 7.9: Geodesic surface diffusion with triangulation of the surface (first and third row) and level set representation of the surface (second and fourth row). Parametric approach: 8.200 grid points, grid size $h = 0.048$ and timestep $\Delta t = 5.0 \times 10^{-6}$. Level set approach: $[0, 4] \times [0, 4] \times [0, 4]$, grid with 91.000 grid points, grid size $h = 0.005$ at the surface and timestep $\Delta t = 5.0 \times 10^{-6}$. From top left to bottom right: $t = 0.0, 0.00002, 0.00005, 0.0002, 0.003, 0.012$.

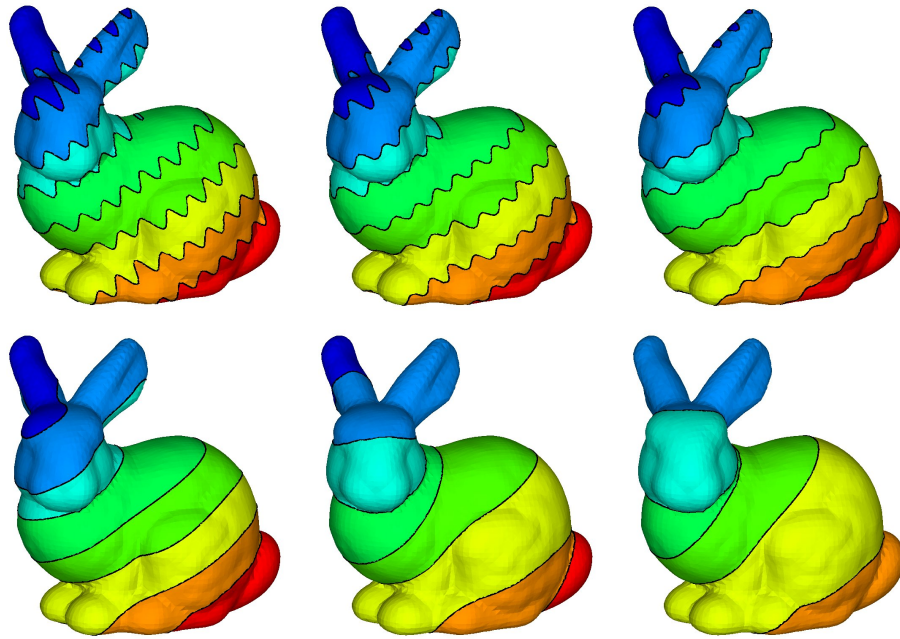


Figure 7.10: Geodesic mean curvature flow with level set representation of the surface: evolution of different level sets. $[0, 4] \times [0, 4] \times [0, 4]$ grid with 192.000 grid points, grid size $h = 0.039$ at the surface and timestep $\Delta t = 0.001$. From top left to bottom right: $t = 0.0$, $t = 0.002$, $t = 0.005$, $t = 0.04$, $t = 1.0$, $t = 1.8$.

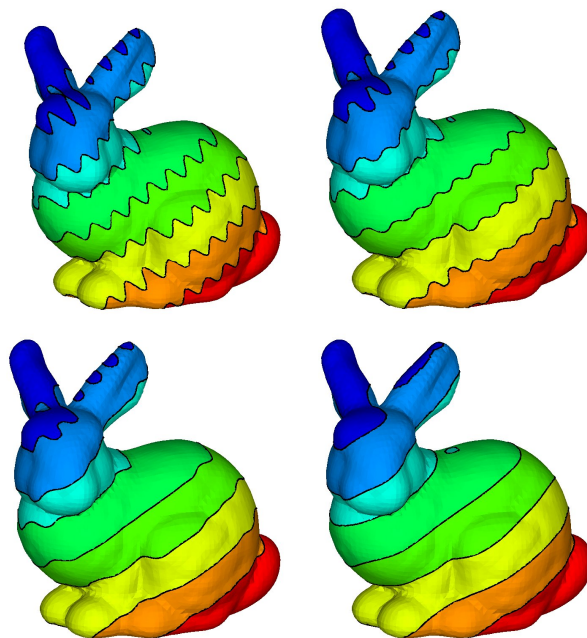


Figure 7.11: Geodesic surface diffusion with level set representation of the surface: evolution of different level sets. $[0, 4] \times [0, 4] \times [0, 4]$ grid with 192.000 grid points, grid size $h = 0.039$ at the surface and timestep $\Delta t = 2.5 \times 10^{-6}$. From top left to bottom right: $t = 0.0$, $t = 0.00002$, $t = 0.00005$, $t = 0.0003$.

and on implicitly defined surfaces, where the equation reads

$$u_t = |(I - \nu \otimes \nu) \nabla u| \left(\frac{1}{|\nabla \phi|} \nabla \cdot \left(|\nabla \phi| \frac{(I - \nu \otimes \nu) \nabla u}{|(I - \nu \otimes \nu) \nabla u|} - 2\lambda(u - u_0) \right) \right). \quad (7.9)$$

The last equation has been solved numerically with finite differences in [7] and [16]. The authors in [7] also extend the calculation of the forcing term coefficient λ from the situation in \mathbb{R}^{d+1} given in [55] to implicitly given surfaces. The idea is as follows: when steady state is reached the term on the left hand side vanishes. Multiplication with $|\nabla \phi|(u - u_0)$ and integration by parts results in

$$\lambda = -\frac{1}{2\sigma^2} \int_{\Omega} |\nabla \phi| \frac{(I - \nu \otimes \nu) \nabla u}{|(I - \nu \otimes \nu) \nabla u|} \cdot \nabla(u - u_0) dx$$

with noise parameter $\sigma^2 = \int_{\Omega} |\nabla \phi|(u - u_0)^2 dx$. We now use this model to demonstrate the possibility to update existing models in image processing to surfaces. For image denoising on implicitly defined surfaces the weak form of (7.9) is given through

$$\begin{aligned} \int_{\Omega} \frac{u_t |\nabla \phi|}{|(I - \nu \otimes \nu) \nabla u|} \eta dx = \\ - \int_{\Omega} |\nabla \phi| \frac{(I - \nu \otimes \nu) \nabla u}{|(I - \nu \otimes \nu) \nabla u|} \cdot \nabla \eta dx - 2\lambda \int_{\Omega} |\nabla \phi| (u - u_0) \eta dx. \end{aligned}$$

The discretization for image denoising reads

$$\begin{aligned} \int_{\Omega} \frac{u^{k+1} |\nabla \phi|_{\delta}}{|(I - \nu \otimes \nu) \nabla u^k|_{\delta}} \eta dx - \int_{\Omega} \frac{u^k |\nabla \phi|_{\delta}}{|(I - \nu \otimes \nu) \nabla u^k|_{\delta}} \eta dx + \\ \tau \int_{\Omega} |\nabla \phi|_{\delta} \frac{(I - \nu \otimes \nu) \nabla u^{k+1}}{|(I - \nu \otimes \nu) \nabla u^k|_{\delta}} \cdot \nabla \eta dx + \\ \tau 2\lambda^k \int_{\Omega} |\nabla \phi|_{\delta} u^{k+1} \eta dx - \tau 2\lambda^k \int_{\Omega} |\nabla \phi|_{\delta} u_0 \eta dx = 0. \end{aligned} \quad (7.10)$$

The forcing term coefficient λ^k depends on the solution u^k of the last timestep and has to be calculated in each timestep in a preprocessing step through

$$\lambda^k = -\frac{1}{2\sigma^2} \int_{\Omega} |\nabla \phi| \frac{(I - \nu \otimes \nu) \nabla u}{|(I - \nu \otimes \nu) \nabla u|} \cdot \nabla(u - u_0) dx.$$

Note that σ^2 is a fixed noise parameter which is an estimation of the amount of noise in the initial image. To complete we present the linear system. With

$$\begin{aligned} M_1 &:= M[|\nabla \phi|_{\delta} |(I - \nu \otimes \nu) \nabla u^k|_{\delta}^{-1}], \\ M_2 &:= M[|\nabla \phi|_{\delta}], \\ L_1 &:= L[|\nabla \phi|_{\delta} (I - \nu \otimes \nu) \nabla u^k|_{\delta}^{-1} (I - \nu \otimes \nu)], \\ R_1 &:= \left(\int_{\Omega} |\nabla \phi|_{\delta} u_0 \varphi_i dx \right)_i \end{aligned}$$

the linear system corresponding to (7.10) is

$$(M_1 + \tau L_1 + \tau 2\lambda^k M_2) \bar{u}^{k+1} = M_1 \bar{u}^k + \tau 2\lambda^k R_1.$$

Again, we solve the linear system with the Krylov subspace method BiCGStab2.



Figure 7.12: Image denoising with level set representation of the surface. From left to right: original image, noisy image, image after 5 timesteps. $[0, 4] \times [0, 4] \times [0, 4]$, grid with 192.000 grid points, grid size $h = 0.039$ at the surface and timestep $\Delta t = 0.001$.

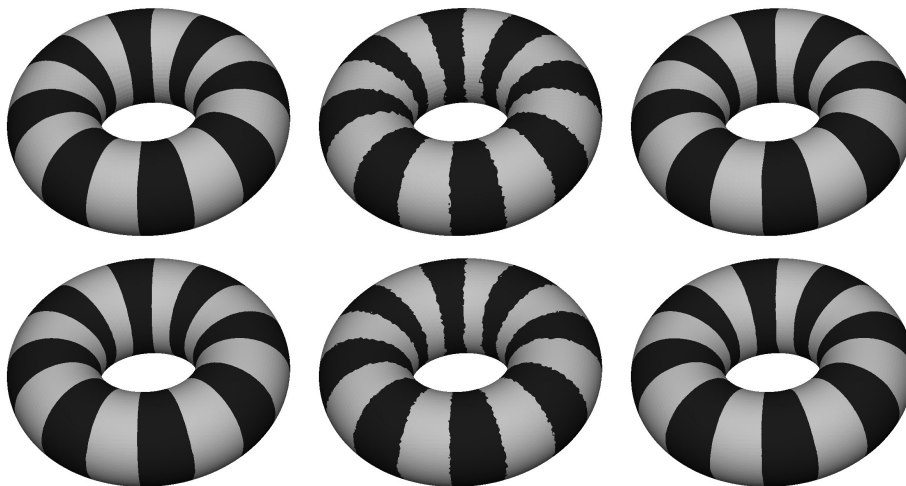


Figure 7.13: Image denoising with triangulation of the surface (top row) and level set representation of the surface (bottom row). From left to right: original image, noisy image, image after 5 timesteps. Parametric approach: 16.500 grid points, grid size $h = 0.034$ and timestep $\Delta t = 0.001$. Level set approach: $[0, 4] \times [0, 4] \times [0, 4]$, grid with 193.000 grid points, grid size $h = 0.03125$ at the surface and timestep $\Delta t = 0.001$.

Figure 7.12 shows results of the approach on the bunny and figure 7.13 shows a comparison between the implicit and the parametric surface representation for image denoising on the torus.

We have presented a framework for the numerical treatment of geometric evolution equations on surfaces with level set methods. Discretizations for triangulated surfaces can be adopted from planar space. For derivations of the discretized equations it makes no difference whether the equations are defined on a planar or a non-planar space. For the computations and numerical stability, however, there may be a difference, as it is more difficult on non-planar surface meshes to guarantee the regularity of mesh elements than in the planar case, especially on complex surfaces. This depends on the mesh generation. In case implicit surfaces are used, the discretization necessitates to express surface gradients in terms of gradients (in space). How this can be done in level set context has been derived and applied to geodesic mean curvature flow in [7]. The application on geodesic surface diffusion has been presented here. Implicit surfaces demand higher computational costs, but have the advantage that standard meshes in Euklidian space can be used and no effort in mesh generation has to be done. If in a next step, PDEs on moving surfaces are considered, the implicit surface approach also offers more flexibility concerning topology changes. PDEs on moving surfaces have been numerically treated in [28] with a triangulation of the surface and in [17, 1, 73] on implicit surfaces.

Chapter 8

Conclusion

A numerical treatment of non-linear higher-order geometric evolution equations with the level set method has been presented. We have considered four different models: the model of mean curvature flow, the model of surface diffusion, a kinetic model, which combined the effects of mean curvature flow and surface diffusion and included a further kinetic component, and an adatom model, which incorporated in addition free adatoms. The dependency on energy functionals has been given and the thermodynamic consistency of the models with respect to these energy functionals has been discussed. In the adatom model the energy did not only depend on the evolving surface, but was also related to the free adatom density. The kinetic and the adatom model were equations modelling surface evolution processes in thin film growth. A brief illustration of the physical background has been given. The models of mean curvature flow, surface diffusion and the kinetic model described the evolution of surfaces, whereas the adatom model was a diffusion equation on a moving surface. The diffusion of adatoms on a surface has been coupled to the geometric evolution of surfaces.

For each model the isotropic, anisotropic and strong anisotropic situation have been treated, where the well-known numerical treatment of the equations of isotropic and anisotropic mean curvature flow and surface diffusion was used as an introduction to and a preparation for the more complicated models. The instabilities in the equations in the strong anisotropic situation have been employed to produce the effect of faceting. A curvature-dependent energy functional has been used to reach the physical phenomenon of corner and edge roundings in the faceted structures. The models delivered geometric evolution equations of up to 6th order and have been split into systems of second order equations.

Numerous numerical examples have been given for each model showing the evolution of curves and surfaces towards the energy minimizing shape (wulffshape). In the kinetic model, the influence of the kinetic term on the dynamics has been analyzed by different parameter choices. It has been observed that choosing the kinetic coefficient in the magnitude of 0.01 or larger leads to a significant slow down in the evolution in comparison to surface diffusion where the kinetic term is neglected. The focus was then on a comparison of the evolution under surface diffusion with kinetics, which is the kinetic model where the mean curvature flow part is neglected, and the evolution under surface diffusion and mean curvature flow. For the employed choice of parameters surface diffusion with kinetics showed the behavior of volume-conserving mean curvature flow, and through that its shape evolution was that of mean curvature flow. The only difference was the difference in the enclosed volume.

In the numerical examples for the adatom model mainly the distribution of the adatoms has been analyzed. The adatom density adopted to the evolution velocity, which is basically determined by the mean curvature. In areas with fast surface changes, high changes in the adatom density have been observed. A comparison with the kinetic model showed that the free adatoms seem to have no influence on the evolving shape. The only difference was the enclosed

volume, which is due to the free adatoms on the surface. The enclosed volume is smaller if the adatom density on the surface is high.

In numerical examples in the strong anisotropic situation, the formation of facets with the correct facet orientations has been shown. Corner and edge roundings occurred on the predicted length scale.

Furthermore, the numerical treatment of geometric evolution equations on curved surfaces has been presented in a level set framework with the examples of mean curvature flow and surface diffusion. Therein, a parametric representation and an implicit level set representation of the curved surfaces have been used. A comparison of numerical results for the two representation methods has been given, and an application to image denoising has been discussed. Numerical results showed the evolution of closed curves on fixed surfaces towards the wulffshape.

The underlying partial differential equations have been numerically solved with standard linear finite elements. Semi-implicit discretization schemes have been employed which resulted in linear systems of equations, which except for the adatom model have been solved with a Schur complement approach. For the adatom model, an operator splitting approach has been applied. The level set treatment, the finite element discretization as well as the resulting linear systems have been described in detail for each equation. To keep computational costs low, the finite element grids were adaptively refined near the moving surface. Redistancing based on a local Hopf-Lax formula has been employed. In particular, an extension of the algorithm to the 3D-setting has been explained in detail.

Acknowledgment

First of all, I would like to thank Prof. Dr. Axel Voigt for getting me in contact with this interesting research field, and for his patience and encouragement throughout the last years, especially in periods when things did not seem to work so well. Furthermore, I would like to thank Prof. Dr. Martin Burger, who advised me in many helpful discussions.

I would like to thank my (former) group at caesar, who supported me in many different ways. Thank you Frank for helping me during the first steps with level sets, for numerous patient explanations and last but not least your encouragement for writing this thesis. Thanks goes also to Andreas for his expertise in variational calculus and differential geometry, to Simon for his kind support in AMDiS and many rapid implementational solutions, to Angel for his advise in error estimators and composite finite elements, and to Rainer for his expertise in gnuplot and frequent technical support in different fields, especially to mention a technical problem in one of the last weeks before finishing this thesis. It was a pleasure to work in this group.

Moreover, I would like to thank Martina Teusner, who supported me in parts of the redistancing algorithm, and Sandra Rasche for her help in the adaption of the redistancing algorithm to extensions in normal direction.

I would like to acknowledge the research center caesar for the financial support during the last years and especially during the last months, which made it possible to finish this thesis here in Bonn.

Bibliography

- [1] D. Adalsteinsson and J. A. Sethian. Transport and diffusion of material quantities on propagating interfaces via level set methods. *J. Comp. Phys.*, 185(1):271–288, 2003.
- [2] www.math.tu-dresden.de/~witkowsk/amdis.
- [3] E. Bänsch, P. Morin, and R. H. Nochetto. Surface diffusion of graphs: variational formulation, error analysis and simulation. *SIAM J. Num. Anal.*, 42(2):773–799, 2004.
- [4] E. Bänsch, P. Morin, and R. H. Nochetto. A finite element method for surface diffusion: the parametric case. *J. Comp. Phys.*, 203:321–343, 2005.
- [5] J. W. Barrett, H. Garcke, and R. Nürnberg. On the parametric finite element approximation of evolving hypersurfaces in \mathbb{R}^3 . *SIAM J. Sci. Comp.*, 29(3):1006–1041, 2007.
- [6] T. J. Barth and J. A. Sethian. Numerical schemes for the hamilton-jacobi and level set equations on triangulated domains. *J. Comp. Phys.*, 145:1–40, 1998.
- [7] M. Bertalmío, L.-T. Cheng, S. Osher, and G. Sapiro. Variational problems and partial differential equations on implicit surfaces. *J. Comp. Phys.*, 174:759–780, 2001.
- [8] F. Bornemann and C. Rasch. Finite-element discretization of static hamilton-jacobi equations based on a local variational principle. *Comp. Vis. Sci.*, 9:57–69, 2006.
- [9] M. Burger. Numerical simulation of anisotropic surface diffusion with curvature-dependent energy. *J. Comp. Phys.*, 203:602–625, 2005.
- [10] M. Burger. Surface diffusion including adatoms. *Comm. Math. Sci.*, 4:1–51, 2006.
- [11] M. Burger. Finite element approximation of elliptic partial differential equations on implicit surfaces. *Comp. Vis. Sci.*, to appear, 2007.
- [12] M. Burger, F. Haußer, C. Stöcker, and A. Voigt. A level set approach to anisotropic flows with curvature regularization. *J. Comp. Phys.*, 225(1):183–205, 2007.
- [13] M. Burger, C. Stöcker, and A. Voigt. Finite element based level set methods for higher order flows. submitted to *J. Sci. Comp.*, March 2007.
- [14] W. K. Burton, N. Cabrera, and F. C. Frank. The growth of crystals and the equilibrium structure of their surfaces. *Phil. Trans. Roy. Soc. London Ser. A*, 243(866):299–358, 1951.
- [15] J. W. Cahn and J. E. Taylor. Overview no 113 - surface motion by surface diffusion. *Acta Metall. Mater.*, 42(4):1045–1063, 1994.
- [16] L.-T. Cheng. *The Level Set Method Applied to Geometrically Based Motion, Materials Science, and Image Processing*. PhD thesis, UCLA, 2000.

- [17] L.-T. Cheng, P. Burchard, B. Merriman, and S. Osher. Motion of curves constrained on surfaces using a level-set approach. *J. Comp. Phys.*, 175:604–644, 2002.
- [18] D. L. Chopp and J. A. Sethian. Flow under curvature: Singularity formation, minimal surfaces, and geodesics. *Exp. Math.*, 2:235–255, 1993.
- [19] D. L. Chopp and J. A. Sethian. Motion by intrinsic laplacian of curvature. *Interfaces Free Bound.*, 1:107–123, 1999.
- [20] U. Clarenz. *Sätze über Extremalen zu parametrischen Funktionalen*. PhD thesis, Universität Bonn, 1999. Bonner Math. Schriften 322.
- [21] U. Clarenz, F. Hauber, M. Rumpf, A. Voigt, and U. Weikard. On level set formulations for anisotropic mean curvature flow and surface diffusion. In *Multiscale modeling in epitaxial growth. International Series of Numerical Mathematics 149*, pages 227–237, Basel, 2005. Birkhäuser.
- [22] K. Deckelnick and G. Dziuk. A fully discrete numerical scheme for weighted mean curvature flow. *Num. Math.*, 91(3):423–452, 2002.
- [23] K. Deckelnick, G. Dziuk, and C. M. Elliott. Computation of geometric partial differential equations and mean curvature flow. *Acta Numerica*, 14:139–232, 2005.
- [24] K. Deckelnick, G. Dziuk, and C. M. Elliott. Fully discrete finite element approximation for anisotropic surface diffusion of graphs. *SIAM J. Num. Anal.*, 43:1112–1138, 2005.
- [25] A. DiCarlo, M. E. Gurtin, and P. Podio-Guidugli. A regularized equation for anisotropic motion-by-curvature. *SIAM J. Appl. Math.*, 52(4):1111–1119, 1992.
- [26] U. Diewald, T. Preusser, and M. Rumpf. Anisotropic diffusion in vector field visualization on euclidean domains and surfaces. *IEEE Trans. Vis. Comp. Graph.*, 6(2):139–149, 2000.
- [27] M. Droske and M. Rumpf. A level set formulation for willmore flow. *Interf. Free Bound.*, 6:361–378, 2004.
- [28] G. Dziuk and C. M. Elliott. Finite elements on evolving surfaces. *IMA J. Num. Anal.*, 27(2):262–292, 2007.
- [29] G. Dziuk and C. M. Elliott. Surface finite elements for parabolic equations. *J. Comp. Math.*, 25(4):385–407, 2007.
- [30] J. J. Eggleston, G. B. McFadden, and P. W. Voorhees. A phase-field model for highly anisotropic interfacial energy. *Physica D*, 150:91–103, 2001.
- [31] P. Thompson F. Memoli, G. Sapiro. Implicit brain imaging. *Neuroimage*, 23:179–188, 2004.
- [32] L.B. Freund and S. Suresh. *Thin Film Materials: Stress, Defect Formation and Surface Evolution*. Cambridge Univ. Press, 2003.
- [33] E. Fried and M. E. Gurtin. A unified treatment of evolving interfaces accounting for small deformations and atomic transport with emphasis on grain-boundaries and epitaxy. *Adv. Appl. Mech.*, 40:1–177, 2004.
- [34] J. B. Greer, A. L. Bertozzi, and G. Sapiro. Fourth order partial differential equations on general geometries. *J. Comp. Phys.*, 216:216–246, 2006.

- [35] M. E. Gurtin and M. E. Jabbour. Interface evolution in three dimensions with curvature-dependent energy and surface diffusion: Interface-controlled evolution, phase transitions, epitaxial growth of elastic films. *Arch. Rat. Mech. Anal.*, 163:171–208, 2002.
- [36] F. Haußer and A. Voigt. A discrete scheme for regularized anisotropic surface diffusion, a sixth order geometric evolution equation. *Interf. Free Bound.*, 7:1–17, 2005.
- [37] F. Haußer and A. Voigt. Facet formation and coarsening modeled by a geometric evolution law for epitaxial growth. *J. Cryst. Growth*, 275:e47–e51, 2005.
- [38] F. Haußer and A. Voigt. A discrete scheme for regularized anisotropic curve shortening flow. *Appl. Math. Lett.*, 19:691–698, 2006.
- [39] C. Herring. Some theorems on the free energies of crystal surfaces. *Phys. Rev.*, 82:87–93, 1951.
- [40] R. Kimmel. Intrinsic scale space for images on surfaces: The geodesic curvature flow. *Graph. Models Image Proc.*, 59:365–372, 1997.
- [41] P.-L. Lions. *Generalized solutions of Hamilton-Jacobi equations*. Research Notes in Mathematics 69, Pitman, Boston, 1982.
- [42] F. Liu and H. Metiu. Dynamics of phase separation of crystal surfaces. *Phys. Rev. B*, 48:5808–5817, 1993.
- [43] T. E. Madey, J. Guan, C.-H. Nien, C.-Z. Dong, H.-S. Tao, and R.A. Campbell. Faceting induced by ultrathin metal films on W(111) and Mo(111): Structure, reactivity, and electronic properties. *Surf. Rev. Lett.*, 3(2):1315, 1996.
- [44] A. Marquina and S. Osher. Explicit algorithms for a new time dependent model based on level set motion for nonlinear deblurring and noise removal. *SIAM J. Sci. Comp.*, 22:387–405, 2000.
- [45] W. W. Mullins. Two-dimensional motion of idealized grain boundaries. *J. Appl. Phys.*, 27:900–904, 1956.
- [46] W. W. Mullins. Theory of thermal grooving. *J. Appl. Phys.*, 28:333–339, 1957.
- [47] T. G. Myers and J. P. F. Charpin. A mathematical model for atmospheric ice accretion and water flow on a cold surface. *Int. J. Heat Mass Transfer*, 47(25):5483–5500, 2004.
- [48] C. H. Nien and T. E. Madey. Atomic structures on faceted W(111) surfaces induced by ultrathin films of Pd. *Surf. Sci.*, 380(2-3):L527–L532, 1997.
- [49] S. Osher and R. Fedkiw. *Level set methods and dynamic implicit surfaces*. Applied Mathematical Sciences. 153, Springer, New York, 2003.
- [50] S. Osher and J. A. Sethian. Fronts propagating with curvature-dependent speed: Algorithms based on hamilton-jacobi formulations. *J. Comp. Phys.*, 79:12–49, 1988.
- [51] D. Peng, S. Osher, B. Merriman, and H.-K. Zhao. The geometry of wulff crystal shapes and its relations with riemann problems. In *Nonlinear Partial Differential Equations*, pages 251–303, Providence, 1999. American Mathematical Society.
- [52] A. Pimpinelli and J. Villain. *Physics of Crystal Growth*. Cambridge Univ. Press, 1998.

- [53] A. Rätz and A. Voigt. Higher order regularization of anisotropic geometric evolution equations in three dimensions. *J. Comp. Theor. Nanosci.*, 3:560–573, 2006.
- [54] A. Rätz and A. Voigt. A diffusive-interface approximation for surface diffusion including adatoms. *Nonlin.*, 20:177–192, 2007.
- [55] L. Rudin, S. Osher, and E. Fatemi. Nonlinear total variation based noise removal algorithms. *Physica D*, 60:259–268, 1992.
- [56] T. V. Savina, A. A. Golovin, S. H. Davis, A. A. Nepomnyashchy, and P. W. Voorhees. Faceting of a growing crystal surface by surface diffusion. *Phys. Rev. E*, 67(2):021606, 2003.
- [57] J. A. Sethian. *Level Set Methods and Fast Marching Methods: Evolving Interfaces in Computational Geometry, Fluid Mechanics, Computer Vision, and Materials Science*. Cambridge Univ. Press, 1999.
- [58] V. A. Shchukin and D. Bimberg. Spontaneous ordering of nanostructures on crystal surfaces. *Rev. Mod. Phys.*, 71(4):1125–1171, 1999.
- [59] P. Smereka. Semi-implicit level set methods for curvature and surface diffusion motion. *J. Sci. Comp.*, 19:439–456, 2003.
- [60] B. J. Spencer. Asymptotic solutions for the equilibrium crystal shape with small corner energy regularization. *Phys. Rev. E*, 69:011603, 2004.
- [61] A. Spira and R. Kimmel. Geometric curve flows on parametric manifolds. *J. Comp. Phys.*, 223:235–249, 2007.
- [62] J. Stewart and N. D. Goldenfeld. Spinodal decomposition of a crystal surface. *Phys. Rev. A*, 46:6505–6512, 1992.
- [63] C. Stöcker, S. Vey, and A. Voigt. AMDiS - adaptive multidimensional simulations: composite finite elements and signed distance functions. *WSEAS Transactions on Circuits and Systems*, 4(3):111–116, 2005.
- [64] C. Stöcker and A. Voigt. The effect of kinetics in the surface evolution of thin crystalline films. *J. Cryst. Growth*, 303(1):90–94, 2007.
- [65] C. Stöcker and A. Voigt. A level set approach to anisotropic surface evolution with free adatoms. *SIAM J. Appl. Math.*, accepted, 2007.
- [66] C. Stöcker and A. Voigt. Geodesic evolution laws - a level set approach. submitted to *SIAM J. Imag. Sci.*, Aug. 2007.
- [67] A. Szczepkowicz and R. Bryl. Observation of vertex-rounding transition for a crystal in equilibrium: Oxygen-covered tungsten. *Phys. Rev. B*, 71:113416, 2005.
- [68] G. Turk. Generating textures on arbitrary surfaces using reaction-diffusion. In *SIGGRAPH '91: Proceedings of the 18th annual conference on Computer graphics and interactive techniques*, pages 289–298, New York, 1991. ACM Press.
- [69] S. Vey and A. Voigt. AMDiS - adaptive multidimensional simulations. *Comp. Vis. Sci.*, 10:57–67, 2007.
- [70] S.J. Watson, F. Haußer, and A. Voigt. A geometric Ginzburg-Landau theory for faceted crystals in 1d: from coarsening to chaos through a driving force. *Phys. Rev. Lett.*, in review.

- [71] T. J. Willmore. *Riemannian Geometry*. Clarendon Press, Oxford, 1993.
- [72] G. Wulff. Zur Frage der Geschwindigkeit des Wachstums und der Auflösung der Kristallflächen. *Zeitschrift für Kristallographie und Mineralogie*, 34:449–530, 1901.
- [73] J.-J. Xu and H.-K. Zhao. An eulerian formulation for solving partial differential equations along a moving interface. *J. Sci. Comp.*, 19:573–594, 2003.
- [74] W. Zhang. Evolution of crystal morphologies to equilibrium by surface diffusion with anisotropic surface free energy in three dimensions. *J. Cryst. Growth*, 297(1):169–179, 2006.
- [75] Y. W. Zhang. Self-organization, shape transition, and stability of epitaxially strained islands. *Phys. Rev. B*, 61(15):10388–10392, 2000.